VNIVERSITAT DE VALÈNCIA

Doctorado en Nanociencia y Nanotecnología

Ph.D. thesis:

Novel architectures and materials for perovskite opto-electronics

Ph.D. candidate:

Benedikt Dänekamp

Supervisors:

Dr. Hendrik Jan Bolink

Dr. Michele Sessolo

Tutor:

Dr. Hendrik Jan Bolink

December 2018

Acknowledgments

First of all, I would like to thank my tutor, Henk for giving me the opportunity to work in this group. You gave me the support that I needed and the freedom and space for the development of my own ideas. I think it is very challenging to find the right balance between these two things and that it requires a very fine sense for people and their way of working. Michele, I appreciated your constant support during my thesis and I would like to thank you for the significant commitment and your exceptional personal involvement. Pablo, I thank you for the scientific inspiration and input, especially during the last period of my Ph.D.

Finally, I would like to thank the entire group for these intensive three years. I have seen and visited a lot of different scientific groups before and during my Ph.D. There are very little groups with this willingness to help. Scientific competition or egoism has never been an issue, something that is exceptional in the scientific world. I would like to thank everyone of you for the time that we spend together, in Valencia having dinner or going out and for the nice trips that we have made together. Lidón, you were probably the person in the group that helped me the most in the lab. Thanks, for being so patient when I ask the same things over and over again. You should be listed as one of my supervisors! Ana, it's a bit weird to be so crazy about cats but I like you very very much! Laura, thanks for being one of the persons that keeps the group together. Dani, I thank you for many creative jokes, even though you write way too many of them in our Whatsapp groups! Jorge, thank you for a very intensive nigh live in Valencia. Kassio, thanks for your hospitality. I like to thank the newcomers, Yous, Paz, and Wiria for enriching this group.

Isidora, for being one of the most positive persons I have met so far. Paco, for the support during my publications. Maria, for solving basically all my problems and for your friendship. Chris, for many inspiring scientific chats and the time we spend together. I'm happy, you joined the group! Finally, I would like to thank my very very close friends Maria Grazia and Azin for so many moments we had and will have together.

Albert, ich danke dir für so vieles! Du bist der beste Freund, den ich in meinem Leben gefunden habe. Ich danke meiner Familie für die Stütze, die ihr mir wart. Wegen euch bin ich der, der ich heute bin. Diese Promotionsarbeit habe ich euch zu verdanken.

Index

Dr. Hendrik Jan Bolink y **Dr. Michele Sessolo**, Investigadores de la Universidad de Valencia en el Instituto de Ciencia Molecular (ICMol), certifican que la memoria presentada por el doctorando Benedikt Dänekamp con el título "**Novel architectures and materials for perovskite opto-electronics**" corresponde a su Tesis Doctoral y ha sido realizada bajo su dirección, autorizando mediante este escrito la presentación de la misma.

En Valencia, a 11 de diciembre de 2018

Dr. Hendrik Jan Bolink Dr. Michele Sessolo

(director y tutor) (director)

1 Introduction

1.1 Hybrid perovskites for third generation solar cells and light-emitting devices

Energy drives modern societies and is the backbone of future generation's development. Energy has become a substantial resource for any human activity, spanning from feeding, health systems, to every part of our economy. As the world's population is constantly growing, energy security and sustainability has become one of our mayor challenges. Up to now, the world's population sill depends strongly on fossil energy sources, which results in greenhouse gas emission contributing to the climate change or other environmental concerns, as well as geopolitical and military conflicts. In the historical unique United Nations Climate Change conference (COP 21) 196 nations agreed to limit the global warming to 2 degrees compared to pre-industrial times, while targeting 1.5. This target requires an ambitious development of renewable energies. There is a multitude of technologies to collect energy from renewable sources such as sunlight wind, rain, tide, waves and geothermal heat. Photovoltaics (PV) is becoming more and more cost competitive, with very little impact on the environment. This is just one of the reasons why the market of solar energy is constantly growing and the 235 GW that were installed worldwide in 2015 are estimated to be doubled by the end of 2018.[1] The PV market is dominated by the established silicon technology, as the first silicon solar cell with power conversion efficiency (PCE) of 6% was already introduced by Bell labs in 1954.[2] Over the last decades the prices of silicon photovoltaic modules dropped significantly and intensive investigation lead to a remarkable improvements in terms of power

conversion efficiency. Howver, while the overall efficiencies have improved over the years, the underlying photophysical principles remained the same and so did the fundamental limitations of this technology. Solar grade silicon is obtained from silicon oxide through a process which requires substantial amount of energy and in particular heat, as the material needs to be melted at over 1400 °C in order to be shaped into high purity single-crystal silicon. The high temperature that is required to process the materials increases the so called energy payback time of a solar cell. The energy payback time is the time an energy sources needs to be running in order to generate the amount of energy that was used for its production. For silicon solar-cells the energy payback time is estimated to be approximately 8 years.[3] The energy-consumption and complexity of the process is not the only drawback. Non–optimal photophysical properties complicate the further expansion of silicon PV technology. Silicon is an indirect bandgap material with a low optical absorption coefficient and a long absorption tail at low photon energy. As a consequence, more material is needed to increase the amount of absorbed photons leading to thick and heavy end products. Heavy silicon solar cells have high transportation and installation costs, contributing to up to 50% of the final costs. The drawbacks of silicon solar cells motivated the development of second generation Photovoltaics. These use of direct bandgap semiconductors that are orders of magnitude more efficient in terms of photon absorption lead to the development of thin film devices. Thin film technologies promised less materials consumption in the production process and easier and inexpensive transportation and installation. The most important technologies are based on cadmium telluride, copper indium gallium selenide (CIGS) and hydrogenated

amorphous silicon (a-Si:H).[4] While these technologies showed to be feasible for commercial application their market share remain below 10%. The third generation of solar cells uses thin film semiconductors that can be processed by simple solution or vacuum methods at mild temperatures and thus promises to overcome the limitations of silicon based solar cells. A promising candidate have been dye-sensitized solar cells (DSSCs) that were originally co-invented in 1988 by Brian O`Regan and Michael Grätzel at UC Berkeley and further developed by Grätzel at École polytechnique fédérale de Lausanne (EPFL), with the first efficient DSSC reported in 1991.[5] DSSCs showed already some of the interesting features of third generation solar cells, such as the processability through simple coating techniques, semi-flexibility and transparency. The latter allows for their integration in glass structures such as windows. Unfortunately it was shown to be unpractical to produce DSSCs without expensive elements such as platinum or ruthenium and avoiding the use of liquid electrolyte. For these reasons, DSSCs are now investigated only for niche applications. A new generation of devices stemming from DSSCs research is the perovskite solar cell, which employs a hybrid organic-inorganic tin or lead-halide film as the light absorber. Using perovskite materials as an active layer promises for simple manufacturing with low overall production cost and a low energy payback time. Perovskite based photovoltaics is nowadays by far the fastest advancing solar technology,[6] with efficiency exceeding 20% and startup companies already promising a quick commercialization.[7] One of the big advantages of perovskites are their versatile and tunable optoelectronic properties which allow application as absorber in a solar cells but also as the active layer in a light emitting diode (LED). Addressing the world energy demand and

reducing the emission of greenhouse gases requires not only the development of renewable energy sources but also a more efficient energy consumption. Worldwide electric lighting consumes 19% of the total global electricity production, which is more than the 36 OECD (Organization for Economic Co-operation and Development) countries consume for all purposes.[8] Further improvement of new lighting technologies such as LEDs would be an indispensable step towards a greener and more sustainable energy policy. In this sense, perovskite have the potential to deliver both a source of renewable energy and of efficient lighting, contributing to decrease the overall energy consumption.

1.2 The structure property relationship of thin film perovskite devices

Three dimensional perovskites are defined by a general ABX_3 structure with X as an anion and A and B being cations of different size and charge. The crystallographic stability of a perovskite structure can be estimated from the tolerance factor (t) and the octahedral factor (μ) [9] where t is defined as the ratio between the distances A-X to the distance B-X which themselves depend on the ionic radii. Assuming a perfect solid-sphere model t and μ are defined as:

$$t = \frac{r_{A+}r_X}{\sqrt{2(r_{B+}r_X)}}$$

$$\mu = \frac{R_B}{R_X}$$

R_A, R_B and R_X are the ionic radii of the cations and anions. For a halide perovskite with X = F, Cl, Br, I a stable structures results when $0.81 < t > 1.11$ and $0.44 < \mu > 0.90$. For the most frequently used organic-inorganic perovskite, the organic cation A is large with methylammonium ($CH_3NH_3^+$) having an ionic radius of R_A = 0.18 nm[10] and ethylammonium ($CH_3CH_2NH_3^+$), formamidinium ($NH_2CH{=}NH_2^+$) having ionic radii of R_A=0.23 nm[11], R_A=0.19-0.22 nm.[12–14]

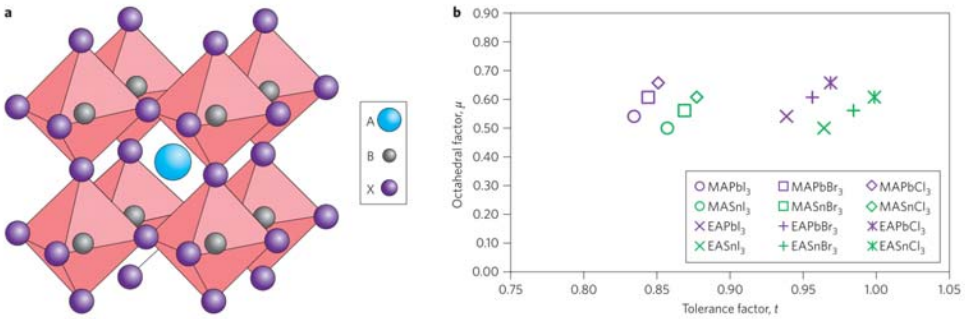

Figure 1. a) Crystal structure of a cubic perovskite. B) Calculated tolerance factor (t) and octahedral factor (μ) for commonly used halide perovskite structures, adapted from reference[15].

I, Br and Cl are most commonly used as the anion X and have ionic radii of 0.220 nm, 0.196 nm, and 0.181 nm, respectively.[15] The cation B is usually a divalent metal such as Pb^{2+} or Sn^{2+}. If *t* lies in an even narrower range of 0.89 - 1.0, a cubic structure is expected (Figure 1), while less symmetric tetragonal and orthorhombic structures are predicted for lower *t* values. Nevertheless, the structure of a perovskite does not solely depend on the size of its ions but also on the temperature. The methylammonium lead iodide perovskite (MAPI) for instance undergoes a phase transition from tetragonal (β) to cubic (α) phase at 56 °C[16], while an orthorhombic (γ) phase is stabilized at low temperatures, around 160 K. The temperatures of the phase transitions has important implications for the thermal stability of the perovskite structure. The higher temperature for the tetragonal to cubic phase transition of Formamidinium lead iodide ($FAPbI_3$) together with the higher evaporation temperature of the material itself can partially explain its higher thermal stability.[14]

Hybrid lead halide perovskites show interesting features for applications in thin film light-emitting diodes and solar cells. LEDs based on perovskite emitting layers exhibit a narrow emission bandwidth which is tunable over the entire visible spectrum, leading to high color purity. The bandgap can be tuned by exchanging the halides and the $MAPbX_3$ perovskites with $X = Cl^-$, $X = Br^-$, or $X = I^-$ have bandgaps of approximately 3.1 eV, 2.3 eV and 1.6 eV, respectively.[17] A further fine-tuning of the bandgap is obtained mixing the halides in different ratios[18] (see Figure 2a). The wide bandgap perovskites containing Br- and Cl- have been predominantly used for LEDs as they emit in the visible range and show higher exciton binding energies compared to perovskites containing other halides.[19] In contrast, the iodine containing MAPI has excellent properties for PV applications.

The absorption coefficient $\alpha > 10^5$ cm^{-1} (Figure 2a) is extremely high allowing for high photocurrent output using submicron thick films. One of the reasons for the high absorption coefficient is the direct bandgap nature of the material. Upon absorption of a photon, an electron hole pair is generated. The attraction between the electron and the hole needs to be overcome in order to generate free carriers. For the MAPI perovskite the exciton binding energy was estimated to be <5 meV at room temperature, which is lower than the thermal energy (26 meV) thus allowing for the direct generation of free carriers.[20,21] Balanced electron/hole mobility and long diffusion length have been proven to be another advantage of MAPI, facilitating the extraction of carriers. The charge carrier transport is directly related to the band structure of the semiconductor via the carrier effective mass. The electron and hole effective masses ($m^*_{e,h}$) depend directly on the curvature of the conduction and valence bands. Low values for MAPI with $m^*_{e,h}$ (0.1-

0.15) m_0, m_0 being the free electron mass, have been reporter.[20,22] The low carrier effective masses are a result of high spin-orbit coupling due to the heavy Pb atom.[23]

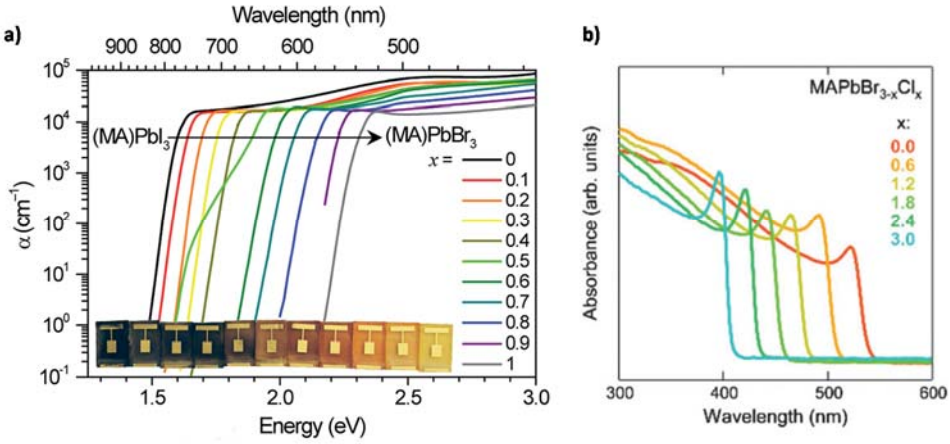

Figure 2. a)Absorption of $(MA)PbI_3$ with increasing Br content, adapted from reference.[24] b) absorption coefficient of $MAPBBr_{3-xClx}$ thin films with increasing Cl content, adapted from reference.[18]

The aforementioned photo physical properties make perovskite good candidates for optoelectronic devices. Nevertheless, not all of the perovskite properties are necessarily beneficial. Already decades ago scientist found that electronic charge carriers are not the only mobile species in perovskites.[25] It was suggested that iodide vacancies and interstitials are mobile as well which leads to a mismatch of JV curves that were taken with different voltage speeds or different scanning directions (forward or reverse bias), a phenomena called Hysteresis.[26] But Hysteresis is not the only phenomena that complicates data interpretation. The structure and morphology of perovskite thin films have an enormous effect on the overall device performance. The very same perovskite compound can have different

properties depending on the deposition techniques and conditions. In particular, the perovskite deposition is a very delicate process influencing the crystallinity, grain size, and grain boundaries (GB) of the material. The importance of grain boundaries can be understood by photoluminescence microscopy, where the grain itself appears bright and the grain boundaries appear dark.[27] The dark areas indicate an increased trapping, thus it is not surprising that perovskites with large grains show generally improved devices efficiencies. Nevertheless, co-evaporated perovskite films seem to be an exception as, besides being composed by small grains, high device efficiencies have been reported.[28]

1.3 Device architecture

Perovskite solar cells can be divided in two mayor groups, mesoporous (Figure 3a) and planar structures (Figure 3b, c). The first perovskite solar cell ever reporter was a modification of a dye sensitized cell with the dye being replaced by perovskite as the absorber material.[29] The mesoporous material is usually metal-oxide with TiO_2 or Al_2O_3. In DSSC the mesoporous structure has an important function, namely the infiltration of the dye and electronically the dissociation of excitons in free carriers but it was later proven that perovskite can also work in a planar configurations where the active layer is sandwiched between two selective transport layers that allow either the transport of electrons (hole blocking) or holes (electron blocking). Depending on the side through which the light enters, the devices are either denoted as n-i-p or p-i-n. In an n-i-p configuration the light enters through the electron transport layer, whereas in a p-i-n configurations it enters through the hole transporter. It is worth nothing that the terms solely refers to the order of layers at which the light passes and not to the potential profile across the devices. It is still under debate if the electric potential in perovskite devices follow a p-n junction or a p-i-n characteristics and both have been reported.[30,31]

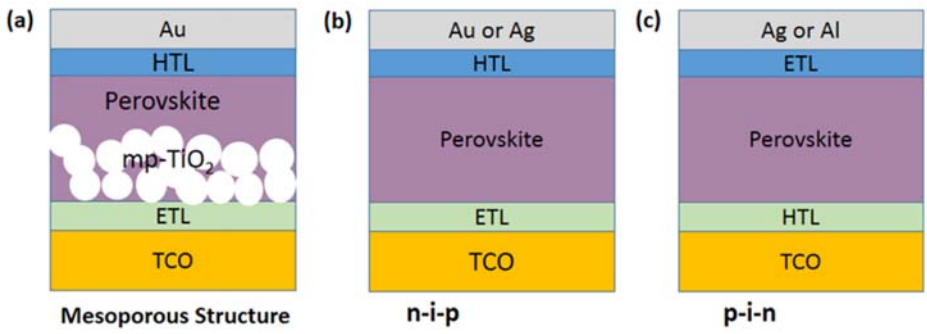

Figure 3. Device architectures of perovskite solar cells. a) mesoporous n-i-p structure , b) planar n-i-p structure, c) planar p-i-n structure. Adapted from reference.[32]

In this thesis, both p-i-n and n-i-p configurations are used. In most of the cases the perovskite active layer was sandwiched between two thin transporting layers, namely C_{60} as electron transport materials and a derivative of arylamine N4,N4,N4”,N4”- tetra([1,1´-biphenyl]-4-yl)-[1,1´:4´,1”-terphenyl]-4,4”-diamine (TaTm) as hole transport material. The thin layers are followed by a thicker layer of the same material but doped in order to enhance the conductivity and hence the carrier extraction. The entire stacks were always fully evaporated on pre-patterned ITO and capped with thin metal layers as top reflective contacts.

1.4 Basic processes of operating perovskite solar cells and light emitting devices

When the perovskite layer absorbs a photon, free carriers are generated even at room temperature. The photogenerated carriers need to reach the selective contacts and extracted before they recombine. To which extend carrier can be extracted depends on the carrier mobility. The carrier mobility can be expressed as:

$$\mu_{n,p} = \frac{e\tau_{n,p}}{m^*_{n,p}}$$

With *e* being the electron charge, $m^*_{n,p}$ the carrier effective mass and $\tau_{n,p}$ the carrier lifetime. Perovskite show very low carrier effective masses and carrier lifetimes of several hundred ns have been reported.[33] Nevertheless, the actual carrier mobility is lower what would be expected from the low recombination and low trapping probabilities.[34,35] The reasons for the moderate carrier motilities are still under debate but scattering phenomena due to lattice vibrations or defects have been suggested as limiting factors.[36]

Another limiting process is the non radiative charge recombination as it competes with charge extraction. There are three different types of recombination in perovskite devices (Figure 4) and carriers can either recombine radiatively or non-radiatively. A direct radiative recombination is the recombination of an electron from the conduction band with a hole in the valence band, releasing a photon with the energy of the bandgap. This bimolecular recombination rate is given by:

$$R_B = \gamma(np - n_i^2)$$

With n and p being the electron and hole densities, n_i being the intrinsic carrier concentration and γ being the bimolecular recombination rate. Bimolecular recombination is low under normal solar cell operation.[37] Nevertheless, non-radiative trap assisted recombination can have a significant impact on the device performance even at 1 sun illumination. Defect assisted recombination occurs at defects in the lattice structure such as grain boundaries and can be expressed by Shockley-Read-Hall (SRH) statistics:

$$R_{RSH} = \frac{C_n C_p \Sigma_T}{C_n(n + n_1) + C_p(p + p_1)}(np - n_i^2)$$

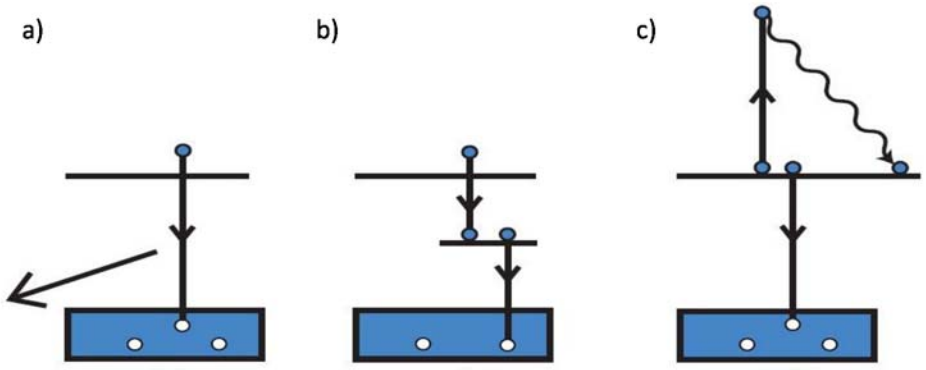

Figure 4. Different types of recombination in perovskite solar cells. a) radiative biomolecular recombination, b) non-radiative trap assisted recombination, c) non-radiative auger recombination. Adapted from reference.[38]

Where Σ_T is the trap density and n_1 and n_2 being constant that depend on the energy levels of the traps. C_n and C_p are the capture coefficients for electrons and holes and reflect the probability per unit time that an electron will be captured from the CB when the trap is filled with a hole (C_n) or the

probability that a hole is captured from the VB if the trap is filled with an electron (C_p). Surface recombination is a special case of defect assisted recombination and is thus often referred to as interfacial SRH recombination. At the perovskite surface the lattice structure is disrupted leading to a high defect densities.[39] The particularly high recombination in this area leads to depletion of the minority carriers. Minority carriers need to diffuse to the surface area and therefore the surface recombination is limited by the rate at which minority carrier move towards the surface, the so called surface recombination velocity.

The third type of recombination is Auger- or phonon assisted recombination. An electron and a hole recombine and transfer their energy and momentum to another electron. As this type of recombination only occurs well above the intensity of 1 sun in the perovskite it will not be further discussed.

The performance of a solar cell is analyzed by means of current density vs. voltage (JV) characteristics. In a calibrated solar simulator a solar cell is illuminated and the current is measured as a function of an applied voltage. The current of a solar cells is described by the classic Shockley diode equation:

$$J = J_{ph} - J_0 \left\{ e^{\frac{qV}{mKT}} - 1 \right\}$$

Where J_{ph} is the photocurrent, V is the applied voltage, J_0 is the reverse saturation current density, q is the elementary charge and n_{ID} is the ideal factor, K the Boltzmann constant and T the absolute temperature. From the JV characteristics several parameters can be extracted.

- Short circuit current density (J_{SC}, mA cm^{-2})

The short circuit is the current that is measured when no voltage is applied and can be described by the following equation:

$$J_{SC} = q \int_0^{\infty} EQE_{PV}(E) \emptyset_{AM1.5}(E) dE$$

EQE_{PV} is the external quantum efficiency which is the number of extracted charges divided by the number of photons received by the surface of the cell. $\phi_{AM1.5}$ is the solar photon flux.

- Open-circuit voltage (V_{oc},V)

  The V_{oc} is the difference in electrical potential at open circuit, and is the maximum achievable voltage of a solar cell. The V_{oc} can be expressed as presented below:

$$V_{oc} = \frac{KT}{q} \ln\left(\frac{J_{SC}}{J_0}\right)$$

  Low non-radiative recombination rates as well as higher photon fluxes (which increase the photocurrent) lead to higher V_{oc} . The ideality factor of a diode can be calculated measuring the V_{oc} as a function of photon flux. The ideality factor reflects the dominating type of recombination. A more comprehensive discussion on ideality factors can be found in the chapter “Influence of hole transport material ionization energy on performance of perovskite solar cells”.

- Maximum power point (MPP)

  The point in a JV-curve corresponding to the maximum power output.

- Fill factor (*FF,* %)

  The FF is the ratio between the theoretical maximum power point of a solar cell and the measured maximum power point:

$$\mathrm{FF} = \frac{\mathrm{V_{mp}} * \mathrm{J_{mp}}}{\mathrm{V_{OC}} * \mathrm{J_{SC}}}$$

  As depicted in Figure 5, the FF is a measure of the "squareness" of the JV-curve. The FF is predominantly influenced by the series and shunt resistances of a solar cell. A high series resistance and low shunt resistance lower the FF. Thus the FF does not only depend on the active absorbing layer but on the entire device architecture.

- Power conversion efficiency (PCE, %)

  The overall performance of a solar cell is indicated by the power conversion efficiency and depends on the fraction of incident power (P_{in}) that is converted into a current:

$$PCE = \frac{FF * V_{OC} * J_{SC}}{P_{in}} 100$$

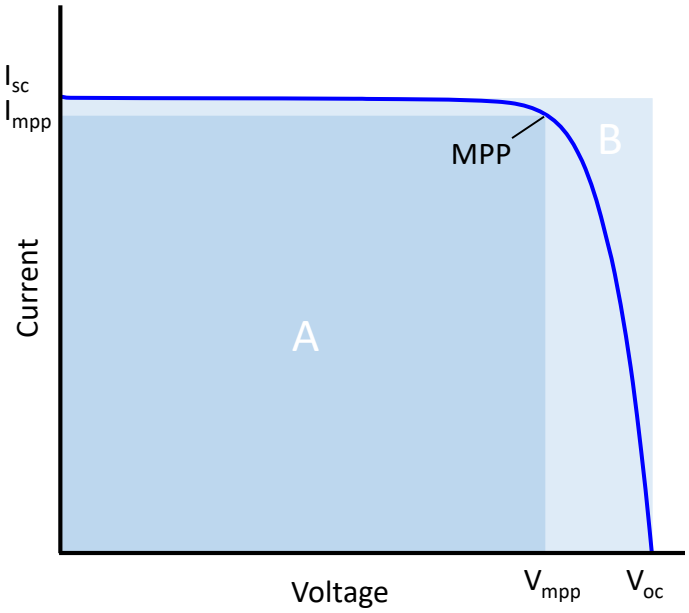

Figure 5. JV-Curve of a perovskite solar cell. The Fill Factor is defined as $FF = \frac{V_{mp} * J_{mp}}{V_{OC} * J_{SC}} = \frac{Area\ A}{Area\ B}$.

A further and deeper analysis of a diode can be achieved measuring the JV-curve in the dark. Dark JV-curves are usually plotted in a logarithmic scale in order to be able to identify the different regimes of the curve. As shown in Figure 6, there are three different regimes in a perovskite diode dark JV-curve. At low voltage, the resulting current is dominated by the shunt resistance (A). At voltages higher than the built in voltage carriers start to get injected and the resulting current is controlled by diffusion (B). The current

at section C is caused by the drift of carriers and relates with the series resistance.

Light emitting devices work very similar to solar cells. In fact, when a voltage is applied to a solar cells, some of the injected carriers recombine and emit a photon. Thus every solar cell could be used as an LED. Nevertheless, active layers in solar cells differ from those that are used in LEDs. The bandgap of the active emitting material is tuned to get a narrow emission bandwidth within the visible spectrum, with the aim to reach high color purity and the structure of the light emitting layer is adapted to increase the exciton binding energy.

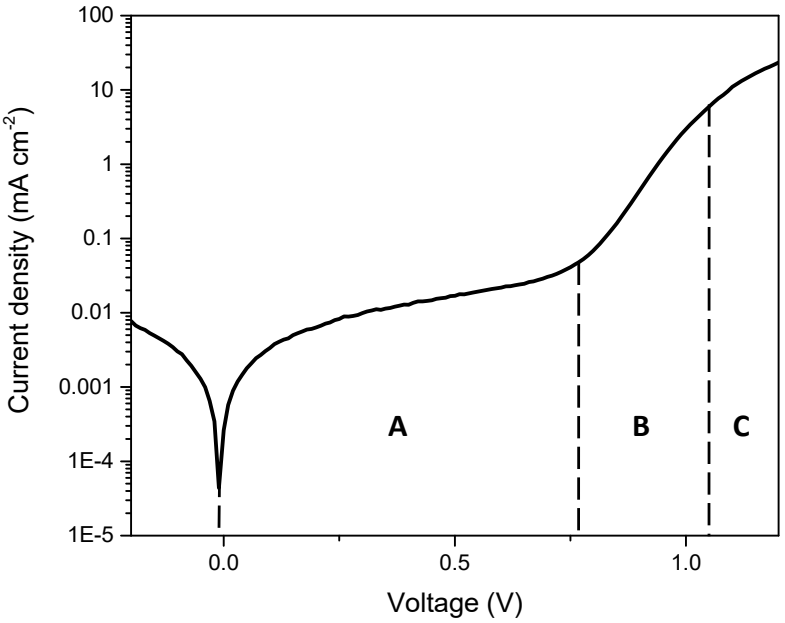

Figure 6. Representative JV-curve of perovskite solar cells under darkness. The different regions A, B, C are dominated by shunt current (A), diffusion current (B), drift current that is limited by the series resistance (C).

The most common parameters to analyze LEDs are:

- Luminance (cd/m^2)

  Luminance is measured in the SI unit candela per square meter (cd/m^2) and is a photometric measure of the luminous intensity. It describes the amount of light being emitted or reflected from a known area. Luminance is corrected for the sensitivity of the human eye and will thus indicate how bright a surface will appear.

- Current density (A/m^2)

  Current density responds to a current that is passing through a unit of area in a device

- Current efficiency (cd/A)

  The current efficiency gives the ratios between the luminance per current density. It is thus a measure of the efficiency of a LED.

- Power efficiency (lm/W)

The power efficiency or luminous efficacy is the ratio of luminous flux to power and a measure of the efficiency of a light source to produce visible light. It takes not only the current density into account but also the applied voltage.

- External quantum efficiency (EQE_{EL}, %)

The external quantum efficiency gives the ratio between the injected electrons over the photons emitted from the device surface

1.5 State-of-the-art

It is only a few years ago that perovskite solar cells were introduced, yet they are competing with photovoltaic technologies that were developed for decades. Nowadays crystalline silicon solar cells is still the most mature photovoltaic technology with efficiencies reaching 26%[40], however the highest reported efficiency for perovskite solar cells has already exceeded 23%.[41] It is noteworthy that this record was fabricated with an area as small as 0.09 cm^2, while larger devices reach efficiencies of 19.7%[42] on a 1 cm^2 cell and 12.1%[43] on a 36.1 cm^2. One of the big advantages of perovskites over crystalline silicon is the compatibility with several substrates, even flexible, with reported efficiencies exceeding 18% for an area of 0.1 cm^2.[44] However while the development of perovskite solar cells seems promising, they are still far away from a considerable market share. The replacement of lead with non-toxic materials remains challenging and a long term-stable perovskite solar cell produced on a large area with reasonable efficiency needs still to be demonstrated.

The toxicity and pure stability, together with low efficiencies are also the main reasons why perovskite based LEDs are still not applied in consumer electronics such as flat-panel displays. After decades of research the modern consumer market for displays could be soon dominated by organic light emitting diodes (OLEDs) and semiconductor quantum dots. EQEs of more than 20% without enhanced optical out coupling are frequently reported for OLEDs. [45–47] Nevertheless it took only 4 years to increase the EQE of perovskite LEDs from 1% [48] in 2014 to around 14% [49] in 2018. With quasi-two-dimensional structures the efficiency of perovskites based LEDs can be

further enhanced and an efficiency of more than 20% at current density between 0.1-1 mA cm^{-2} has been reported recently when a quasi-two dimensional perovskite structure was used in a polymer bulk heterojunction.[49,50]

2 Aim of the thesis

Photovoltaic and light emitting devices based on perovskites have shown an impressive development in the last years. Despite the fast progress, many studies relied still on a trial and error approach in order to further boost device efficiencies. The aim of the thesis is therefore to get further inside into phenomena related to the fundamental photophysics on both perovskite solar cells and LEDs. The work has been structured in three parts:

- Perovskite-Perovskite Homojunctions via Compositional Doping
  One of the most important properties of semiconductors is the possibility to control their electronic properties via intentional doping. Nevertheless doping in perovskite remains nearly unexplored and perovskite pn-junctions have never been reporter. In this work we aim to intentionally dope the material to build a perovskite homojunction.

- Efficient photo- and electroluminescence by trap states passivation in vacuum-deposited hybrid perovskite thin films
  Trap states account for most of the efficiency losses in perovskite LEDs. The goal is therefore to passivate Trap states in MAPI perovskite LEDs using high excess of MAI. The so produced films should increase the overall efficiency.

- Influence of hole transport material ionization energy on performance of perovskite solar cells

The V_{oc} is among the most important parameters controlling the power conversion efficiencies in solar cells. We thus investigate if the V_{oc} is either influenced solely by the nature of recombination or additionally by the ionization potential of the organic transport materials.

Each chapter will consist of an introduction and a detailed description of the methodology and experimental setups and completed with a discussion of the experimental data.

3 Experimental methods

3.1 Vacuum deposition of optoelectronic devices

There are a multitude of technologies to deposit the different layers in perovskite solar cells and light emitting diodes, ranging from solution based techniques such as spin coating and doctor blading to vacuum based techniques. The choice of the deposition technique is important as it strongly influences the morphology of the perovskite film and thus their optoelectronic properties. The challenge is to produce highly uniform films with high crystallinity that are pinhole-free, to guarantee efficient charge transport. A precise control over the layer thickness is another parameter that needs to be considered before a deposition technique is chosen. Devices in this thesis were exclusively produced by vacuum deposition as this deposition method comes with a variety of advantages in comparison to solution based technics.

- Substrates independent processability

  The formation of a film in solution processed techniques depends highly on the substrate the film is spun on. The morphology and roughness of the underlying layer will highly effect the following layer. The vacuum deposition of perovskite thin films is virtually independent of the substrates and can be carried out at room temperature. This allows for deposition on substrates such as plastics, textiles or even on structured silicon for a tandem applications.
- Possibility of upscaling

Vacuum deposition techniques are widely used in semiconductor industry which facilitates to transfer the knowledge from academia to an industrial environment.

- High purity of precursors

  The fine temperature control of the precursors during the evaporation process allows to eliminate the impurities with different sublimation temperatures.

- Fine control of layer thickness

  The layer thickness is usually monitored during the evaporation process using sensitive quartz crystal microbalances (QCMs), which function by means of variation of their acoustic impedance. In a well calibrated system, sub-nanometer precision can be reached which allows for production of devices where the exact thickness is crucial such as optical cavities.

- Intrinsically additive

  The drawback of solution processed methods is that the solvent of each layer can possibly dissolve the underlying layer. Hence, materials and solvents must be chosen accordingly. As evaporated layers don't require any solvents, they are intrinsically additive.

For the aforementioned reasons, dual-source vapor deposition is the method that was used for this thesis. In a dual source evaporation process, the two perovskite precursors PbI_2 and MAI are heated simultaneously in a high vacuum chamber (*Figure 7*). A rotating sample holder is mounted above the source allowing the precursors to deposit on the substrate and react directly to form the perovskite, without any additional annealing steps. The

stoichiometry of the perovskite can be tuned changing the relative deposition rates, which are controlled in real time using QCMs. The first perovskite dual source evaporation was used to produce PbI-based layered Perovskite Quantum Wells.[51] This method was later adapted by our group to produce different and more efficient perovskite solar cells.[52,53]

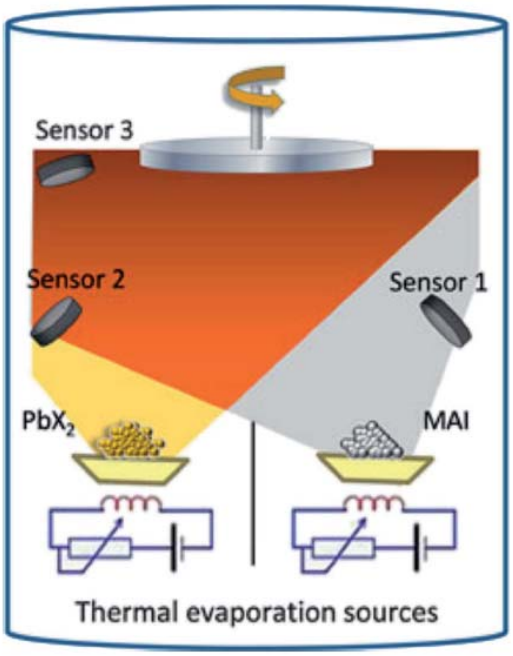

Figure 7. Illustration of a perovskite co-evaporation process. The precursors PbI_2 and MAI are thermally evaporated in a vacuum chamber. Their rate is monitored using quartz microbalances.

3.2 Characterization technics

A multitude of characterization techniques was used in this thesis. Common analytic techniques such as JV-measurements, UV-VIS spectrometry, photoluminescence (PL) measurements, scanning electron microscopy (SEM), and X-ray scattering techniques will not to be discussed. This chapter will focus on characterization techniques that are less frequently used in device production such as Scanning Kelvin probe microscopy, Photoemission spectroscopy and photoluminescence decay dynamics.

Scanning Kelvin Probe Microscopy (KPFM)

A Scanning Kelvin Probe Microscopy setup is an extension of an Atomic force microscope (AFM) with a Kelvin probe tip (Figure 8). The mechanics of the AFM is used to scan a surface with a certain depth profile in the nanometer range. The AFM tip is modified in a way that the cantilever serves as reference electrode and thus forms a capacitor with the sample surface which causes a long-range electrostatic force between the tip and the surface. The electrostatic force is determined by the contact potential difference (CPD) and leads to an additional vibration of the cantilever. A dc voltage is applied to the tip in order to compensate the electrostatic force. The applied dc voltage is thus equal to the CPD. The measure of the CPD allows one to deduce the energetics in conductors or semiconductors such as the Fermi-level which was used in this thesis to identify the type of doping (n- or p-type) in perovskite structures.

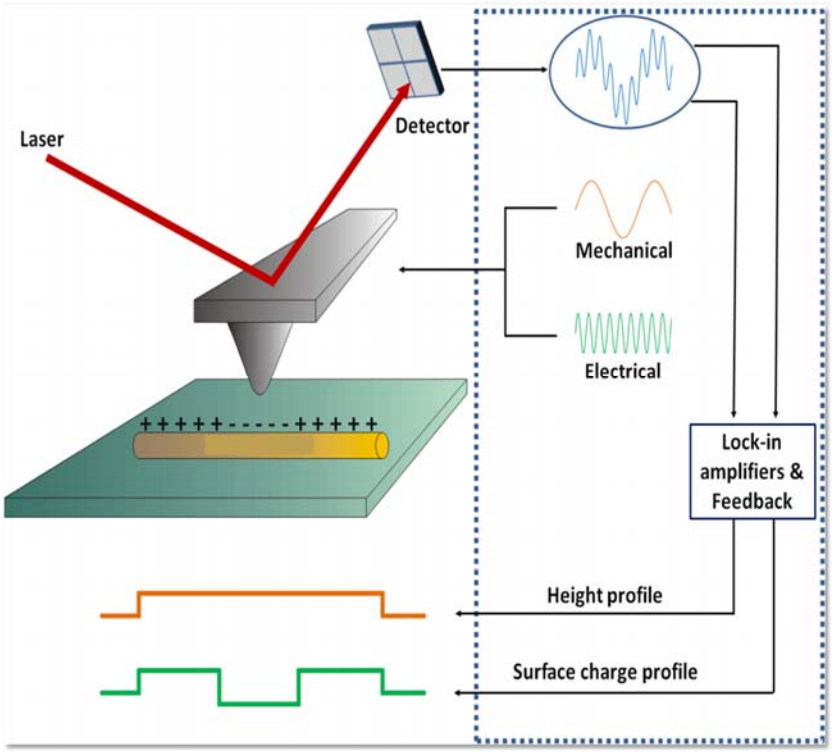

Figure 8. Illustration of a Scanning Kelvin Probe Microscopy (SKPM) setup.

Air Photoemission measurement system (APS)

Air photoemission systems are capable of measuring the ionization energy (IE) of a material. When light with photon energy > IE interacts with the material it liberates electrons at the surface, a phenomena that is known as the photoelectric effect. The electrons are detected using a modified Kelvin probe setup capable of measuring potential difference. The amount of detected electrons depends on the energy or wavelength of the incident light. Following Fowler`s analysis of photoemission, the cube root of the photoelectron yield can be plotted as a function of incident light intensity and thus give insight to the density of states near the Fermi Level.

Time-Resolved Photoluminescence (TRPL)

Time resolved photoluminescence studies the charge carrier dynamics in semiconductors and thus investigates directly the quality of the layers. The measurements are sensitive to essential parameters of the semiconductors such as surface effects, presence of dopants, energy transfer processes, defects and their passivation. There is a multitude of setups for time resolved photoluminescence measurements but common components are: pulsed laser sources (diode laser, LED or multi-photon excitation), single photon sensitive detector, means of separating the emission signal from the excitation light (monochromator or optical filters) and a unit to measure the time delay between excitation and fluorescence emission. The measurement of the time delay is repeated in a series of experiments to account for the statistical nature of the radiative emission in semiconductors. The final results are plotted into a histogram where the emission events are represented as a function of time after the excitation pulse.

4 Perovskite–Perovskite Homojunctions via Compositional Doping

Introduction

The p-n junction is a fundamental structure of semiconductor devices, crucial for transistors, diodes and thus all kinds of modern electronic systems. Light striking such a junction creates a voltage and electric current which is known as the photovoltaic effect. The underlying physical principles have been studied for decades leading to highly efficient conventional inorganic photovoltaics (PV). Since 2009 a new class of semiconductors, organic-inorganic lead halide perovskites, attracted much attention as solar cells based on this material have rapidly reached efficiencies exceeding 23%.[41] While perovskite photovoltaics can already compete with conventional photovoltaic absorbers such as silicon in terms of efficiency, some of their basic working principles are still not understood.[31,37,54–56] Among others, the distribution of the internal potential is still under debate, leaving the question unanswered weather perovskite PVs behave like p-n or p-i-n type structures.[30,55] In both cases the diode behavior of perovskite devices is likely dominated by band bending effects at the interface of the perovskite with either hole or electron transporting materials.[57] The resulting electric field causes a drift of carriers close to the interface. We assume that the field-assisted carrier transport diminishes with increasing distance from the interfaces leading to rather diffusion dominated transport mechanisms in the bulk. Electron and hole diffusion length of over 175 µm have been reported for perovskite single crystals but the diffusion length in polycrystalline films is often limited to 100 nm.[58] Improving transport is thus essential for the further development of perovskite solar cells as the transport properties limit

the maximum thickness of the absorber materials and hence the current that can be extracted. Improving the carrier diffusion length is difficult as it depends strongly on the morphology and thus on the deposition method of the perovskite. The charge drift can be increases by creating an additional interface within the perovskite absorber such as in a p-n junction of differently doped perovskite layers. The p-n junction promotes the separation of carriers and their extraction leading to reduced recombination Nevertheless, doping of perovskites is still very challenging. There has been a multitude of attempts to modify the perovskite electronic structure introducing heterovalent dopants.[59] Abdelhady et al. found strong electronic effects in a MAPI perovskite when adding small amounts of bismuth in the precursor solution.[60] In fact when Bi^{3+} was incorporated into the perovskite lattice structure it lead to a bandgap tuning of (∼300 meV) and a remarkable 10^4 fold enhancement in electrical conductivity (Figure 9). The sign of majority charges was thereby changed from positive to negative. Inspired by this work, researchers further explored the use of trivalent metal ions in the perovskite structure. Snaith et al. added a small amount of Al^{3+} in the precursor solution and found a reduced microstrain in the MAPI structure which resulted in a reduction of density of crystal defects but with negligible electronic effects.[61] In contrast Zhang et al. used Sb^{3+} and successfully doped a MAPI perovskite, increasing the electron density and elevating the quasi-Fermi energy level.[62] Nevertheless most of the fundamental scientific issues of heterovalent doping in perovskite remain unresolved. For instance, it is mostly unclear if the heterovalent dopants are periodically introduced in the lattice structure or if they segregate to the surface or how metal ions regulate the perovskites properties.[59] Furthermore, when heterovalent dopants are

incorporate into the perovskite structure they are likely to introduce lattice imperfections. How local morphology affects the optoelectronic properties of the perovskite is difficult to predict.[63,64]

Considering the difficulties of heterovalent doping, the previously reported defect assisted self-doping is an interesting alternative. Perovskites were observed to be self-doped by changing the ratio of the MAI and PbI_2 precursors.[65] MAI-rich (PbI_2-deficient) perovskites are p-type semiconductors while PbI_2-rich (MAI-deficient) materials are n-type. The unbalanced precursor ratios cause element defects (Pb, I, MA) that introduce electronic states close to the band edges. Surprisingly no deep trap states are created within the band gap as it would be expected for classic semiconductors.[66] Defect states are especially shallow due to the small effective masses of electrons and holes and the high dielectric constant of the perovskite.[66]

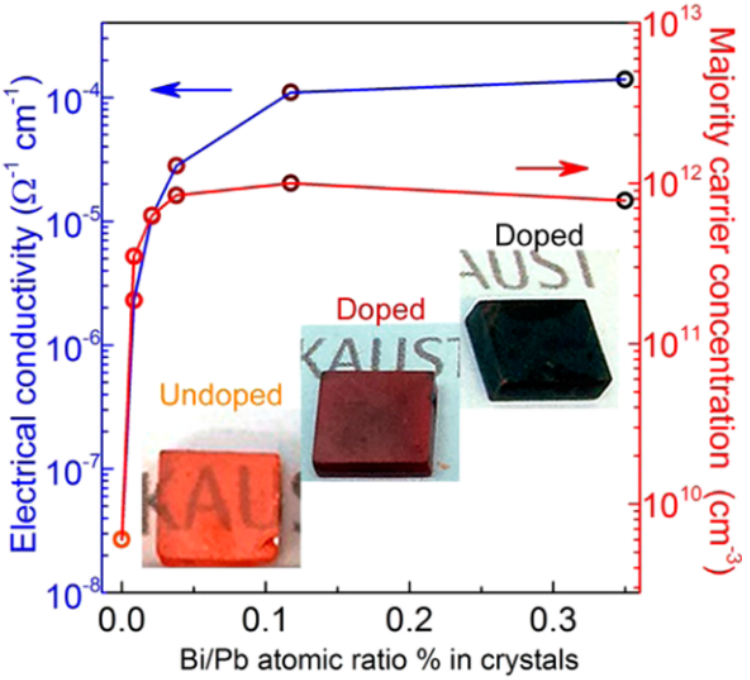

Figure 9. Conductivity and majority concentration of different crystals as a function of Bi/Pb atomic ratio % in the crystal.[67]

Here we present a perovskite p-n junction obtained by vacuum deposition of stoichiometrically-tuned methylammonium lead iodide films. We show the internal potential distribution of the p-n junction as measured by cross-sectional scanning Kelvin probe microscopy with a contact potential difference (CPD) of 250 mV between the doped perovskite layers. The p-n junction was sandwiched between organic charge selective layers. Devices built with the perovskite p-n junction showed photovoltage of 1095 mV and fill factor of 80%, which is large compared to cells built either with intrinsic film or single n- or p-type doped perovskite layers. The enhanced photovoltaic performance could be explained by the additional drift of carriers in a perovskite p-n junction

Experimental Section

Perovskite films deposition and diodes fabrication. ITO-coated glass substrates were subsequently cleaned with soap, water and isopropanol in an ultrasonic bath, followed by UV-ozone treatment. Substrate were transferred to a vacuum chamber integrated into a nitrogen-filled glovebox (H_2O and O_2 < 0.1 ppm) and evacuated to a pressure of 10^{-6} mbar. The vacuum chamber is equipped with six temperature controlled evaporation sources (Creaphys) fitted with ceramic crucibles. Three QCM sensors are used, two monitoring the deposition rates of each evaporation source and a third one close to the substrate holder monitoring the total deposition rate. For the TaTm HTL we used 2,20-(perfluoronaphthalene-2,6-diylidene) dimalononitrile (F_6-TCNNQ) as the organic dopant whereas for the C_{60} ETL, N1,N4-bis(tri-*p*-tolylphosphoranylidene)- benzene-1,4-diamine (PhIm). For thickness calibration, we first individually sublimed the charge transport materials and their dopants. A calibration factor was obtained by comparing the thickness inferred from the QCM sensors with that measured with a mechanical profilometer (Ambios XP1). Then these materials were co-sublimed at temperatures ranging from 135-160 °C for the dopants and 250 °C for the pure charge transport molecules, and the evaporation rate was controlled by separate QCM sensors and adjusted to obtain the desired doping concentration. In general, the deposition rate for TaTm and C_{60} was kept constant at 0.8 Å/s while varying the deposition rate of the dopants to 0.06 Å/s for F_6-TCNNQ and 0.2 Å/s for PhIm during co-deposition. Pure TaTm and C_{60} layers were deposited at a rate of 0.5 Å/s. 40 nm thick doped layers (TaTm:F_6-TCNNQ and C_{60}:PhIm) and 10 nm thick intrinsic layers (TaTm and C_{60}) were used for the solar cell fabrication. After HTL deposition, the

chamber was vented with dry N_2 to replace the crucibles with those containing the starting materials for the perovskite deposition, PbI_2 and MAI. The vacuum chamber was evacuated again to a pressure of 10^{-6} mbar, and the perovskite films were then obtained by co-deposition of the two precursors. For production of the different perovskite layers the MAI deposition rate was kept constant at 0.8 Å/s while varying the deposition rate of PbI_2 between 0.4 Å/s (*p*-type), 0.5 Å/s (intrinsic) and 1.2 Å/s (*n*-type). The source temperature of the MAI was kept constant at 70 °C and that of the PbI_2 varied accordingly between 255 °C and 300 °C. The doped and intrinsic perovskite were deposited to a final thickness of 600 nm. The perovskite *p*-n junction was built by depositing a 300 nm thick *n*-MAPI layer onto a 300 nm thick *p*-MAPI film. After deposition of the perovskite films, the chamber was vented and the crucibles replaced with those containing C_{60} and PhIm, and evacuated again to a pressure of 10^{-6} mbar. The devices were completed depositing a film of pure C_{60} and one of the doped ETL (C_{60}:PhIm), with 10 and 40 nm thicknesses, respectively. Finally the substrates were transferred to a second vacuum chamber where the silver top contact (100 nm thick) was deposited.

Infrared (IR) spectroscopy characterization. For the IR measurements, MAPI films were deposited on both side polished, low doped Si wafers. A thin layer of C_{60} was evaporated on the Si substrate before MAPI deposition, to ensure the same growth conditions as for the solar cells. IR measurements were performed with a Bruker Vertex 80v spectrometer. Spectra were measured with the samples in vacuum (~2 mbar) using a DLaTGS detector and non-polarized light at normal incidence. Spectral resolution was set to 4 cm^{-1} and all spectra are referenced to the spectrum of the bare C_{60}/Si substrate.

Surface and cross-sectional KP measurements. The surface Kelvin probe measurements were performed with a macroscopic Kelvin probe from KP Technology in air. The work function of the gold probe was determined with a freshly cleaved HOPG reference directly before the measurement. For the cross section SKPM measurement, we used a Zeiss/DME integrated AFM/SEM system. To reveal the cross section a hole was milled into the device by a Gallium Focused-Ion-Beam (Ga-FIB). In a first step a rough hole was milled at 2 nA for 180 s. Due to the setup of the FIB the cross section has an angle of 54° towards the surface normal. The cross section was then polished with a beam current of 100 pA for 600 s, achieving a smooth surface. While scanning the cross section with the cantilever, the topography, contact potential and the phase are measured simultaneously. We used the one pass amplitude modulated technique for the Kelvin probe data. We used conductive Pt/Ir coated ATEC-NCPt-50 cantilevers. They have a length of 160 µm, a width of 45 µm and a thickness of 4.6 µm. Their force constant is 45 N / m, the resonance is at about 335 kHz and they have a tip radius of curvature of < 20 nm.

Device characterization. The EQE was estimated using the cell response at different wavelength (measured with a white light halogen lamp in combination with band-pass filters), where the solar spectrum mismatch is corrected using a calibrated Silicon reference cell. The current density-voltage (JV) characteristics were obtained using a Keithley 2612A source measure unit under white light illumination using a solar simulator by Abet Technologies (model 10500 with an AM1.5G xenon lamp as the light source). The scan rate was 0.1 V/s. Before each measurement, the exact light intensity

was determined using a calibrated Si reference diode equipped with an infrared cut-off filter (KG-3, Schott).

Results and discussion

In the co-evaporation process the precursor ratios were changed by increasing the evaporation rate of PbI_2 while maintaining the evaporation speed of MAI constant. These ratios were determined from the calibrated quartz crystal sensor reading during the evaporation process. The grazing incidence X-ray diffraction (GIXRD) pattern confirms the formation of a perovskite thin film with high crystallinity for the p-type perovskite and lower crystallinity for the n-type perovskite film (Figure 10).[52]

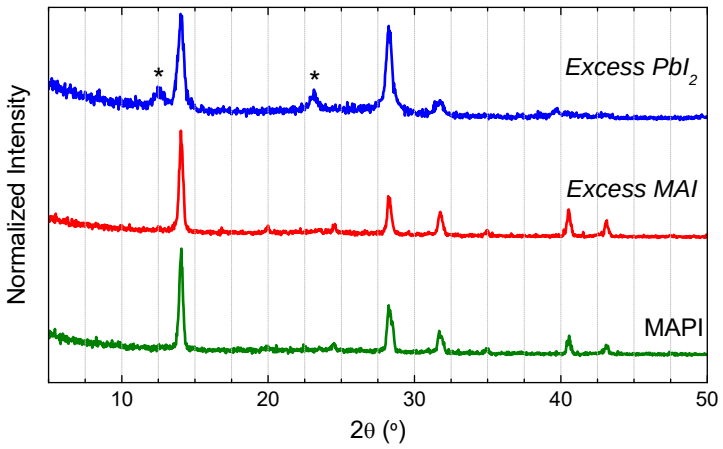

Figure 10. XRD patterns of MAPI thin films with different MAI/PbI_2 ratios. The stars indicate diffractions corresponding to PbI_2.

The diffraction pattern of the n-MAPI sample shows the formation of the perovskite phase with lower degree of crystallinity and smaller crystals (wider diffraction peaks), as well as additional weak diffractions indicating the presence of a residual PbI_2 phase. Both the n- and the p-type perovskite

show the characteristic features of a MAPI absorption spectra with an onset at 780 nm indicating that the band gap remains unchanged (Figure 11a)

Mid-IR spectroscopy was performed to confirm the PbI_2 to MAI ratios in the perovskite films. While far-IR couples to lead halide phonons[68], mid-IR is sensitive to internal vibrations of the MA-cation.[69] Thus it is possible to use the mid-IR spectra as a measurement of the MAI content. Figure 11b shows the region with the most pronounced vibrational peak, the N-H symmetric and asymmetric stretch vibration. The absolute position of the peaks does not change showing that all MA cations experience the same environment. Nevertheless the absolute peak strength is different and analysis of the peak area revealed that the MAI-rich film (p-type) contains approximately 50% more MA compared to the MAI-poor film (n-type). The standard film lies in the middle as expected. While the IR-measurements give no direct information about the halide content it is likely that the higher MA-cation content is accompanied with a higher content of iodine.

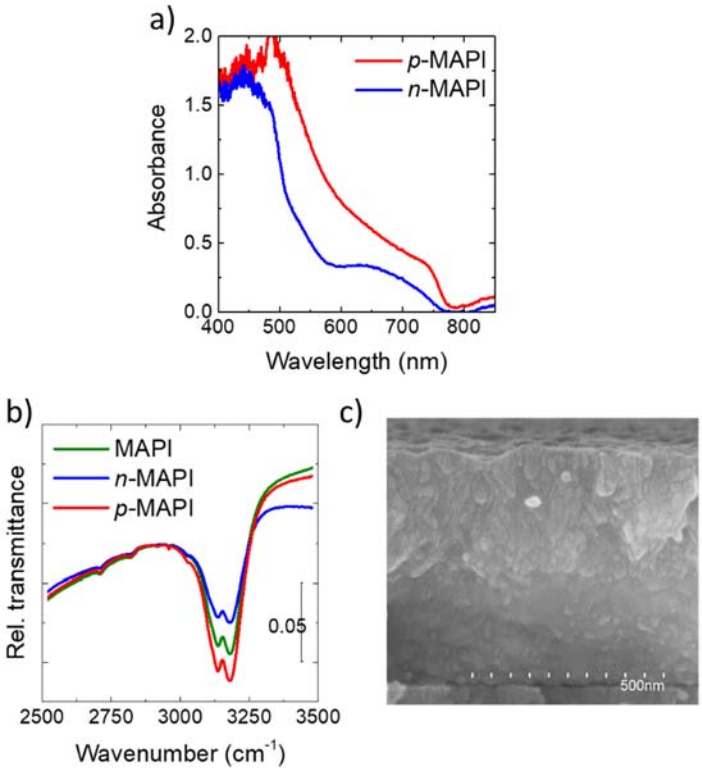

Figure 11. Characterization of the p- and n-type films. (a) Optical absorption spectra of 300 nm thick p-, and n-MAPI layers. (b) IR relative transmittance spectra of the N−H stretching vibration for reference, n-, and p-type MAPI films. All films have a thickness of around 300 nm and were deposited on Si wafers. The change of the N−H stretching vibration peak strength is clear proof for different MA concentrations. (c) SEM images of pn-junction cross section.

To investigate the electronic impact of the different precursor ratios we performed macroscopic Kelvin probe measurements on the perovskites films in ambient conditions. The measured work functions are 4.6 eV for p-MAPI, 4.3 eV for n-MAPI, and 4.45 eV for our reference intrinsic (i-MAPI) film. These values show indeed the expected trend from the stoichiometry change, assuming that the mid-gap is approximately at 4.4 eV.[70]

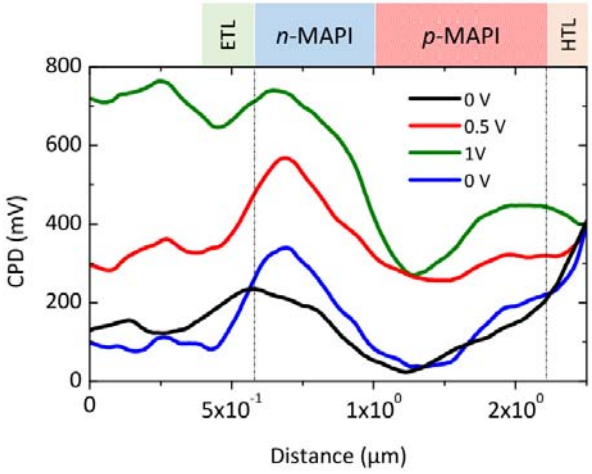

Figure 12. CPD profile of a p-n junction solar cell under illumination and with increasing applied bias. The bias was increased from 0 V (black), to 0.5 V (red), to 1 V (green) and then back again to 0 V (blue). Bias was applied for ~1 hour. The sample was illuminated with an LED attached to the sample holder.

From these measurements it appears that the layers are only slightly doped. We note however that the work function of a material is highly influenced by the substrates, surface defects or adsorbates. Clearly, an in situ study of an n−p MAPI interface during growth via photoemission spectroscopy would be highly desirable. However, this is extremely challenging as our growth conditions for vacuum-deposited MAPI do not meet the requirements for photoelectron spectroscopy[71]. To get further inside into the electronic behavior of the doped perovskite layers we performed SKPM measurements on the cross section of full diodes. We compared an intrinsic perovskite layer with a double p-MAPI/n-MAPI layer which were sandwiched between organic semiconductors used as charge transport layers. The selective contact layers consisted of thick doped layers (40nm) and a thinner intrinsic

film (10nm) in contact with the perovskite. SKPM on solar cell cross sections has been previously reported for organic and perovskite solar cells.[55,72,73]

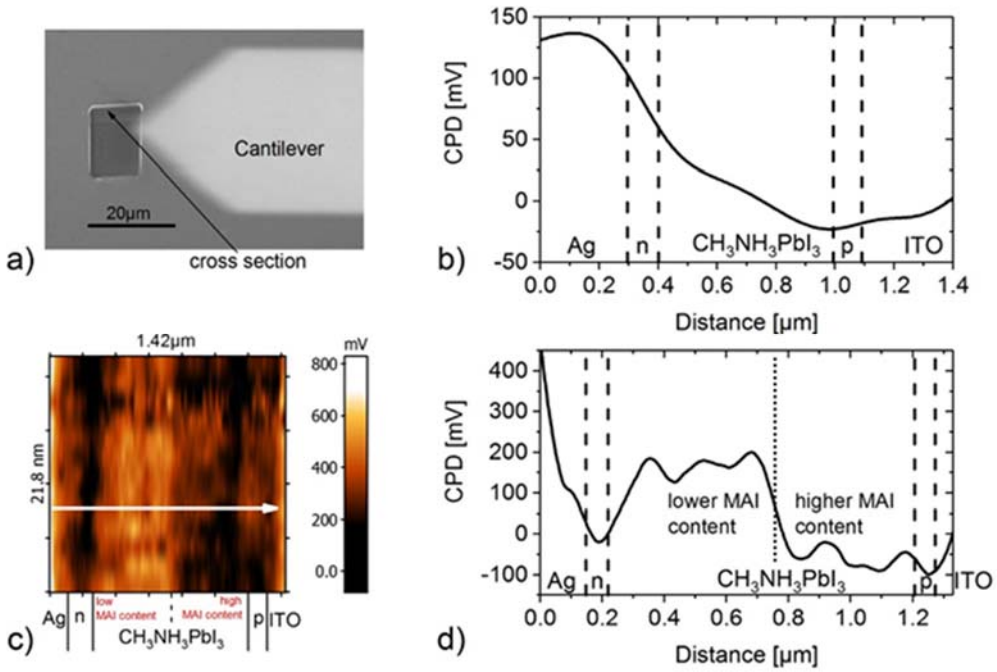

Figure 13. SKPM characterization of planar solar cells with either an intrinsic MAPI (500 nm) or a p-MAPI/n-MAPI bilayer (600 nm) as the absorber. (a) SEM image of the AFM cantilever approaching the FIB-exposed solar cell cross section. (b) CPD profile of a reference vacuum- deposited solar cell. We find an almost constant potential drop over the absorber layer. (c) SKPM image of the cross section for a homojunction solar cell. Already in this representation, a contrast change in the middle of the absorber cell is visible. (d) CPD profile of a p−n junction solar cell. We find a clear potential change at the MAPI p−n junction. The distance is larger than the real layer thickness as the FIB was performed at 54° with respect to the surface normal.

We used an integrated SEM-AFM system in a SKPM mode. The cross section was prepared using a FIB leading to a very smooth surface (topology) and thus avoiding crosstalk between the surface topology and the SKPM signal. Figure 13a shows and SEM image of the cantilever approaching the solar cell cross section. As a reference we first measured the CPD profile of a reference solar cell Figure 13b. Here we find a rather constant drop in the potential as it would be expected for a p-i-n solar cell. In contrast we observed a step like behavior for the solar cell stack containing the p- and n-MAPI Figure 13d. The voltage difference of around 250 mV was stable over the scanning time of 2 hours. It is noteworthy that the potential difference is probably underestimated due to the amplitude modulated scanning mode[74]. We also performed stability measurements under light and applied bias, as shown in Figure 12. If a bias is applied the step-like profile of the potential increases and stays stable over the time of the measurement. Most importantly, the effect of an applied bias is reversible and when the sample is brought back to 0 V, the potential step is still present, indicating that the homojunction is fairly stable under illumination and with an external bias. These experiments are a direct proof of a stable perovskite-perovskite homojunction and show that we are able to fine-tune its electronic behavior. The very same devices that were measured in the SKPM setup were characterized as solar cells.

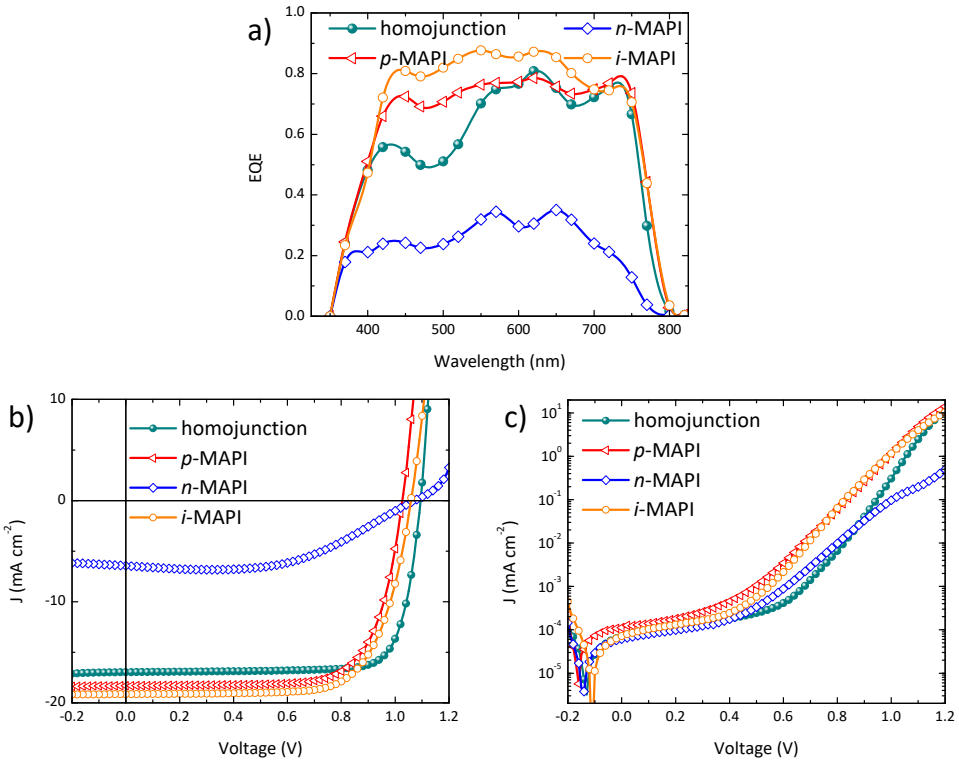

Figure 14. Optoelectronic characterization of solar cells with 600 nm thick MAPI absorbing layers. The MAPI films are either p-type, n-type, or intrinsic (i-MAPI). The perovskite homojunction was built by depositing a 300 nm thick n-MAPI onto a 300 nm p-MAPI. (a) EQE spectra. JV curves (b) under illumination and (c) in the dark for a series of devices varying the MAPI absorber.

Figure 14 shows the JV characteristics of solar cells containing differently doped perovskite absorbing layers under illumination. Solar cells with p-type doped or intrinsic perovskite absorbers show very comparable performance with PCEs of 13.53 %, 15.1 % and FF of 72 % and 71 %, respectively. We observed only a lower V_{oc} for the p-type (1027 mV) perovskite with respect to the intrinsic one (1059 mV), which might be due to the Fermi level

difference observed by Kelvin probe. In contrast the n-type doped perovskite diode is poorly performing with a PCE of 7.84 %. The diode shows a very low J_{sc} of 6.44 mA cm^{-2} which is most likely due to the lower absorption coefficient of the n-perovskite (Figure 11a). The lower MAI content results in an excess of PbI_2 in the film, which hinders both the photocarrier generation and separation/transport. The hindered charge injection and transport within the diode is evident from the JV characteristic measured in the dark and under illumination, where the FF is as low as 54.4 %. The high V_{oc} indicates that non-radiative charge recombination is not the main process limiting the charge collection. The diode containing the perovskite p-n junction is surprisingly well performing considering the presence of a 300 nm thick poorly absorbing n-perovskite. Especially the V_{oc} (1094 mV) and FF (80) improve compared to all the other devices. Considering the difference in work function observed for the p- and n-MAPI (−4.6 and −4.3 eV), one could expect a difference in the majority carrier concentrations in the two materials, i.e., a larger hole (electron) concentration in the p-MAPI (n-MAPI). If we assume the intrinsic material to behave as ambipolar (as often reported in the literature),[70] then the separation and selective transport of photogenerated electrons and holes in p- and n- MAPI would be influenced by the respective carrier conductivities in the two regions of the active layer[75]. The EQE of the diode containing the p-n junction follows in shape and height the one of the n-perovskite up to a wavelength of 570nm. The reason for the lower spectra response in the blue is not yet fully understood. The front perovskite film (p-MAPI) is strongly absorbing in this portion of the spectrum; hence, red photons will be absorbed more homogeneously along the whole film thickness. As the EQE is higher for low-energy photons, it implies that only

electron− hole pairs generated toward the homojunction can reach the selective contacts, most likely due to the favorable gradient of the quasi-Fermi energies.

In summary, we show the fabrication of a vertical perovskite-perovskite homojunction and measured the CPD at the device cross section. The potential difference between the p-type doped and the n-type doped perovskite was as high as 250 mV. The homojunction was stable over time even under illumination or when a bias was applied. When incorporated into a planar device the non-radiative recombination was reduced as indicated by a high V_{oc} (1.1 V) and the carrier extraction was improved, as testified by the high fill factor of 80%. This work is an important step towards a novel design of perovskite solar cells using homo- or heterojunctions to further improve the charge separation or recombination.

THE JOURNAL OF PHYSICAL CHEMISTRY Letters
Cite This: J. Phys. Chem. Lett. 2018, 9, 2770−2775
Letter
pubs.acs.org/JPCL

Perovskite−Perovskite Homojunctions via Compositional Doping

Benedikt Dänekamp,[†,#] Christian Müller,[‡,§,#] Michael Sendner,[§,∥] Pablo P. Boix,[†] Michele Sessolo,*[,†] Robert Lovrincic,*[,‡,§] and Henk J. Bolink[†]

[†]Instituto de Ciencia Molecular, Universidad de Valencia, C/J. Beltrán 2, 46980 Paterna, Spain
[‡]Institute for High Frequency Technology, TU Braunschweig, Schleinitzstrasse 22, 38106 Braunschweig, Germany
[§]InnovationLab, Speyerer Strasse 4, 69115 Heidelberg, Germany
[∥]Kirchhoff Institute for Physics, Heidelberg University, Im Neuenheimer Feld 227, 69120 Heidelberg, Germany

Supporting Information

ABSTRACT: One of the most important properties of semiconductors is the possibility of controlling their electronic behavior via intentional doping. Despite the unprecedented progress in the understanding of hybrid metal halide perovskites, extrinsic doping of perovskite remains nearly unexplored and perovskite−perovskite homojunctions have not been reported. Here we present a perovskite−perovskite homojunction obtained by vacuum deposition of stoichiometrically tuned methylammonium lead iodide (MAPI) films. Doping is realized by adjusting the relative deposition rates of MAI and PbI_2, obtaining p-type (MAI excess) and n-type (MAI defect) MAPI. The successful stoichiometry change in the thin films is confirmed by infrared spectroscopy, which allows us to determine the MA content in the films. We analyzed the resulting thin-film junction by cross-sectional scanning Kelvin probe microscopy (SKPM) and found a contact potential difference (CPD) of 250 mV between the two differently doped perovskite layers. Planar diodes built with the perovskite−perovskite homojunction show the feasibility of our approach for implementation in devices.

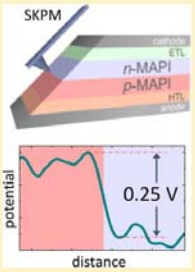

Modern electronics comprises a wide spectrum of components and devices, most of which rely on semiconducting materials. One of the most relevant aspects of semiconductors is the possibility of modulating their electronic properties through doping. The quantitative introduction of selected impurities altering the material stoichiometry allows control of the type (electron, hole) and concentration of charge carriers, leading to n- or p-type semiconductors. Of particular importance for several applications is the interface between semiconductors of opposite doping type, the p−n junction. The underlying physical principles of p−n junctions have been studied for decades, leading to the first efficient photovoltaics (PVs) based on conventional inorganic semiconductors. Hybrid organic−inorganic metal halide perovskites, such as methylammonium lead iodide ($CH_3NH_3PbI_3$, MAPI) have the potential to radically transform the way optoelectronics is conceived, combining the favorable properties of both organic and inorganic compounds within a single material. Hybrid perovskites are now at the forefront of emerging PV materials, thanks to their constantly improving power conversion efficiencies (PCEs), which are now exceeding 22%.[1−4] Besides such fast progress, up to now, extrinsic doping of perovskite remains nearly unexplored,[5] and perovskite−perovskite homojunctions have only be obtained in lateral structures.[6] In fact, when heterovalent metals are incorporated into the perovskite lattice, they are likely to introduce lattice distortions, with strong effect on the electronic properties of the perovskite.[7,8] This strong structure−property relationship usually masks the actual effect of the dopants, making perovskites rather insensitive to the insertion of other metal species.[9,10] Additionally, the type of substrate used for the thin-film growth has a direct effect on the energy bands and Fermi level positions,[11,12] further complicating the design of doped compounds. Considering these difficulties, other strategies have been explored in order to obtain doped perovskite films. For example, p-doping of $MAPbI_3$ via exposure to I_2 gas was recently presented.[13] Alternatively, the defect-assisted self-doping could provide a path for the deposition of p- or n-type compounds as it has been reported that MAI-rich MAPI films are p-type while MAI-deficient compounds are n-type.[14] The unbalanced precursor ratios cause element defects (Pb, I, MA) that introduce electronic states close to the band edges but not deep traps within the band gap as would be expected for classic semiconductors.[15] Defect states are especially shallow due to the small effective masses of electrons and holes and the high dielectric constant of the perovskite.[16] On the basis of this principle, devices with vertical and lateral cell configurations can be switched upon application of a weak electric field due to ion drift, which leads to the formation of reversible p−i−n structures.[17] Most studies on perovskite electronic and optical properties are carried out on materials deposited by solution processes. Despite the high level of control on the perovskite morphology through engineering of the deposition conditions,

Received: March 29, 2018
Accepted: May 10, 2018
Published: May 10, 2018

DOI: 10.1021/acs.jpclett.8b00964
J. Phys. Chem. Lett. 2018, 9, 2770−2775

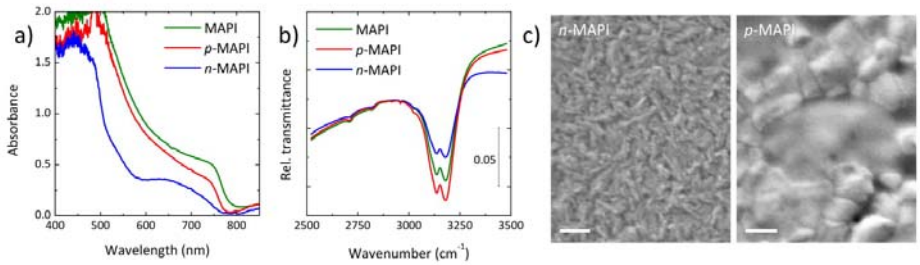

Figure 1. Characterization of the p- and n-type films. (a) Optical absorption measurements of 300 nm thick reference, p-, and n-MAPI layers. (b) IR relative transmittance spectra of the N−H stretching vibration for reference, n-, and p-type MAPI films. All films have a thickness of around 300 nm and were deposited on Si wafers. The change of the N−H stretching vibration peak strength is clear proof for different MA concentrations. (c) SEM images of the surface of the n- and p-MAPI films. The scale bar corresponds to 200 nm.

it is not feasible (if not impossible) to prepare a perovskite double layer entirely from solution due to the unavoidable redissolution of the underlying film. For this purpose, vacuum deposition is a more suited technique and, when applied to perovskites, can lead to high-performing materials of comparable quality.[18,19] Importantly, vacuum deposition methods are intrinsically additive, such that multilayer structures can be readily prepared without the need for orthogonal solvents.[20]

Here we present a perovskite−perovskite homojunction obtained by vacuum co-deposition of stoichiometrically tuned $MAPbI_3$ films. Doping is realized by adjusting the relative deposition rates of MAI and PbI_2 in MAI-rich (herein referred to as p-MAPI) or MAI-deficient (n-MAPI) perovskite films. The successful stoichiometry change in the thin films is confirmed by infrared spectroscopy, which allows us to determine the MA content. We analyzed the resulting thin-film junction by cross-sectional scanning Kelvin probe microscopy (SKPM) and found a contact potential difference (CPD) of 250 mV between the two differently doped perovskite layers. This homojunction structure was sandwiched between organic charge-selective layers in order to evaluate its diode and PV characteristics. Devices built with the perovskite junction showed a promising photovoltage and fill factor, comparable to cells built with intrinsic perovskite films. These proof-of-concept results are encouraging as abrupt homojunctions have been scarcely investigated in the perovskite field and could be of interest for applications in PVs and other optoelectronic devices.

Differently doped perovskite layers were obtained by vapor phase co-deposition systematically changing the ratio of the MAI and PbI_2 deposition rates. The perovskite junction was obtained by depositing n-MAPI on top of a p-MAPI film. Detailed experimental conditions can be found in the Supporting Information. In the co-evaporation process, the precursor ratios were changed by increasing the evaporation speed of PbI_2 while maintaining the evaporation speed of MAI constant. These ratios were determined from the calibrated quartz crystal sensor reading during the evaporation process. The different perovskite absorbing layers were deposited varying the MAI/PbI_2 ratios, as detailed in the Experimental Section. The grazing incidence X-ray diffraction (GIXRD) analysis confirms the formation of a perovskite thin film with high crystallinity for the p-type perovskite, very similar to the reference MAPI thin films (see Supporting Information Figure S1a).[21] On the other hand, the diffraction pattern of the n-MAPI sample shows the formation of the perovskite phase with lower degree of crystallinity and smaller crystals (wider diffraction peaks), as well as additional weak diffractions indicating the presence of a residual PbI_2 phase.

Figure 1 shows some basic characterizations of the reference, n-, and p-MAPI films. All films show the characteristic features of the $MAPbI_3$ absorption spectra with an onset at 780 nm (Figure 1a), indicating that the band gap remains unchanged. The n-MAPI shows, however, a less steep absorption onset and lower absorbance, probably due to the presence of unreacted, wider-band-gap PbI_2. To quantify the actual MAI/PbI_2 ratios and hence correlate the deposition rates with the film stoichiometry, we performed mid-IR measurements on MAPI films on Si substrates. While the far-IR range is sensitive to the lead halide phonons,[22] all absorption peaks in the mid-IR can be assigned to internal vibrations of the $CH_3NH_3^+$ (MA) cation.[23] It is therefore possible to use the IR spectrum as a measure of the MA concentration in the film. Figure 1b shows the region of the most pronounced MA vibrational peak, the N−H symmetric and asymmetric stretch vibration, of n- and p-type MAPI and, for comparison, of a standard (intrinsic) MAPI film used in efficient solar cells.[19] While the peak shape and position for the N−H stretch vibration do not change between samples, indicating that all MA cations experience the same local environment, we see clear differences for the peak strengths. This measurement proves that different MAI/PbI_2 deposition ratios lead to films with differing MA concentrations. An analysis of the peak areas reveals that the MAI-rich film (p-type) contains approximately 50% more MA compared to the MAI-poor film (n-type), with the standard film in the middle. While our vibrational spectra contain no direct information on the presence of halides, it seems likely that a higher MA concentration is accompanied by an increase in iodide content (albeit not necessarily to the same extent) as the MA is incorporated via MAI. To assess the impact of the MAI/PbI_2 ratios on the electronic properties of the material, we first performed Kelvin probe measurement on the surfaces of the perovskite layers (in ambient conditions). The measured work functions are 4.6 eV for p-MAPI, 4.3 eV for n-MAPI, and 4.45 eV for our reference intrinsic (i-MAPI) film. These values show indeed the expected trend from the stoichiometry change. Assuming that the midgap is approximately at 4.4 eV,[13] it appears from this measurement that the reference film is intrinsic while the p- and n-materials are only very lightly doped. We note, however, that the work function measured by Kelvin probe on the surface of MAPI films might be strongly

DOI: 10.1021/acs.jpclett.8b00964
J. Phys. Chem. Lett. 2018, 9, 2770−2775

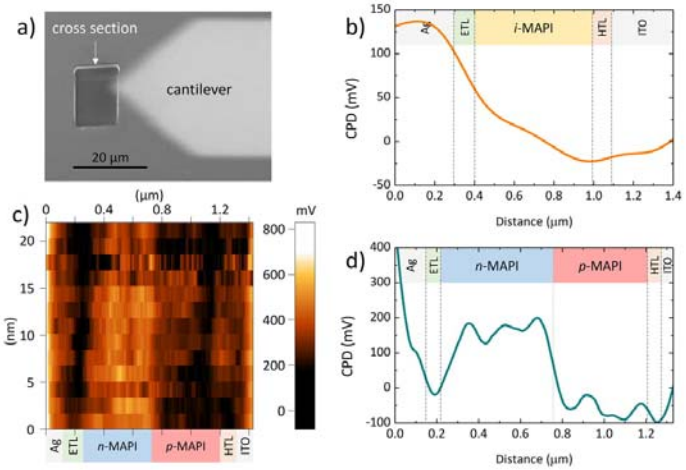

Figure 2. SKPM characterization of planar solar cells with either an intrinsic MAPI (500 nm) or a p-MAPI/n-MAPI bilayer (600 nm) as the absorber. (a) SEM image of the AFM cantilever approaching the FIB-exposed solar cell cross section. (b) CPD profile of a reference vacuum-deposited solar cell. We find an almost constant potential drop over the absorber layer. (c) SKPM image of the cross section for a homojunction solar cell. Already in this representation, a contrast change in the middle of the absorber cell is visible. (d) CPD profile of a p−n junction solar cell. We find a clear potential change at the MAPI p−n junction. The distance is larger than the real layer thickness as the FIB was performed at 54° with respect to the surface normal.

influenced by the substrate, surface defects, or adsorbates. Clearly, an in situ study of an n−p MAPI interface during growth via photoemission spectroscopy would be highly desirable. However, this is extremely challenging as our growth conditions for vacuum-deposited MAPI do not meet the requirements for photoelectron spectroscopy.[11]

Therefore, to gain more direct insight about these stoichiometrically tuned materials and their effect on the working principles of optoelectronic devices, we performed SKPM measurements on the cross sections of full diodes. In particular, we compared diodes employing a reference MAPI film with one including a p-MAPI/n-MAPI double layer. In these devices, the perovskite films were sandwiched between organic semiconductors used as charge transport materials. The selective contacts consisted of double layers, formed by a thick doped layer (40 nm) and a thinner intrinsic film in contact with the perovskite (10 nm). The electron and hole transport layers (ETL, HTL) consisted of fullerene (C_{60}) and *N*4,*N*4,*N*4″,*N*4″-tetra([1,1′-biphenyl]-4-yl)-[1,1′:4′,1″-terphenyl]-4,4″-diamine (TaTm), while the dopants employed were *N*1,*N*4-bis(tri*p*-tolylphosphoranylidene)benzene-1,4-diamine (PhIm) and 2,2′-(perfluoronaphthalene-2,6-diylidene)-dimalononitrile (F_6-TCNNQ), respectively. Thicknesses and doping concentrations were previously optimized.[19] The stacks were fully vacuum-deposited on prepatterned ITO using Ag as the reflective top contact. SKPM on solar cell cross sections has been previously reported for organic and perovskite solar cells.[24−26] We used an integrated SEM−AFM system to first expose the cross section via focused ion beam (FIB) milling and then scanned the cross section in the SKPM mode of the AFM, as detailed in the Supporting Information. The resulting cross sections were very smooth, and we therefore avoided crosstalk between the surface topology and the SKPM signal. Figure 2a shows an SEM image of the AFM tip as it scanned over the exposed solar cell cross section. For comparison, we first measured the CPD profile of a reference MAPI solar cell (Figure 2b). For such a device, we found a relatively constant drop of the potential from the electron- to the hole-selective contact across the perovskite absorber layer, as would be expected for a p−i−n type cell. In contrast, for the homojunction type cell, we observed a clear step in the potential at the interface between the p-MAPI and n-MAPI within the devices (Figure 2c). This step, of approximately 250 mV, was stable over the several hours that the measurement took (Figure 2d). We note that, due to the amplitude modulated scanning mode used here, the potential difference is probably underestimated.[27] We also performed measurements of the stability of the homojunction toward light and an applied bias (see Supporting Information Figure S2). The applied bias increases the potential step at the p−n interface. Interestingly, when the sample is brought back to 0 V, the potential step is still present, indicating that the homojunction is fairly stable under illumination and with an external bias. This measurement is direct proof for the formation of a perovskite−perovskite vertical homojunction. Even though the potential differences, and hence the doping levels, are only moderate, our results represent an important step toward full control of electronic properties in thin-film perovskite devices.

The same devices (with reference intrinsic i-MAPI and homojunction absorber layers), as well as diodes based on either a single layer of p- or n-MAPI films, were characterized as solar cells. Figure 3a depicts the device layout. Figure 3b shows the external quantum efficiency (EQE) spectra for the series of devices with stoichiometrically tuned doped perovskites. The spectral response of the cells with p-MAPI closely resembles that of the intrinsic perovskites, in accordance with its absorption spectrum (Figure 1a). The absolute EQE values

DOI: 10.1021/acs.jpclett.8b00964
J. Phys. Chem. Lett. 2018, 9, 2770−2775

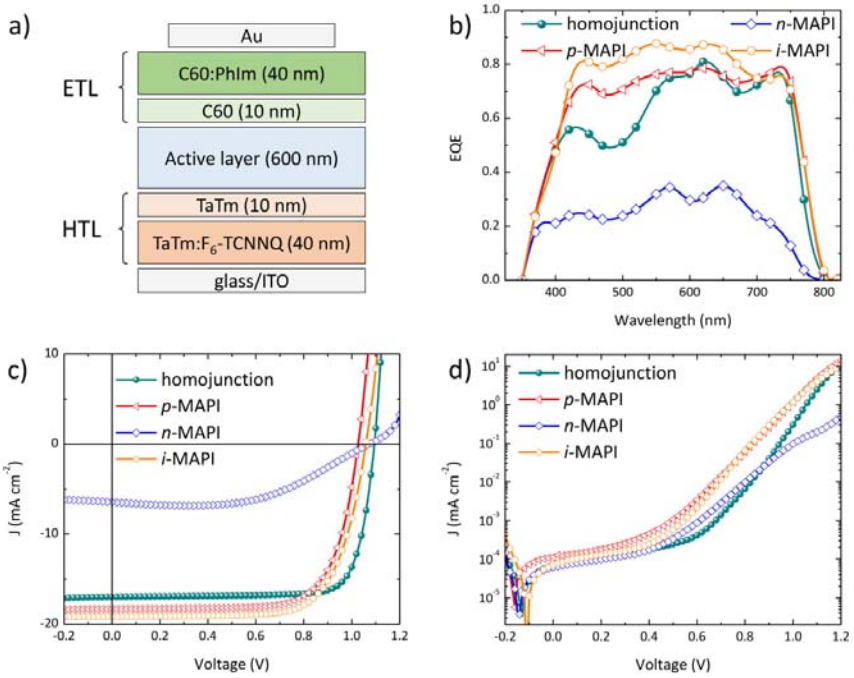

Figure 3. Optoelectronic characterization of solar cells with 600 nm thick MAPI absorbing layers. The MAPI films are either p-type, n-type, or intrinsic (i-MAPI). The perovskite homojunction was built by depositing a 300 nm thick n-MAPI onto a 300 nm p-MAPI. (a) Scheme of the solar cell layout. (b) EQE spectra. $J-V$ curves (c) under illumination and (d) in the dark for a series of devices varying the MAPI absorber.

are only 5−10% lower, resulting in a lower short-circuit current density of 18.3 mA cm^{-2} (J_{sc}, Figure 3c and Table 1).

Table 1. PV Parameters for Solar Cells with Different MAPI-Based Absorbers

absorber	thickness [nm]	V_{oc} [mV]	J_{sc} [mA cm^{-2}]	FF [%]	PCE [%]
i-MAPI	600	1059	20.1	71.1	15.1
p-MAPI	600	1027	18.3	72.0	13.53
n-MAPI	600	1072	6.4	54.4	3.8
homojunction	300/300	1095	16.8	79.7	14.7

The current density vs voltage ($J-V$) characteristics under illumination and in the dark (Figure 3c,d) for the intrinsic and p-MAPI cells are also rather similar. A small reduction in the open-circuit voltage (V_{oc}) from 1059 to 1027 mV was also observed, which might be due to the Fermi level difference observed for the intrinsic and p-type MAPI. Overall, at this MAI concentration, the p-MAPI is still capable of efficiently harvesting photons and collecting charge carriers (high EQE and fill factor of 72%), leading to high-performing devices.

The situation is different when the n-MAPI perovskite is used as the light absorber in a solar cell. Due to the strongly reduced optical density, the EQE spectrum is very low, resulting in a J_{sc} of only 6.4 mA cm^{-2}. The lower MAI content results in an excess of PbI_2 in the film, which hinders both the photocarrier generation and separation/transport. The hindered charge injection and transport within the diode is evident from the $J-V$ characteristic measured in the dark (Figure 3d) and under illumination (Figure 3c), where the FF is as low as 54.4%. On the other hand, the V_{oc} was observed to be rather high (1072 mV), meaning that nonradiative charge recombination is not the main process limiting charge collection in these devices. Unreacted PbI_2 has a wider band gap compared to the MAPI, but it has been reported to efficiently passivate the perovskite, justifying the concurrence of a low FF with high photovoltages.[28] The diode containing the perovskite homojunction has remarkable performance, with good rectification (Figure 3d). Especially the V_{oc} (1095 mV) and FF (~80%) improve substantially compared to those of the other devices, even if the resulting PCE is still inferior as compared to that of reference cells with stoichiometric MAPI.[19] Considering the difference in work function observed for the p- and n-MAPI (−4.6 and −4.3 eV), one could expect a difference in the majority carrier concentrations in the two materials, i.e., a larger hole (electron) concentration in the p-MAPI (n-MAPI). If we assume the intrinsic material to behave as ambipolar (as often reported in the literature),[13] then the separation and selective transport of photogenerated electrons and holes in p- and n-MAPI would be influenced by the respective carrier conductivities in the two regions of the active layer.[29] The origin of the lower spectral response in the blue to green region (Figure 3b) is not yet clearly understood. The front perovskite film (p-MAPI) is strongly absorbing in this portion of the spectrum; hence, red photons will be absorbed more

DOI: 10.1021/acs.jpclett.8b00964
J. Phys. Chem. Lett. 2018, 9, 2770−2775

homogeneously along the whole film thickness. As the EQE is higher for low-energy photons, it implies that only electron–hole pairs generated toward the homojunction can reach the selective contacts, most likely due to the favorable gradient of the quasi-Fermi energies.[29] One possible way to increase the current density arising from such a device might be the fabrication of MAPI homojunctions with asymmetric thicknesses of the p-MAPI and n-MAPI films. Motivated by the good PV performance of the MAPI–MAPI homojunctions, we also prepared devices without any organic transport layers, i.e., with the perovskite homojunction directly sandwiched in between ITO and a gold electrode. Such devices were however found to be systematically shorted, independently of the thickness (up to 1 μm) of the perovskite absorber. This phenomenon is most likely due to the penetration of the evaporated metal deep into the "soft" perovskite film. While hole-conductor-free perovskite solar cells have been demonstrated,[30,31] those devices still employed a thick TiO_2 layer in between the transparent front contact and the perovskite film. This additional layer would indeed protect the device from direct contact between the two electrodes. Avenues to address this issue in view of the development of pure metal–perovskite devices are being explored.

In summary, we demonstrate the fabrication of a vertical MAPI homojunction, obtained by vacuum co-deposition of stoichiometrically tuned MAPI films. By means of Kelvin probe measurements on the surface and through the cross section of the junction, we showed a junction potential exceeding 250 mV. When incorporated into planar devices using organic semiconductors as the charge transport materials, the MAPI homojunction shows good charge extraction and limited recombination, as testified by the high fill factor (80%) and high photovoltage (1.1 V). This work represents a proof-of-principle for the development of perovskite optoelectronic devices, which could benefit from the use of homo- or heterojunctions to further improve the charge separation or recombination.

■ ASSOCIATED CONTENT

Supporting Information

The Supporting Information is available free of charge on the ACS Publications website at DOI: 10.1021/acs.jpclett.8b00964.

Materials, perovskite film fabrication, device fabrication, XRD measurements, IR spectroscopy and SKPM setup, and SKPM measurements under illumination and under bias (PDF)

■ AUTHOR INFORMATION

Corresponding Authors

*E-mail: michele.sessolo@uv.es (M.S.).
*E-mail: r.lovrincic@tu-braunschweig.de (R.L.).

ORCID

Pablo P. Boix: 0000-0001-9518-7549
Michele Sessolo: 0000-0002-9189-3005
Robert Lovrincic: 0000-0001-5429-5586
Henk J. Bolink: 0000-0001-9784-6253

Author Contributions

#B.D. and C.M. contributed equally to this work

Notes

The authors declare no competing financial interest.

■ ACKNOWLEDGMENTS

Financial support is acknowledged from the European Union H2020 project INFORM (Grant 675867), the German Federal Ministry of Education and Research (FKZ 13N13656 and 13N13657), the Spanish Ministry of Economy and Competitiveness (MINECO) via the Unidad de Excelencia María de Maeztu MDM-2015-0538, MAT2017-88821-R, MAT2017-88905-P, PCIN-2015-255, and the Generalitat Valenciana (Prometeo/2016/135 and SEJI2017/2017/012). M.S. and P.P.B. thank the MINECO for their RyC contracts.

■ REFERENCES

(1) Lee, M. M.; Teuscher, J.; Miyasaka, T.; Murakami, T. N.; Snaith, H. J. Efficient Hybrid Solar Cells Based on Meso-Superstructured Organometal Halide Perovskites. *Science* **2012**, *338*, 643–647.

(2) Yang, W. S.; Noh, J. H.; Jeon, N. J.; Kim, Y. C.; Ryu, S.; Seo, J.; Seok, S. I. High-Performance Photovoltaic Perovskite Layers Fabricated through Intramolecular Exchange. *Science* **2015**, *348*, 1234–1237.

(3) Saliba, M.; Matsui, T.; Seo, J.-Y.; Domanski, K.; Correa-Baena, J.-P.; Nazeeruddin, M. K.; Zakeeruddin, S. M.; Tress, W.; Abate, A.; Hagfeldt, A.; et al. Cesium-Containing Triple Cation Perovskite Solar Cells: Improved Stability, Reproducibility and High Efficiency. *Energy Environ. Sci.* **2016**, *9*, 1989–1997.

(4) Yang, W. S.; Park, B.-W.; Jung, E. H.; Jeon, N. J.; Kim, Y. C.; Lee, D. U.; Shin, S. S.; Seo, J.; Kim, E. K.; Noh, J. H.; et al. Iodide Management in Formamidinium-Lead-Halide–Based Perovskite Layers for Efficient Solar Cells. *Science* **2017**, *356*, 1376–1379.

(5) Abdelhady, A. L.; Saidaminov, M. I.; Murali, B.; Adinolfi, V.; Voznyy, O.; Katsiev, K.; Alarousu, E.; Comin, R.; Dursun, I.; Sinatra, L.; et al. Heterovalent Dopant Incorporation for Bandgap and Type Engineering of Perovskite Crystals. *J. Phys. Chem. Lett.* **2016**, *7*, 295–301.

(6) Ou, Q.; Zhang, Y.; Wang, Z.; Yuwono, J. A.; Wang, R.; et al. Strong Depletion in Hybrid Perovskite p-n Junctions Induced by Local Electronic Doping. *Adv. Mater.* **2018**, *30*, 1705792.

(7) Filip, M. R.; Eperon, G. E.; Snaith, H. J.; Giustino, F. Steric Engineering of Metal-Halide Perovskites with Tunable Optical Band Gaps. *Nat. Commun.* **2014**, *5*, 5757.

(8) Nayak, P. K.; Sendner, M.; Wenger, B.; Wang, Z.; Sharma, K.; Ramadan, A. J.; Lovrinčić, R.; Pucci, A.; Madhu, P. K.; Snaith, H. J. Impact of Bi^{3+} Heterovalent Doping in Organic–Inorganic Metal Halide Perovskite Crystals. *J. Am. Chem. Soc.* **2018**, *140*, 574–577.

(9) Wang, J. T.-W.; Wang, Z.; Pathak, S.; Zhang, W.; deQuilettes, D. W.; Wisnivesky-Rocca-Rivarola, F.; Huang, J.; Nayak, P. K.; Patel, J. B.; Mohd Yusof, H. A.; et al. Efficient Perovskite Solar Cells by Metal Ion Doping. *Energy Environ. Sci.* **2016**, *9*, 2892–2901.

(10) Pérez-del-Rey, D.; Forgács, D.; Hutter, E. M.; Savenije, T. J.; Nordlund, D.; Schulz, P.; Berry, J. J.; Sessolo, M.; Bolink, H. J. Strontium Insertion in Methylammonium Lead Iodide: Long Charge Carrier Lifetime and High Fill-Factor Solar Cells. *Adv. Mater.* **2016**, *28*, 9839–9845.

(11) Olthof, S.; Meerholz, K. Substrate-Dependent Electronic Structure and Film Formation of $MaPbi_3$ Perovskites. *Sci. Rep.* **2017**, *7*, 40267.

(12) Schulz, P.; Edri, E.; Kirmayer, S.; Hodes, G.; Cahen, D.; Kahn, A. Interface Energetics in Organo-Metal Halide Perovskite-Based Photovoltaic Cells. *Energy Environ. Sci.* **2014**, *7*, 1377–1381.

(13) Zohar, A.; Levine, I.; Gupta, S.; Davidson, O.; Azulay, D.; Millo, O.; Balberg, I.; Hodes, G.; Cahen, D. What Is the Mechanism of $MAPbI_3$ P-Doping by I_2? Insights from Optoelectronic Properties. *ACS Energy Lett.* **2017**, *2*, 2408–2414.

(14) Wang, Q.; Shao, Y.; Xie, H.; Lyu, L.; Liu, X.; Gao, Y.; Huang, J. Qualifying Composition Dependent p and n Self-Doping in $CH_3NH_3PbI_3$. *Appl. Phys. Lett.* **2014**, *105*, 163508–163508.

DOI: 10.1021/acs.jpclett.8b00964
J. Phys. Chem. Lett. 2018, 9, 2770–2775

(15) Yin, W.-J.; Shi, T.; Yan, Y. Unique Properties of Halide Perovskites as Possible Origins of the Superior Solar Cell Performance. *Adv. Mater.* **2014**, *26*, 4653−4658.
(16) Kim, J.; Lee, S.-h.; Lee, J. H.; Hong, K.-h. The Role of Intrinsic Defects in Methylammonium Lead Iodide. *J. Phys. Chem. Lett.* **2014**, *5*, 1312−1317.
(17) Xiao, Z.; Yuan, Y.; Shao, Y.; Wang, Q.; Dong, Q.; Bi, C.; Sharma, P.; Gruverman, A.; Huang, J. Giant Switchable Photovoltaic Effect in Organometal Trihalide Perovskite Devices. *Nat. Mater.* **2015**, *14*, 193.
(18) Hsiao, S.-Y.; Lin, H.-L.; Lee, W.-H.; Tsai, W.-L.; Chiang, K.-M.; Liao, W.-Y.; Ren-Wu, C.-Z.; Chen, C.-Y.; Lin, H.-W. Efficient All-Vacuum Deposited Perovskite Solar Cells by Controlling Reagent Partial Pressure in High Vacuum. *Adv. Mater.* **2016**, *28*, 7013−7019.
(19) Momblona, C.; Gil-Escrig, L.; Bandiello, E.; Hutter, E. M.; Sessolo, M.; Lederer, K.; Blochwitz-Nimoth, J.; Bolink, H. J. Efficient Vacuum Deposited p-i-n and n-i-p Perovskite Solar Cells Employing Doped Charge Transport Layers. *Energy Environ. Sci.* **2016**, *9*, 3456−3463.
(20) Forgács, D.; Gil-Escrig, L.; Pérez-Del-Rey, D.; Momblona, C.; Werner, J.; Niesen, B.; Ballif, C.; Sessolo, M.; Bolink, H. J. Efficient Monolithic Perovskite/Perovskite Tandem Solar Cells. *Adv. Energy Mater.* **2017**, *7*, 1602121.
(21) Malinkiewicz, O.; Yella, A.; Lee, Y. H.; Espallargas, G. M.; Graetzel, M.; Nazeeruddin, M. K.; Bolink, H. J. Perovskite Solar Cells Employing Organic Charge-Transport Layers. *Nat. Photonics* **2014**, *8*, 128−132.
(22) Sendner, M.; Nayak, P. K.; Egger, D. A.; Beck, S.; Muller, C.; Epding, B.; Kowalsky, W.; Kronik, L.; Snaith, H. J.; Pucci, A.; et al. Optical Phonons in Methylammonium Lead Halide Perovskites and Implications for Charge Transport. *Mater. Horiz.* **2016**, *3*, 613−620.
(23) Glaser, T.; Müller, C.; Sendner, M.; Krekeler, C.; Semonin, O. E.; Hull, T. D.; Yaffe, O.; Owen, J. S.; Kowalsky, W.; Pucci, A.; et al. Infrared Spectroscopic Study of Vibrational Modes in Methylammonium Lead Halide Perovskites. *J. Phys. Chem. Lett.* **2015**, *6*, 2913−2918.
(24) Saive, R.; Scherer, M.; Mueller, C.; Daume, D.; Schinke, J.; Kroeger, M.; Kowalsky, W. Imaging the Electric Potential within Organic Solar Cells. *Adv. Funct. Mater.* **2013**, *23*, 5854−5860.
(25) Saive, R.; Mueller, C.; Schinke, J.; Lovrincic, R.; Kowalsky, W. Understanding S-Shaped Current-Voltage Characteristics of Organic Solar Cells: Direct Measurement of Potential Distributions by Scanning Kelvin Probe. *Appl. Phys. Lett.* **2013**, *103*, 243303.
(26) Bergmann, V. W.; Weber, S. A. L.; Javier Ramos, F.; Nazeeruddin, M. K.; Grätzel, M.; Li, D.; Domanski, A. L.; Lieberwirth, I.; Ahmad, S.; Berger, R. Real-Space Observation of Unbalanced Charge Distribution inside a Perovskite-Sensitized Solar Cell. *Nat. Commun.* **2014**, *5*, 5001.
(27) Zerweck, U.; Loppacher, C.; Otto, T.; Grafström, S.; Eng, L. M. Accuracy and Resolution Limits of Kelvin Probe Force Microscopy. *Phys. Rev. B: Condens. Matter Mater. Phys.* **2005**, *71*, 125424.
(28) Chen, Q.; Zhou, H.; Song, T.-B.; Luo, S.; Hong, Z.; Duan, H.-S.; Dou, L.; Liu, Y.; Yang, Y. Controllable Self-Induced Passivation of Hybrid Lead Iodide Perovskites toward High Performance Solar Cells. *Nano Lett.* **2014**, *14*, 4158−4163.
(29) Würfel, U.; Cuevas, A.; Würfel, P. Charge Carrier Separation in Solar Cells. *IEEE J. Photovolt.* **2015**, *5*, 461−469.
(30) Etgar, L.; Gao, P.; Xue, Z.; Peng, Q.; Chandiran, A. K.; Liu, B.; Nazeeruddin, M. K.; Grätzel, M. Mesoscopic $CH_3NH_3PbI_3/TiO_2$ Heterojunction Solar Cells. *J. Am. Chem. Soc.* **2012**, *134*, 17396−17399.
(31) Laban, W. A.; Etgar, L. Depleted Hole Conductor-Free Lead Halide Iodide Heterojunction Solar Cells. *Energy Environ. Sci.* **2013**, *6*, 3249−3253.

DOI: 10.1021/acs.jpclett.8b00964
J. Phys. Chem. Lett. 2018, 9, 2770−2775

5 Efficient photo- and electroluminescence by trap states passivation in vacuum-deposited hybrid perovskite thin films

Hybrid halide perovskite LEDs have attracted much attention as they meet the requirements of inexpensive and energy efficient light source.[76–78] The low cost of the material and the possibility of simple and low temperature processing makes them a potential competitor to LEDs prepared from inorganic semiconductors which demand high temperature and complex manufacturing methods. Hybrid halide perovskite LEDs show a narrow emission line-width that is tunable over the visible spectrum, making them interesting for applications in consumer electronics such as flat-panel displays. The bandgap and thus the emission spectrum can be tuned exchanging the halides so that $MAPbX_3$ with $X=Cl^-$, $X=Br^-$, or $X=I^-$ shows bandgaps of 3.1 eV, 2.3 eV and 1.6 eV, respectively.[17] The bandgap can be further fine-tuned mixing the halides in different rations.[18,79] The Br^- and Cl^- based perovskites emit in the visible spectrum and show an increased exciton binding energy and are thus predominantly used for LEDs.[19] In contrast, the MAPI perovskite shows excellent properties as a photovoltaic absorber, with balanced hole and electron transport properties, high carrier mobility's and diffusion length and low exciton binding energies.[37,54,80–82] The low exciton binding energy of 9-60 meV [83,84] which is beneficial for photovoltaics might appear a drawback for applications in LEDs as high exciton binding energies increase the radiative biomolecular recombination. Furthermore, most MAPI perovskites show low photoluminescence quantum yields (PLQY) as the monomolecular trap-mediated recombination dominates under low fluences.[84,85] Hence, when MAPI is integrated into a diode device structure,

the obtained electroluminescence under forward driving is typically low. This is due to the rather low carrier density (in comparison to the trap density), which is unable to fill all the traps and hence these LEDs exhibited a low efficiency.[86] For this reason, several studies are directed towards the passivation of traps in perovskite devices. In perovskite solar cells, passivation usually refers to a either a chemical passivation where the amount of defect trap states is reduced or a physical passivation by isolating certain functional layers from the environment.[87] Physical passivation can be applied at any interface in the devices stack and is complementary to chemical passivation. Chemical passivation is specifically relevant for the grain boundaries in perovskite active layers as they show an increased trap density. It has been shown that grain boundaries can be passivated using non-stoichiometric precursor ratios in MAPI perovskites. Supasai et al. showed that the presence of excess of PbI_2 leads to improved carrier lifetime which is most likely due to reduced recombination at the grain boundaries.[88] Interestingly, in perovskite materials traps can be passivated with either an excess or a deficiency of PbI_2 (excess MAI). Son et al showed a self-assembly effect of MAI at perovskite grain boundaries.[89] The excess of MAI significantly increased device efficiencies and additionally decreased the hysteresis of the cells. It was postulated that the MAI excess is retained at the grain boundaries as it cannot be accommodate in the perovskite lattice. It was later found that MAI vapor post treatment has similar effects.[90,91] The MAI vapor is able to diffuse into the perovskite lattice and passivate the bulk defects in MAPI.[87]

Here we present a non-stoichiometric, easy-to-process 3D MAPI perovskite structure exhibiting an external quantum efficiency of electroluminescence as high as 1.92 %. The near infrared emitting LED (EL peak maximum at 769

nm) shows a very low turn-on voltage of 1.65 V. These results were obtained by modifying the MAI to PbI_2 ratios in the structure by adjusting the respective sublimation rates.

Experimental Section

Thin-film and device preparation: ITO-coated glass substrates were cleaned using soap, water and isopropanol in an ultrasonic bath, followed by UV-ozone treatment. The substrates were transferred into a vacuum chamber integrated into a nitrogen-filled glovebox (H_2O and O_2 < 0.1 ppm) and evacuated to a pressure lower then 10^{-6} mbar. Two QCM sensors are used to monitor the deposition rate of the individual sources and a third one close to the substrate holder monitors the total deposition rate. For the TaTm HTL we F_6-TCNNQ as the organic dopant whereas for the C_{60} ETL PhIm. For thickness calibration, we individually sublimed charge transport materials and their dopants. Comparing the thickness inferred from the QCM sensors and the measured film thickness gives a calibration factor. The evaporation rates of the co-sublimed materials were controlled by separate QCM sensors and adjusted to desired doping concentration with temperatures ranging from 135-160 ^oC for the dopants and approximately 250 ^oC for the pure charge transport molecules. In the co-deposition process the deposition rates for TaTm and C_{60} were kept constant at 0.8 Å/s while varying the deposition rates of the dopants to 0.06 Å/s for F_6-TCNNQ and 0.2 Å/s for PhIm. Pure TaTm and C_{60} layers were deposited at a rates of 0.5 Å/s. 40 nm thick n-doped electron-transport layer (C_{60}:PhIm) was deposited and capped with a 10 nm thick pure C_{60} film. After completing this deposition, the chamber was vented with dry N_2 in order to replace the crucibles with the ones containing the perovskite precursors, PbI_2 and MAI. The vacuum chamber was evacuated again to a pressure lower then 10^{-6} mbar before co-depositing the perovskite film. For production of the different perovskite layers the MAI deposition rate was kept constant at 0.8 Å/s while varying the deposition rate of PbI_2 between

0.8 Å/s (1:1), 0.25 Å/s (3:1) and 0.13 Å/s (6:1). The source temperature of the MAI was kept constant at 70 ^{o}C and that of the PbI_2 varied between 250 ^{o}C and 305 ^{o}C. The vacuum chamber was vented again after deposition of a 320 nm thick perovskite film and the crucibles were replaced with those containing F_6-TCNNQ and TaTm, and evacuated again to a pressure of 10^{-6} mbar. The devices were finished by deposition of 10 nm thick TaTm capped with 40 nm thick doped HTL (TaTm:F_6-TCNNQ). Finally the substrates were transferred to a second vacuum chamber where the gold top contact (100 nm thick) was deposited.

Thin-film characterization: X-ray diffraction was measured with a Panalytical Empyrean diffractometer equipped with CuKα anode operated at 45 kV and 30 mA and a Pixcel 1D detector in scanning line mode. Single scans were acquired in the 2 theta = 10° to 50° range in Bragg-Brentano geometry in air. Anti-scatter slits of 1/16° and step-sizes of 0.025° were used for high-resolution diffractograms. Data analysis was performed with HighScore Plus software. Scanning Electron Microscopy (SEM) images were collected on a Hitachi S-4800 microscope operating at an accelerating voltage of 2 kV over Platinum - metallized samples. Absorption spectra were collected using a fiber-optics based Avantes Avaspec 2048 spectrometer. The JV- and electroluminescence-voltage (LV) characteristics were collected using a Keithley Model 2400 source measurement unit and a calibrated Si-photodiode coupled to a Keithley Model 6485 pico-amperometer, respectively. Electroluminescence spectra were recorded using an Avantis fiber-optics spectrometer.

Time-resolved photoluminescence spectroscopy setup: For the time-resolved PL measurements, the excitation pulses were generated by the fundamental

near-UV pulses of a Q-switched Surelite Continuum Laser (3 ns, 355 nm, 10 Hz) and frequency converted in an Optical Parametrical Oscillator (GWU Versa scan). The intensity of the excitation pulses was varied by using different neutral optical density filters. An Andor i-Star camera, coupled to a monochromator, was used for the detection of the PL signal. The decay of the PL signal at different times after the excitation was recorded by varying the time-delay between the Qswitching of the laser and the detection time of the camera.

Results and discussion

The light emitting layer consisted of a 320 nm thick MAPI perovskite obtained by vapor phase co-deposition of PbI_2 and MAI which was sandwiched between a hole transporting (and electron blocking) and an electron transporting (and hole blocking) layer. The MAPI LEDs were produced optimizing the ratios of the precursors of MAI and PbI_2. In the co-evaporation process the ratios of these components were changed by changing the evaporation speed of PbI_2 while maintaining the speed of the MAI precursor at a fixed rate. These ratios were determined from the calibrated quartz crystal sensor reading during the evaporation process. Three different perovskite emitting layers were deposited with the MAI/PbI_2 speed ratios of 1:1, 3:1 and 6:1. The perovskite films were then exposed to air before the stack was finished.

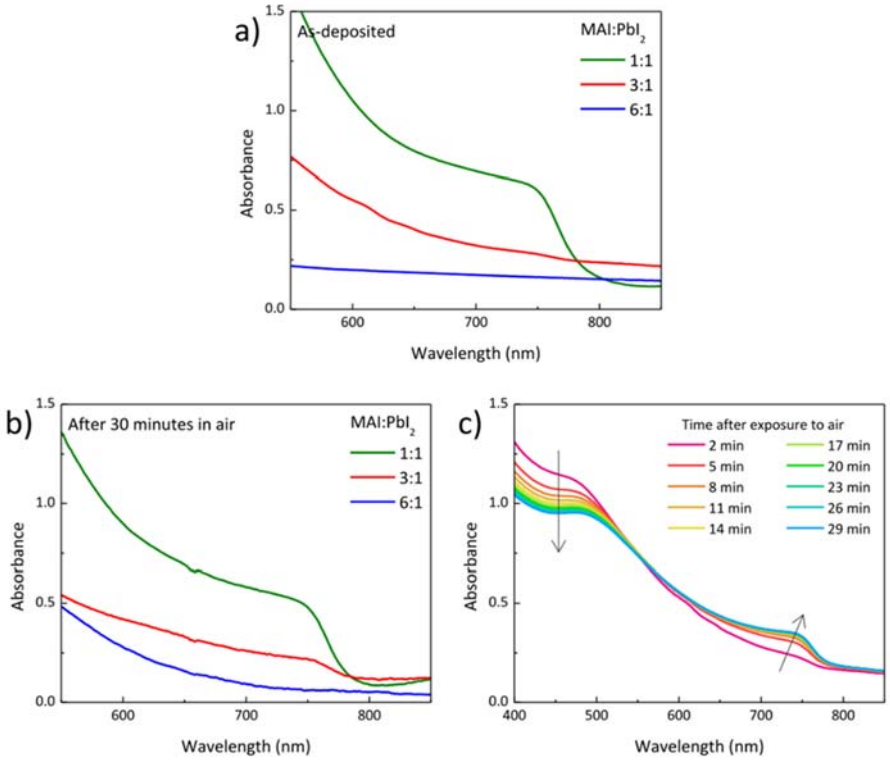

Figure 15. Absorption spectra of the perovskite films produced with different (MAI/Pbi2) ratios recorded a) in inert atmosphere immediately after deposition and b) after 30 minutes of exposure to air. c) Evolution of the absorption spectrum for the MAPI films with low MAI excess during air exposure.

Without exposure to air, only the stoichiometric perovskite shows clearly the characteristic features of the MAPI absorption spectrum with an onset at 780 nm (Figure 15a). The absorption spectra of the perovskite films produced with MAI excess only start to show the expected features after exposure to ambient atmosphere. A clear absorption onset at around 780 nm gradually forms and stable conditions are reached after approximately 30 minutes (Figure 15c). The effect of atmosphere on perovskite growth and stability was intensively studied in the last years. For instance, oxygen can intercalate into

the lattice framework of MAPI forming Pb-O bonds[92] but it is mainly the moisture of the ambient atmosphere that has a strong impact on methylammonium halide perovskite films. While a long exposure of perovskite films to ambient conditions usually leads to degradation and thus poorly performing devices, a controlled short exposure during different processing steps of the perovskite formation can be beneficial.[93] The formation of the perovskite structure during the exposure to ambient atmosphere can be understood looking at the chemistry of the perovskite precursors. Methylammonium halides are hygroscopic, favoring the penetration of water into the perovskite film. Water can partially dissolve the MA but not the Pb,[94,95] leading to a reorganization of the material and promoting its recrystallization.[96]

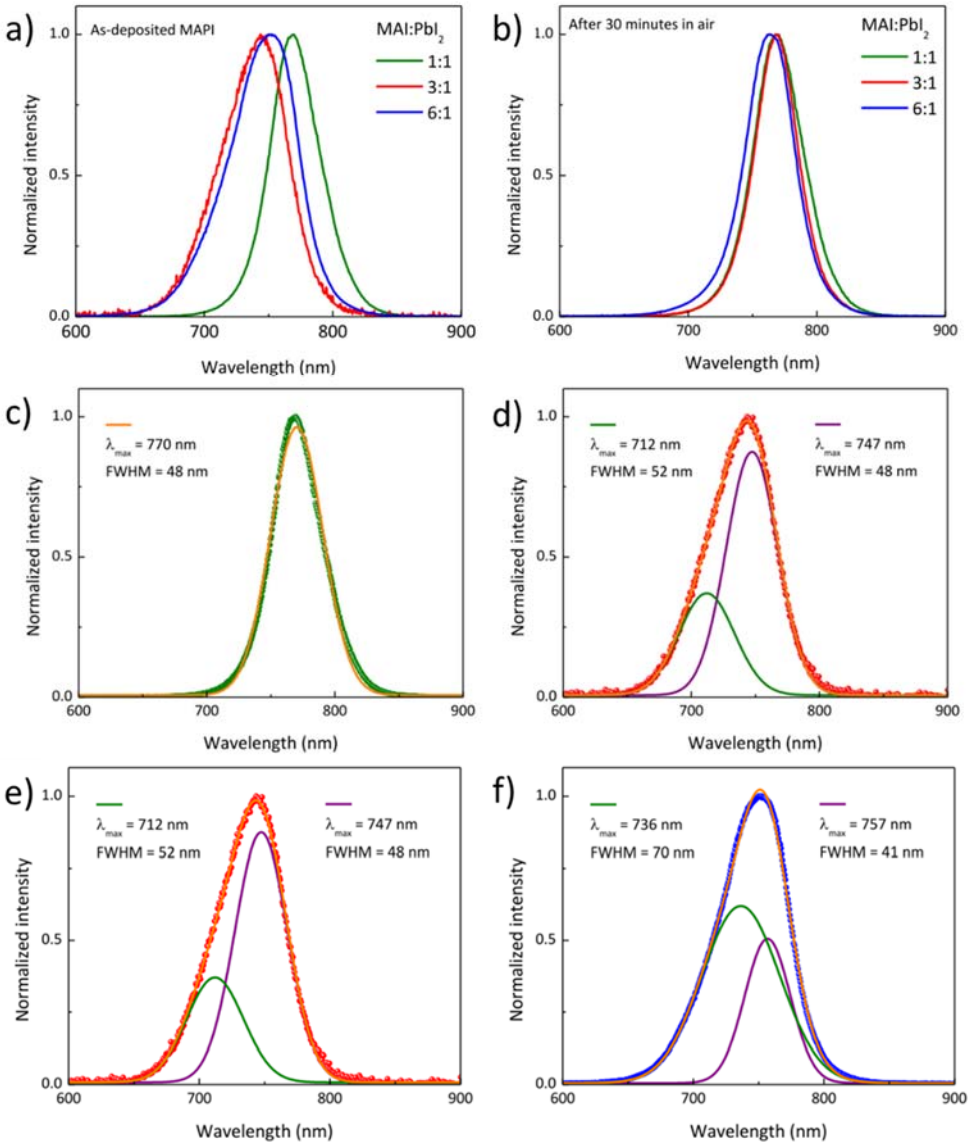

Figure 16. PL spectra recorded under excitation with a 515 nm continuous wave laser with an irradiance of 300 mW/cm^2 for a) as-deposited film in inert atmosphere and b) after 30 minutes of exposure to air. Fitting of the PL spectra with MAI:PbI_2 ratios of a) 1:1, b) 3:1 and c) 6:1 using c) one or d-e) two Gaussian functions. The raw data are represented as symbols and fittings as lines.

Figure 16a-b shows the PL spectra of the perovskite films produced with different precursor ratios before and after exposure to ambient atmosphere. The spectra of the unexposed films are unsymmetrical and can be fitted with either one (Figure 16c) or two Gaussian functions (Figure 16d-e). The blue shifted components of the non-stoichiometric films is likely associated with an increased disorder in the material.[97,98] This thesis is supported by the X-ray diffraction (XRD) (Figure 18). The high energy component disappears after exposure to air and a narrow PL-peak with a maximum intensity at 769 nm appears as it is expected for the band gap energy of MAPI, approximately 1.6 eV. Most importantly, the absolute PL signal increases after air exposure for the non-stoichiometric perovskite samples (Figure 17a). Figure 17b shows the PL dynamics of the three different MAPI films after exposure to air, monitored at the wavelength of their maximum intensity. The average lifetime was estimated using the following expression

$$\tau = \frac{\sum_i^{1,2} a_i \tau_i}{\sum_i^{1,2} a_i}$$

where i = 1 for the 1:1 compound and i = 2 for those with higher MAI content. The perovskite with 1:1 MAI:PbI_2 has a short PL lifetime of τ_1 = 5.7 ns, and the average lifetime for the 6:1 perovskite films is slightly longer, τ = 13.5 ns (τ_1 = 3.3 ns, τ_2 = 26 ns). Interestingly, the average lifetime substantially increases for the films that were produced with a MAI:PbI_2 ratio of 3:1, to τ = 34.4 ns (τ_1 = 13.7 ns, τ_2 = 47 ns), suggesting an increased PLQY.

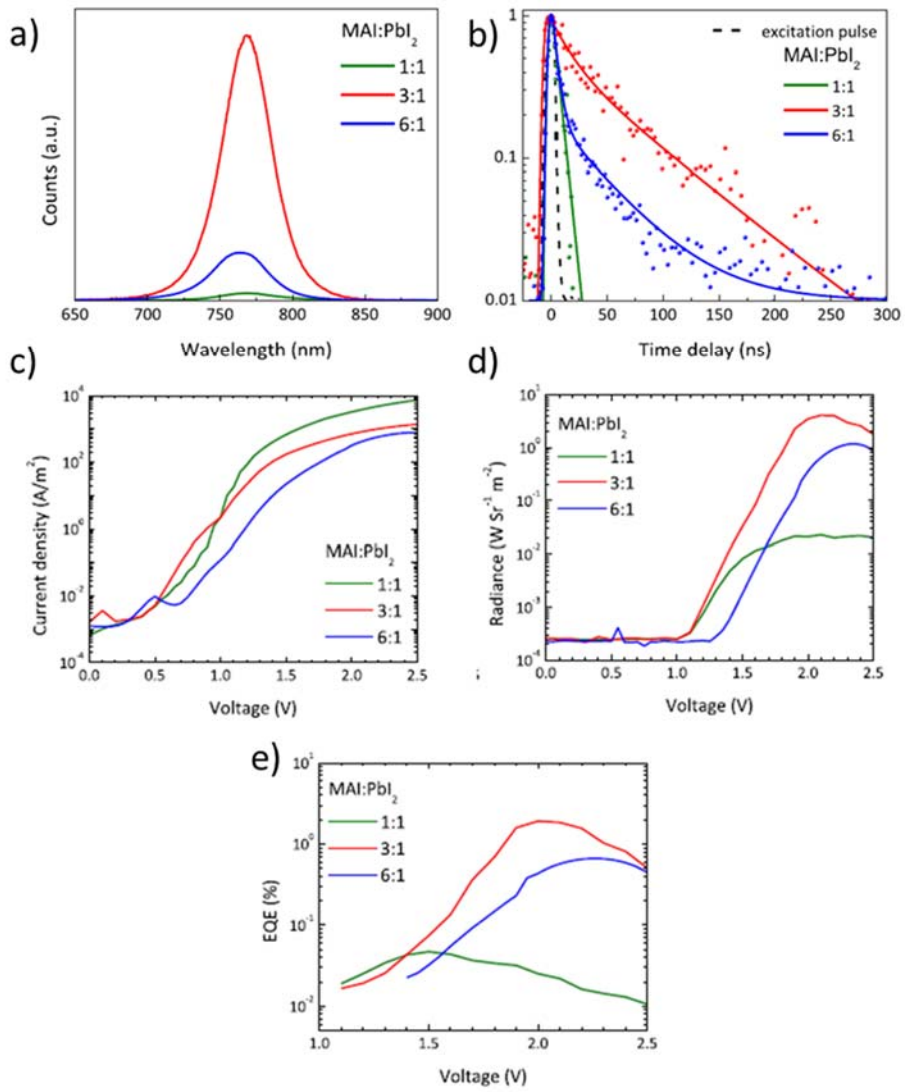

Figure 17. (a) PL spectra for perovskite films with different stoichiometry's recorded under excitation of a 515 nm continuous wave laser with an irradiance of 300 mW/cm^2. (b) PL dynamics of the three different MAPI films after exposure to air, monitored at the wavelength of their maximum intensity, each normalized to its maximum PL intensity. The films were excited at 520 nm with an excitation density of 5 × 1017 cm^{-3}. Optoelectronic characterization of MAPI LEDs with different MAI/PbI_2 ratios: (c) current density, (d) radiance, and (e) EQE vs applied voltage.

Figure 18 show the XRD patterns for the perovskite film series that was collected using Bragg-Brentano configuration in order to enhance the signal-to-noise ratio. The films were exposed to ambient atmosphere for 30 minutes as the layers that were used for photo- and electroluminescence studies. The XRD patterns show the characteristic tetragonal perovskite peaks at 14.02° and 28.25°, corresponding to the (100) and (200) reflections, for all film stoichiometries.

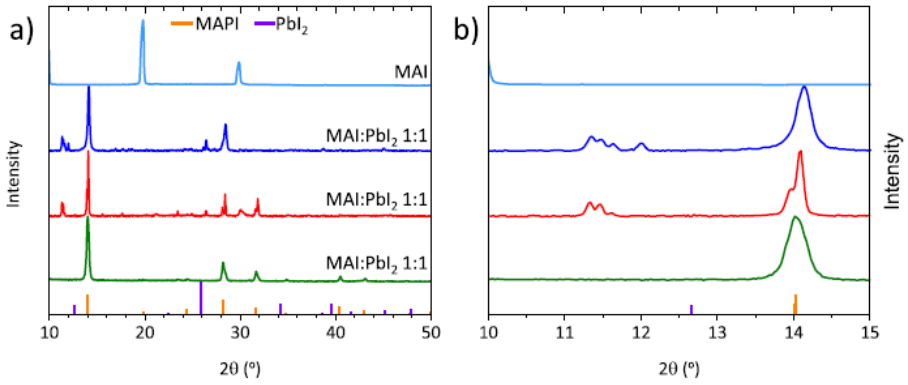

Figure 18. (a) XRD patterns of the three different perovskite films with increasing MAI content and for a pure vacuum-deposited MAI film. Reference patterns for MAPI and PbI_2 are also included (ICSD collection codes 250735 and 68819, respectively). (b) Zoom of the diffraction patterns in the 10° ≤ 2θ ≤ 15° range, highlighting the presence of structured reflections for excess-MAI perovskite films.

We noticed that when a large excess of MAI is used, the peak at 36.68° (corresponding to a combination of the (012) and (021) reflections) is missing, suggesting a different orientation of the material. Importantly, for excess MAI films, we identified weak diffraction signals at a low angle (11–12°). These structured reflections cannot directly be ascribed to MAI, as they are not observed for the pure MAI films deposited in our setup. However, they have been reported in the literature for MAPI films prepared from MAI-

excess precursors and were attributed to the formation of low-dimensional perovskite species.[99] The structural changes observed by XRD are reflected in the surface morphology of the films (Figure 19). In particular, only the stoichiometric MAPI shows a typical polycrystalline morphology, whereas the films with a MAI excess appear composed of large agglomerates without any well-defined grain structure.

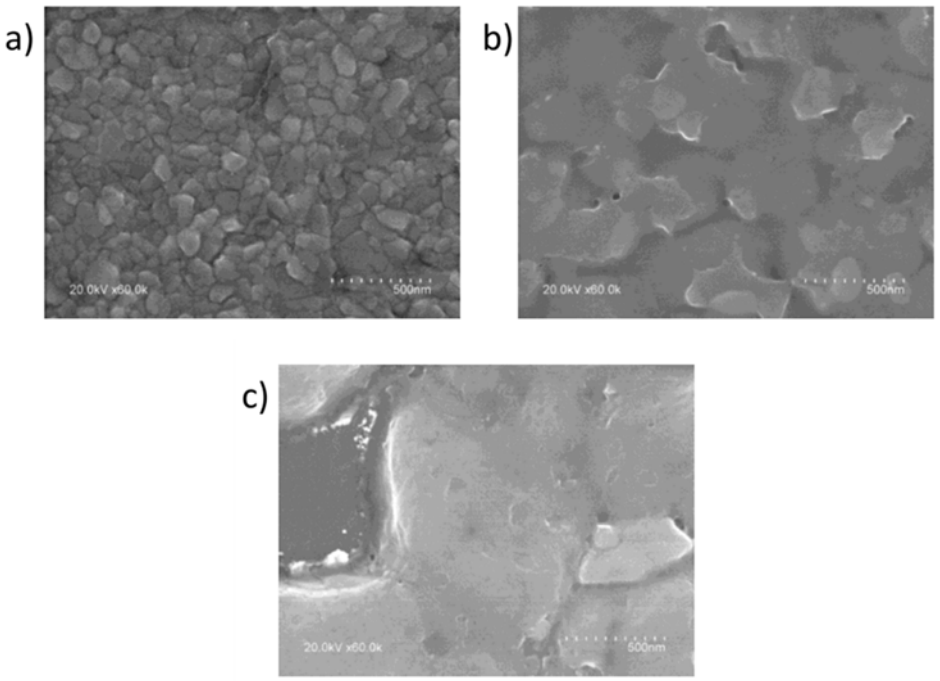

Figure 19. SEM images of perovskite films with different MAI/PbI_2 precursor ratios: a) stoichiometric, b) with low MAI excess and c) with high MAI excess. The series of MAPI films was used as a 320 nm thick emissive layer and

sandwiched between hole and electron injection layers. The electron injecting C_{60} layer consists of 10 nm thick intrinsic layer which is in contact with the perovskite and a 40 nm thick doped C_{60} to enhance the conductivity. TaTm was used as hole transport layer with a 10 nm thick intrinsic layer and a 40 nm thick doped layer. The entire stack was evaporated in a n-i-p

configuration with gold as a top reflective contact. The diodes were characterized applying a forward bias and the current density, the radiance and the EQE_{EL} were measured as a function of voltage (Figure 17c-e).

The current density starts rising at around 0.5V for all three devices and a significant radiance is detected at around 1.1 V for the 1:1 and 3:1 perovskites and at 1.2 V for the 6:1 perovskite. The LED employing the 3:1 perovskite shows the highest radiance of 4.1 $W \cdot sr^{-1} \cdot m^{-2}$, which is more than two orders of magnitude higher compared to the reference (1:1) device ($2.3 \cdot 10^{-2}$ $W \cdot sr^{-1} \cdot m^{-2}$). The brightest LED is also the most efficient, with an EQE of 1.92% which is higher compared to the reference (0.05%) based on the 1:1 material. Also, the LED with the largest MAI excess (6:1) showed an enhanced radiance (maximum at 1.2 $W \cdot sr^{-1} \cdot m^{-2}$) and EQE (0.67%) despite the lower current density flowing through the device. Most importantly, the EQE of the devices follow the trend of the PL-decay dynamics.

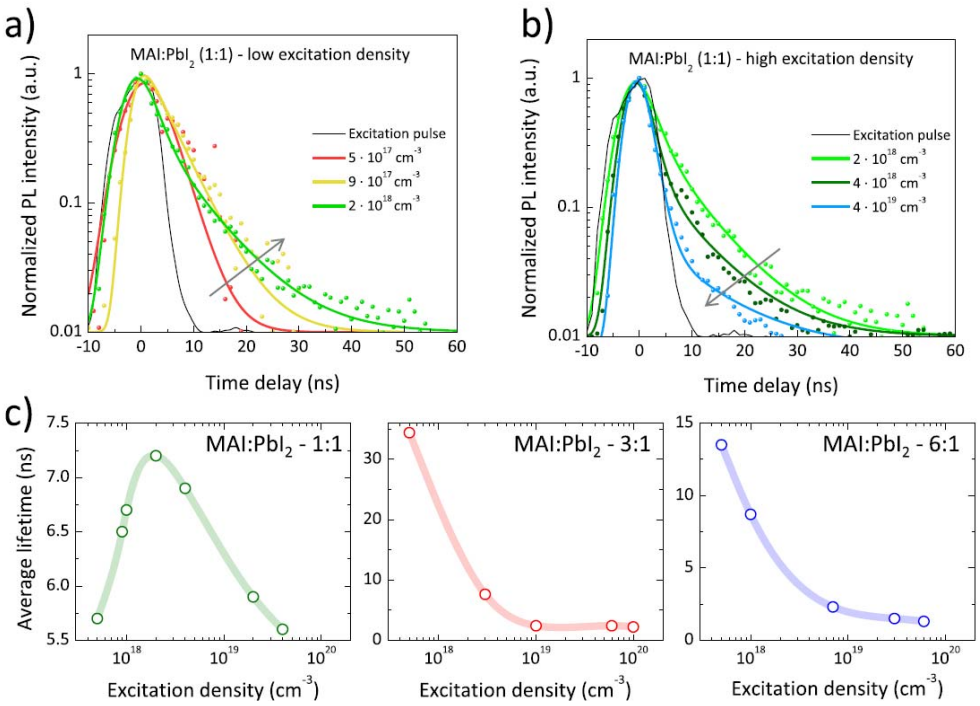

Figure 20. PL dynamics at (a) low and (b) high excitation densities for the MAPI film deposited with a MAI/PbI_2 ratio of 1:1. Symbols are experimental data and lines are fits using a biexponential function. (c) Trend of the average lifetime as a function of the excitation densities for materials with increasing MAI content. The samples were excited with 3 ns duration pulses at 520 nm, and the dynamics were recorded at the wavelength of the maximum intensity of each sample.

To get further insides into the optoelectronics of the samples, we studied their PL-dynamics as a function of excitation density (Figure 20). For the stoichiometric perovskite layer the PL-dynamics become slower up to a certain value. This behavior was reported before and attributed to trap filling.[100–102] When the carrier density is further increased, the dynamics become faster again due to higher order recombination processes.[103] The perovskite films with the MAI:PbI_2 precursor ratios of 3:1 and 6:1 behave somewhat different. The dynamics become faster with increasing carrier

density without any changes in the trend as it was observed for the stoichiometric perovskite film. This shows that traps are already filled at low carrier densities. To give a better overview of the dynamics, the average PL-lifetime was plotted as a function of carrier density (Figure 20c). The inversion point gives rise to the trap density in the stoichiometric film which is approximately 2×10^{18} cm^{-3}. The trap densities that were estimated here are large than the ones reported in the literature (10^{16} - $10^{17}cm^{-3}$).[27,53,83,104,105] These results are puzzling as the same perovskite shows outstanding performance when incorporated in a solar cell, with open circuit voltages exceeding 1.1 V.[53,106] Traps may be shallow so that under continuous illumination charge detrapping is an efficient process.

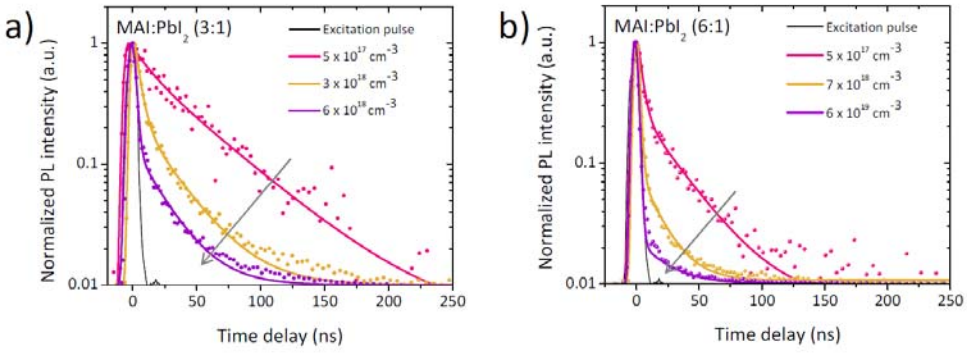

Figure 21. PL dynamics at increasing excitation densities for MAPI films with a) 3:1 and b) 6:1 MAI:PbI_2 ratios. Symbols are experimental data and lines the fitting using equation 1 in the main text. The samples were excited with 3 ns duration pulses at 520 nm, and the dynamics were recorded at the wavelength of the maximum intensity of each sample.

Nevertheless, the physical nature of trap states in perovskites remain unclear. It was proposed that they originate from halide vacancies on the surface or at grain boundaries.[107,108] Recently it was shown how light and atmospheric treatment increased the internal luminescence quantum efficiencies to 90%,[109] an analogous phenomenon to what was observed in our vacuum-deposited MAPI films. The authors proposed that as a result of O_2 reduction to O_2^- at surface vacancies occupied by trapped electrons, the sub-gap (trap) states shift down into the valence band, effectively removing the trap states. The same effect might be occurring here upon air exposure of the nonstoichiometric MAPI samples.

In summary the effect of excess MAI concentration in MAPI perovskites was studied. The precursor ratios were adapted during the co-evaporation process to control the stoichiometry. The PL-decay dynamics slowed down using excess of MAI in the film preparation suggesting that excess of MAI is able to passivate traps in the perovskites. Most importantly, these results agreed with the device performance where the most efficient device reached an EQE approaching 2%. The data presented here give further inside into the passivation of traps which is an important step towards the production of high efficient perovskite LEDs.

ACS APPLIED MATERIALS & INTERFACES

Research Article

Cite This: ACS Appl. Mater. Interfaces XXXX, XXX, XXX−XXX

www.acsami.org

Efficient Photo- and Electroluminescence by Trap States Passivation in Vacuum-Deposited Hybrid Perovskite Thin Films

Benedikt Dänekamp,[†] Nikolaos Droseros,[‡] Francisco Palazon,[†] Michele Sessolo,*[,†] Natalie Banerji,[‡] and Henk J. Bolink[†]

[†]Instituto de Ciencia Molecular, Universidad de Valencia, C/ Catedrático J. Beltrán 2, 46980 Paterna, Valencia, Spain

[‡]Department of Chemistry and Biochemistry, University of Bern, Freiestrasse 3, CH-3012 Bern, Switzerland

Supporting Information

ABSTRACT: Methylammonium lead iodide (MAPI) has excellent properties for photovoltaic applications, although it typically shows low photoluminescence quantum yield. Here, we report on vacuum-deposited MAPI perovskites obtained by modifying the methylammonium iodide (MAI) to PbI_2 ratio during vacuum deposition. By studying the excitation density dependence of the photoluminescence lifetime, a large concentration of trap states was deduced for the stoichiometric MAPI films. The use of excess MAI during vacuum processing is capable of passivating these traps, resulting in luminescent films which can be used to fabricate planar light-emitting diodes with quantum efficiency approaching 2%.

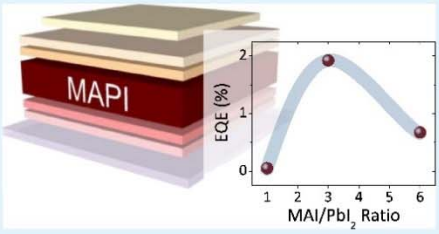

KEYWORDS: *perovskites, light-emitting diodes, vacuum deposition, passivation, stoichiometry*

INTRODUCTION

Hybrid lead halide perovskites are very interesting semiconductors for light-emitting diodes (LEDs), as they could meet the requirements to develop inexpensive and energy-efficient light sources.[1−3] The low cost of the precursors and the possibility of easy and low temperature processing make them potential competitors with LEDs prepared from inorganic crystalline semiconductors, as these require high temperature and complex manufacturing methods. Hybrid lead halide perovskite LEDs exhibit a narrow emission bandwidth easily tunable over the visible spectrum, leading to a high color purity. The type of halide employed in the perovskite has the strongest effect on the band gap, that is, methylammonium lead halide perovskites, $MAPbX_3$, with $X = Cl^-$, $X = Br^-$, or $X = I^-$ have band gaps of approximately 3.1, 2.3, and 1.6 eV, respectively.[4] The band gap can be further tuned by mixing the three halides in different ratios.[5,6] As the wide band gap perovskites containing Cl^- and Br^- emit in the visible range of the spectrum and show larger exciton binding energies, they have been predominantly investigated for LEDs.[7] On the other hand, $MAPbI_3$ has excellent properties for photovoltaic (PV) applications, such as the long carrier diffusion length, balanced hole and electron mobility, low trap density, and free carrier generation at room temperature.[8−12] The latter derives from a low exciton binding energy, reported to be within the 2−60 meV range,[13−15] which is beneficial for PVs. Furthermore, most $MAPbI_3$ perovskites show low photoluminescence quantum yield (PLQY) as the monomolecular trap-mediated recombination dominates at low excitation fluence.[10,16,17] This means that at a low current density, perovskite LEDs based on pure polycrystalline methylammonium lead iodide (MAPI) are rather inefficient. Strategies to overcome this limitation involve the use of quasi-2D perovskite structures to efficiently harvest charge carriers to the lowest-band gap emitting material, the use of nanostructured perovskite thin films or through passivating agents.[18−20] An alternative way to enhance the photoluminescence of perovskites is the use of an excess of methylammonium iodide, which has been shown to improve the photo- and electroluminescence as it leads to smoother, trap-free films when processed from solutions.[21−23] In solution-processed $MAPbBr_3$, a $MABr/PbBr_2$ molar ratio > 3 can lead to the formation of nanocrystals embedded in a MABr-rich matrix, which enhances the PLQY.[24] In MAPI films, an excess of methylammonium iodide (MAI) was found to cause brighter PL intensities and longer PL lifetimes both within the grains and at the grain boundaries, attributed to the passivation of the halide vacancies.[25] The initial reports on vacuum-deposited MAPI thin films also used an excess of MAI; however, an annealing step was used to promote the perovskite formation and the elimination of excess cation.[26] Hence, the effect of resilient MAI content in vacuum-deposited perovskite films, and its effect on the luminescent properties of the materials is unknown. Here, we report on vacuum-deposited MAPI perovskites obtained by modifying the MAI to PbI_2 ratio during vacuum deposition by adjusting the respective deposition rates without a post-deposition annealing step.

Received: August 1, 2018
Accepted: September 25, 2018
Published: September 25, 2018

DOI: 10.1021/acsami.8b13100
ACS Appl. Mater. Interfaces XXXX, XXX, XXX−XXX

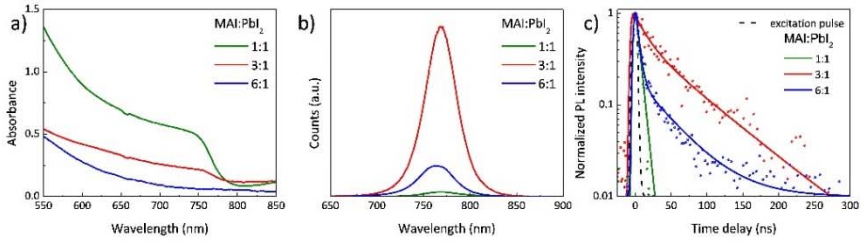

Figure 1. (a) Absorption spectra of the perovskite film series after exposure to air. (b) PL spectra for the same compounds recorded under excitation with a 515 nm continuous wave laser with an irradiance of 300 mW/cm^2. (c) PL dynamics with exponential fit of the three different MAPI films after exposure to air, monitored at the wavelength of their maximum intensity, each normalized to its maximum PL intensity. The films were excited at 520 nm with an excitation density of 5×10^{17} cm^{-3}.

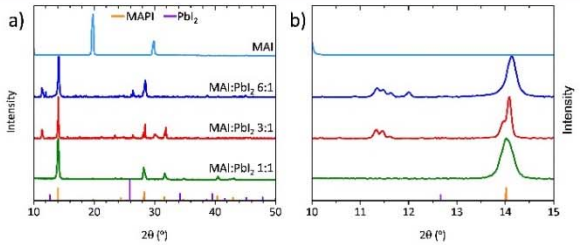

Figure 2. (a) XRD patterns of the three different perovskite films with increasing MAI content and for a pure vacuum-deposited MAI film. Reference patterns for MAPI and PbI_2 are also included (ICSD collection codes 250735 and 68819, respectively). (b) Zoom of the diffraction patterns in the $10° \leq 2\theta \leq 15°$ range, highlighting the presence of structured reflections for excess-MAI perovskite films.

These materials exhibit enhanced photoluminescent properties and, when incorporated into planar LEDs, lead to external quantum efficiency (EQE) approaching 2%.

The MAPI films were prepared by adjusting the ratio of the MAI and PbI_2 precursors. The ratios of these components were varied by modifying the deposition rate of PbI_2, while maintaining the MAI deposition rate fixed during the dual-source deposition process. These ratios were determined from the calibrated quartz crystal microbalance sensor readings during the deposition process. Three different perovskite emitting layers were deposited with the MAI/PbI_2 deposition rate ratios of 1:1, 3:1, and 6:1.

The as-deposited 1:1 MAPI films showed the characteristic optical absorption for this particular perovskite compound, with an onset at 780 nm and intense absorbance throughout the visible range (Figure 1a). On the other hand, the optical absorption spectra of the perovskite films produced with MAI excess show a much lower absorbance, with the band-to-band absorption essentially vanishing in the case of the 6:1 compound (Figure S2). Interestingly, upon exposure to air, the absorption spectrum of the 3:1 perovskite progressively evolves showing the clear band-to-band transition at about 780 nm and reaching stable optical characteristics after approximately 20 min (see Figures 1b and S2c). The effect of atmosphere on the perovskite growth and stability has been previously investigated. While a long exposure of perovskite films to ambient conditions usually leads to degradation and hence poorly performing devices, a controlled exposure during different processing steps can be beneficial.[27,28] Methylammonium halides are very hygroscopic, favoring the penetration of water into the perovskite film. Water preferentially hydrates/partially redissolves the organic cations, allowing a reorganization of the material and promoting its recrystallization.[29−31] This is most likely the mechanism responsible for the evolution of the absorption spectrum observed here, in view of the very high MAI content used in our films. Figure S3 shows the normalized photoluminescence spectrum of the perovskite film produced with 3:1 MAI/PbI_2 before and after exposure to air for 30 min. The spectrum of the unexposed film is unsymmetrical and can be deconvoluted using two Gaussian functions (Figure S4), one centered at 747 nm and the second, lower intensity component, at 712 nm. This blue-shifted component is likely associated with an increased disorder in the material[32,33] as also observed by X-ray diffraction (XRD) and scanning electron microscope (SEM) for perovskites with excess MAI. The high energy component eventually disappears after exposure to air, when a narrow PL signal with full width at half maximum of 40 nm and maximum intensity at 769 nm is observed. The latter corresponds to the expected band gap energy for MAPI thin films (about 1.6 eV). A similar evolution of the PL spectra was observed for the perovskite films with the 6:1 ratio. Importantly, the absolute PL intensity increases after air exposure for the sample with 3:1 MAI/PbI_2 ratio. The photoluminescence decay dynamics were recorded (Figure 1c) and analyzed either with a single exponential function for the case of the 1:1 perovskite or by a double exponential for the case of the samples with excess MAI. The average lifetime was estimated using the following expression

DOI: 10.1021/acsami.8b13100
ACS Appl. Mater. Interfaces XXXX, XXX, XXX−XXX

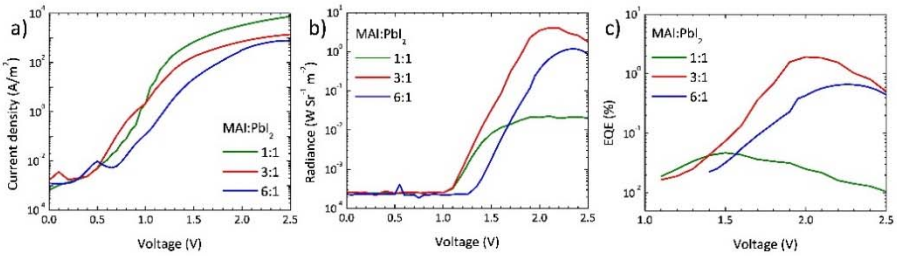

Figure 3. Optoelectronic characterization of MAPI LEDs with different MAI/PbI_2 ratios: (a) current density, (b) radiance, and (c) EQE vs applied voltage.

$$\tau = \frac{\sum_i^{1,2} a_i \tau_i}{\sum_i^{1,2} a_i} \quad (1)$$

where i = 1 for the 1:1 compound and i = 2 for those with higher MAI content. The perovskite with 3:1 MAI:PbI_2 has a short PL lifetime of τ_1 = 5.7 ns, and the average lifetime for the 6:1 perovskite films is slightly longer, τ = 13.5 ns (τ_1 = 3.3 ns, τ_2 = 26 ns). Interestingly, the average lifetime substantially increases for the films that were produced with a MAI:PbI_2 ratio of 3:1, to τ = 34.4 ns (τ_1 = 13.7 ns, τ_2 = 47 ns), thus contributing to their increased PLQY. The XRD (Figure 2) for the film series was collected using Bragg–Brentano configuration to enhance the signal-to-noise ratio. The perovskite films were exposed 30 min to ambient atmosphere before the measurements and hence are treated the same way as the layers used for photo- and electroluminescence studies.

The XRD patterns show the characteristic tetragonal perovskite peaks at 14.02° and 28.25°, corresponding to the (100) and (200) reflections, for all film stoichiometries. We noticed that when a large excess of MAI is used, the peak at 36.68° (corresponding to a combination of the (012) and (021) reflections) is missing, suggesting a different orientation of the material. Importantly, for excess MAI films, we identified weak diffraction signals at a low angle (11–12°). These structured reflections cannot directly be ascribed to MAI, as they are not observed for the pure MAI films deposited in our setup (Figure 1a,b). However, they have been reported in the literature for MAPI films prepared from MAI-excess precursors and were attributed to the formation of low-dimensional perovskite species.[34] The structural changes observed by XRD are reflected in the surface morphology of the films (Figure S1). In particular, only the stoichiometric MAPI shows a typical polycrystalline morphology, whereas the films with a MAI excess appear composed of large agglomerates without any well-defined grain structure.

The MAPI film series was used as the emissive layer in planar diodes with organic semiconductors as the charge transport materials. The emissive layer consisted of a 320 nm thick MAPI film exposed to air for 30 min, which was sandwiched in between a 10 nm thick hole transport (electron blocking) and electron transport (hole blocking) layers, referred to as HTL and ETL, respectively. The HTL consisted of a derivative of arylamine, *N*4,*N*4,*N*4″,*N*4″-tetra([1,1′-biphenyl]-4-yl)-[1,1:4′,1″-terphenyl]-4,4″-diamine (TaTm), whereas the fullerene C_{60} was used as the ETL. In between the electrodes and the intrinsic HTL and ETL, we deposited 40 nm thick films with the same materials but doped to enhance the conductivity and hence the carrier injection. For the TaTm, we used 2,20-(perfluoronaphthalene-2,6-diylidene)-dimalononitrile (F_6-TCNNQ) as the organic dopant, whereas for the C_{60} ETL, N^1,N^4-bis(tri-*p*-tolylphosphoranylidene)-benzene-1,4-diamine (PhIm) was used. The stack was fully evaporated in an n–i–p configuration on prepatterned indium tin oxide with gold as the reflective top contact. Detailed experimental conditions can be found in the Supporting Information. The diodes were characterized in forward bias, and the current density and radiance were measured as a function of the driving voltage (Figure 3a,b). The current density starts to rise above 0.5 V, and the current injection above 1 V is inversely proportional to the amount of MAI incorporated into the active layer. This might be expected considering the larger amount of excess material and reduced crystallinity in films with MAI excess, as also observed by XRD and SEM. The electroluminescence is detected at voltages as low as 1.1 V for the devices containing 1:1 and 3:1 perovskites, and at a slightly higher voltage (>1.3 V) for the 6:1 compound. Interestingly, the highest power output was recorded for the LEDs based on nonstoichiometric compounds, with the device employing the perovskite with a MAI/PbI_2 ratio of 3:1 reaching a maximum radiance of 4.1 W·sr^{-1}·m^{-2}, more than two orders of magnitude higher compared to the reference 1:1 device (2.3×10^{-2} W·sr^{-1}·m^{-2}). The associated EQE is 1.92% for the 3:1 MAI/PbI_2 compound as opposed to a maximum value of 0.05% for the LEDs based on 1:1 materials (Figure 3c). Also, the LED with the largest MAI excess (6:1) showed an enhanced radiance (maximum at 1.2 W·sr^{-1}·m^{-2}) and EQE (0.67%) despite the lower current density flowing through the device (Figure 3a). The EQE values recorded for the LED series follow the trend of the decay dynamics and PL intensities of the emissive layers, as described above. Interestingly, the electroluminescence spectra of the LEDs series (Figure S6) show a single emission peak analogous to the PL spectra recorded for the series of compound after exposure to air (Figure S3b). We found the stability of the perovskite LEDs to be rather poor, several minutes in the best working devices, as observed in several reports on these devices. The typical low lifetime of perovskite LEDs can be ascribed to the limited stability of perovskites, and to the instability induced by the particular device operation. Under the relatively high applied bias, several effects such as ionic migration,[35] diffusion of metallic species from electrodes,[36,37] and photoluminescence quenching[38] can take place. While perovskite solar cells are becoming more stable, thanks also to material and encapsulation development, their stability is expected to be higher as the current density in typical

DOI: 10.1021/acsami.8b13100
ACS Appl. Mater. Interfaces XXXX, XXX, XXX–XXX

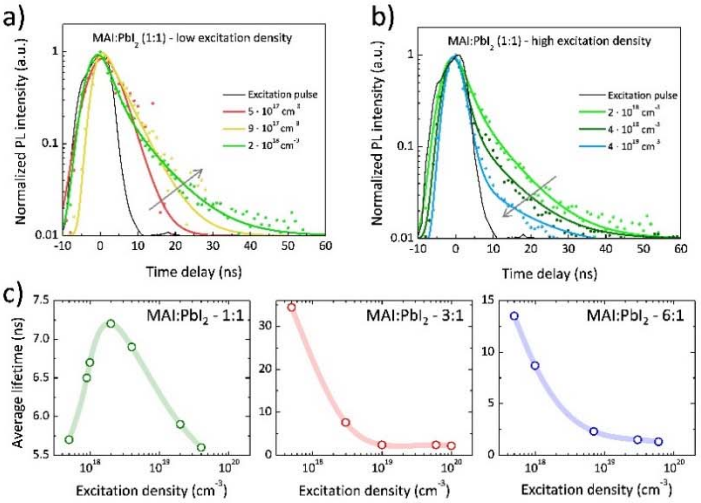

Figure 4. PL dynamics at (a) low and (b) high excitation densities for the MAPI film deposited with a MAI/PbI_2 ratio of 1:1. Symbols are experimental data and lines are fits using a biexponential function. (c) Trend of the average lifetime as a function of the excitation densities for materials with increasing MAI content. The samples were excited with 3 ns duration pulses at 520 nm, and the dynamics were recorded at the wavelength of the maximum intensity of each sample.

perovskite solar cells is lower than that in perovskite LEDs. In the latter, thermal stress because of Joule heating can accelerate the emitting layer degradation, especially for methylammonium-based perovskites.[39] These limitations are, however, not fully understood and still under investigation.

To shed light on the improved optical and optoelectronic properties of the samples with excess MAI, we studied their PL dynamics as a function of the excitation density (Figure 4). For the 1:1 perovskite, as clearly observed in Figure 4a, the PL dynamics become slower as the excitation density increases up to a certain value. This behavior has been observed in previous studies and it has been attributed to trap filling.[40−42] By further increasing the excitation density, the PL dynamics become faster (Figure 4b) because of higher order recombination processes.[43] On the other hand, as shown in Figure S5, the PL dynamics of the MAPI films with MAI/PbI_2 ratio of 3:1 and 6:1 exhibit a different trend compared to the stoichiometric perovskite. Their PL dynamics become faster when increasing the excitation density, without any change in the trend as observed for the stoichiometric material. To better visualize the PL dynamics, the average PL lifetime is plotted as a function of the excitation density (Figure 4c) for the series of materials studied here. For the reference 1:1 MAPI, the excitation density at which the inversion in the behavior of the dynamics occurs (maximum of the graph in Figure 4c) provides an estimation of the trap density of the material. This value is approximately 2×10^{18} cm^{-3} and is substantially larger compared to previous literature reports, where trap density in between 10^{16} and 10^{17} cm^{-3} were observed.[12,44−46] The large trap density hence explains the low PLQY and, in particular, the poor EQE of the corresponding LEDs. The effect of these trap states remains puzzling as the same 1:1 MAPI films do lead to very efficient solar cells (power conversion efficiency above 18%), with photovoltage exceeding 1.1 V.[47,48] Hence, traps may in fact be shallow such that under continued illumination, carrier detrapping is an efficient process.[49] The physical nature of trap states in perovskite materials remains unclear, but they likely originate from halide vacancies on the perovskite surface/grain boundaries.[50,51] Recently, it was shown that by combining light and atmospheric treatments, it is possible to increase the internal luminescence quantum efficiencies of perovskite films from 1 to 90%,[52] a phenomenon analogous to what was observed in our vacuum-deposited MAPI films. The authors proposed that as a result of O_2 reduction to O_2^- at surface vacancies occupied by trapped electrons, the sub-gap (trap) states shift down into the valence band, effectively removing the trap states. The same effect might be occurring here upon air exposure of the non-stoichiometric MAPI samples.

Other processes might contribute to alter the perovskite (surface) chemistry during MAPI deposition at high MAI rate. Recent studies have highlighted the possibility of decomposition of MAI into compounds other than its precursors, methylamine and hydroiodic acid.[53,54] The molecular salt MAI might decompose into energetically favored thermal degradation products, such as iodomethane and ammonia. Interestingly, iodomethane had been shown to passivate the perovskite surface, increasing the grain size, whereas reducing the trap density.[55] However, further insight on the exact structural and chemical effects are necessary to rationalize these findings.[56] On the other hand, both the films with MAI excess show a continuous decrease of the PL lifetime, indicating that traps are already filled in this excitation regime. Hence, the excess MAI efficiently passivates traps, reducing their concentration in comparison with the 1:1 MAPI. Importantly, the longest PL lifetime and reduced trap concentration agree with the trend observed in the EQE of the devices.

DOI: 10.1021/acsami.8b13100
ACS Appl. Mater. Interfaces XXXX, XXX, XXX−XXX

CONCLUSION

In summary, the effect of excess MAI in the preparation of vacuum-deposited MAPI thin films was studied. The stoichiometry was controlled by the relative deposition rates of PbI_2 and MAI during the vacuum deposition process. We observed substantial differences in the perovskite films, with the PL intensity proportional to the MAI content. By studying the excitation density dependence of the photoluminescence lifetime, a large concentration of trap states was deduced for the stoichiometric MAPI films, which appears to be responsible for their low luminescence. The use of excess MAI in evaporated films is capable of efficiently passivating these traps, in analogy to what was observed for solution-processed MAPI films. Importantly, we were able to prepare planar light-emitting diodes (LEDs) with EQE approaching 2% by using MAPI films with intentionally altered stoichiometry. This value is almost two orders of magnitude higher compared to the reference LEDs employing the stoichiometric MAPI. The data presented here are promising for the development of efficient, vacuum-deposited perovskite LEDs, where trap management is essential to guarantee an efficient electroluminescence.

ASSOCIATED CONTENT

Supporting Information

The Supporting Information is available free of charge on the ACS Publications website at DOI: 10.1021/acsami.8b13100.

SEM images, optical absorption, PL spectra, PL decay kinetics, and EL spectra for the samples discussed in the manuscript. Full experimental section (PDF)

AUTHOR INFORMATION

Corresponding Author

*E-mail: michele.sessolo@uv.es.

ORCID

Nikolaos Droseros: 0000-0002-9818-9387
Francisco Palazon: 0000-0002-1503-5965
Michele Sessolo: 0000-0002-9189-3005
Natalie Banerji: 0000-0001-9181-2642
Henk J. Bolink: 0000-0001-9784-6253

Notes

The authors declare no competing financial interest.

ACKNOWLEDGMENTS

We acknowledge financial support from the European Union H2020 project INFORM (grant 675867). F.P. acknowledges the European Union for his Marie Sklodowska-Curie Grant (PerovSAMs—747599). N.D. and N.B. would like to acknowledge the Universities of Fribourg and Bern, Switzerland, for providing funding and infrastructure. Financial support is acknowledged from the Spanish Ministry of Economy and Competitiveness (MINECO) via the Unidad de Excelencia Maria de Maeztu MDM-2015-0538, MAT2017-88821-R, PCIN-2015-255, PCIN-2017-014 and the Generalitat Valenciana (Prometeo/2016/135). M.S. thanks the MINECO for his RyC contract.

REFERENCES

(1) Sutherland, B. R.; Sargent, E. H. Perovskite Photonic Sources. *Nat. Photon.* **2016**, *10*, 295−302.

(2) Kim, Y.-H.; Cho, H.; Lee, T.-W. Metal Halide Perovskite Light Emitters. *Proc. Natl. Acad. Sci. U.S.A.* **2016**, *113*, 11694−11702.

(3) Veldhuis, S. A.; Boix, P. P.; Yantara, N.; Li, M.; Sum, T. C.; Mathews, N.; Mhaisalkar, S. G. Perovskite Materials for Light-Emitting Diodes and Lasers. *Adv. Mater.* **2016**, *28*, 6804−6834.

(4) Kitazawa, N.; Watanabe, Y.; Nakamura, Y. Optical Properties of $CH_3NH_3PbX_3$ (X = Halogen) and Their Mixed-Halide Crystals. *J. Mater. Sci.* **2002**, *37*, 3585−3587.

(5) Noh, J. H.; Im, S. H.; Heo, J. H.; Mandal, T. N.; Seok, S. I. Chemical Management for Colorful, Efficient, and Stable Inorganic−Organic Hybrid Nanostructured Solar Cells. *Nano Lett.* **2013**, *13*, 1764−1769.

(6) Comin, R.; Walters, G.; Thibau, E. S.; Voznyy, O.; Lu, Z.-H.; Sargent, E. H. Structural, Optical, and Electronic Studies of Wide-Bandgap Lead Halide Perovskites. *J. Mater. Chem. C* **2015**, *3*, 8839−8843.

(7) Sessolo, M.; Gil-Escrig, L.; Longo, G.; Bolink, H. J. Perovskite Luminescent Materials. *Top. Curr. Chem.* **2016**, *374*, 52.

(8) Chondroudis, K.; Mitzi, D. B. Electroluminescence from an Organic−Inorganic Perovskite Incorporating a Quaterthiophene Dye within Lead Halide Perovskite Layers. *Chem. Mater.* **1999**, *11*, 3028−3030.

(9) Xing, G.; Mathews, N.; Sun, S.; Lim, S. S.; Lam, Y. M.; Gratzel, M.; Mhaisalkar, S.; Sum, T. C. Long-Range Balanced Electron- and Hole-Transport Lengths in Organic-Inorganic $CH_3NH_3PbI_3$. *Science* **2013**, *342*, 344−347.

(10) Stranks, S. D.; Burlakov, V. M.; Leijtens, T.; Ball, J. M.; Goriely, A.; Snaith, H. J. Recombination Kinetics in Organic-Inorganic Perovskites: Excitons, Free Charge, and Subgap States. *Phys. Rev. Appl.* **2014**, *2*, 034007.

(11) Wehrenfennig, C.; Eperon, G. E.; Johnston, M. B.; Snaith, H. J.; Herz, L. M. High Charge Carrier Mobilities and Lifetimes in Organolead Trihalide Perovskites. *Adv. Mater.* **2014**, *26*, 1584−1589.

(12) Xing, G.; Mathews, N.; Lim, S. S.; Yantara, N.; Liu, X.; Sabba, D.; Grätzel, M.; Mhaisalkar, S.; Sum, T. C. Low-Temperature Solution-Processed Wavelength-Tunable Perovskites for Lasing. *Nat. Mater.* **2014**, *13*, 476−480.

(13) Lin, Q.; Armin, A.; Nagiri, R. C. R.; Burn, P. L.; Meredith, P. Electro-Optics of Perovskite Solar Cells. *Nat. Photon.* **2014**, *9*, 106−112.

(14) Savenije, T. J.; Ponseca, C. S.; Kunneman, L.; Abdellah, M.; Zheng, K.; Tian, Y.; Zhu, Q.; Canton, S. E.; Scheblykin, I. G.; Pullerits, T.; Yartsev, A.; Sundström, V. Thermally Activated Exciton Dissociation and Recombination Control the Carrier Dynamics in Organometal Halide Perovskite. *J. Phys. Chem. Lett.* **2014**, *5*, 2189−2194.

(15) Yang, Y.; Yang, M.; Li, Z.; Crisp, R.; Zhu, K.; Beard, M. C. Comparison of Recombination Dynamics in $CH_3NH_3PbBr_3$ and $CH_3NH_3PbI_3$ Perovskite Films: Influence of Exciton Binding Energy. *J. Phys. Chem. Lett.* **2015**, *6*, 4688−4692.

(16) Deschler, F.; Price, M.; Pathak, S.; Klintberg, L. E.; Jarausch, D.-D.; Higler, R.; Hüttner, S.; Leijtens, T.; Stranks, S. D.; Snaith, H. J.; Atatüre, M.; Phillips, R. T.; Friend, R. H. High Photoluminescence Efficiency and Optically Pumped Lasing in Solution-Processed Mixed Halide Perovskite Semiconductors. *J. Phys. Chem. Lett.* **2014**, *5*, 1421−1426.

(17) Wu, X.; Trinh, M. T.; Niesner, D.; Zhu, H.; Norman, Z.; Owen, J. S.; Yaffe, O.; Kudisch, B. J.; Zhu, X.-Y. Trap States in Lead Iodide Perovskites. *J. Am. Chem. Soc.* **2015**, *137*, 2089−2096.

(18) Cho, H.; Jeong, S.-H.; Park, M.-H.; Kim, Y.-H.; Wolf, C.; Lee, C.-L.; Heo, J. H.; Sadhanala, A.; Myoung, N.; Yoo, S.; Im, S. H.; Friend, R. H.; Lee, T.-W. Overcoming the Electroluminescence Efficiency Limitations of Perovskite Light-Emitting Diodes. *Science* **2015**, *350*, 1222−1225.

(19) Yuan, M.; Quan, L. N.; Comin, R.; Walters, G.; Sabatini, R.; Voznyy, O.; Hoogland, S.; Zhao, Y.; Beauregard, E. M.; Kanjanaboos, P.; Lu, Z.; Kim, D. H.; Sargent, E. H. Perovskite Energy Funnels for Efficient Light-Emitting Diodes. *Nat. Nanotechnol.* **2016**, *11*, 872−877.

DOI: 10.1021/acsami.8b13100
ACS Appl. Mater. Interfaces XXXX, XXX, XXX−XXX

(20) Tian, Y.; Zhou, C.; Worku, M.; Wang, X.; Ling, Y.; Gao, H.; Zhou, Y.; Miao, Y.; Guan, J.; Ma, B. Highly Efficient Spectrally Stable Red Perovskites Light-Emitting Diodes. *Adv. Mater.* **2018**, *30*, 1707093.
(21) Wang, J.; Wang, N.; Jin, Y.; Si, J.; Tan, Z.-K.; Du, H.; Cheng, L.; Dai, X.; Bai, S.; He, H.; Ye, Z.; Lai, M. L.; Friend, R. H.; Huang, W. Interfacial Control Toward Efficient and Low-Voltage Perovskite Light-Emitting Diodes. *Adv. Mater.* **2015**, *27*, 2311−2316.
(22) Sadhanala, A.; Ahmad, S.; Zhao, B.; Giesbrecht, N.; Pearce, P. M.; Deschler, F.; Hoye, R. L. Z.; Gödel, K. C.; Bein, T.; Docampo, P.; Dutton, S. E.; De Volder, M. F. L.; Friend, R. H. Blue-Green Color Tunable Solution Processable Organolead Chloride−Bromide Mixed Halide Perovskites for Optoelectronic Applications. *Nano Lett.* **2015**, *15*, 6095−6101.
(23) Ham, S.; Choi, Y. J.; Lee, J.-W.; Park, N.-G.; Kim, D. Impact of Excess CH_3NH_3I on Free Carrier Dynamics in High-Performance Nonstoichiometric Perovskites. *J. Phys. Chem. C* **2017**, *121*, 3143−3148.
(24) Lee, J.-W.; Choi, Y. J.; Yang, J.-M.; Ham, S.; Jeon, S. K.; Lee, J. Y.; Song, Y.-H.; Ji, E. K.; Yoon, D.-H.; Seo, S.; Shin, H.; Han, G. S.; Jung, H. S.; Kim, D.; Park, N.-G. In-Situ Formed Type I Nanocrystalline Perovskite Film for Highly Efficient Light-Emitting Diode. *ACS Nano* **2017**, *11*, 3311−3319.
(25) Ham, S.; Choi, Y. J.; Lee, J.-W.; Park, N.-G.; Kim, D. Impact of Excess CH_3NH_3I on Free Carrier Dynamics in High-Performance Nonstoichiometric Perovskites. *J. Phys. Chem. C* **2017**, *121*, 3143−3148.
(26) Liu, M.; Johnston, M. B.; Snaith, H. J. Efficient Planar Heterojunction Perovskite Solar Cells by Vapour Deposition. *Nature* **2013**, *501*, 395−398.
(27) Eperon, G. E.; Habisreutinger, S. N.; Leijtens, T.; Bruijnaers, B. J.; van Franeker, J. J.; deQuilettes, D. W.; Pathak, S.; Sutton, R. J.; Grancini, G.; Ginger, D. S.; Janssen, R. A. J.; Petrozza, A.; Snaith, H. J. The Importance of Moisture in Hybrid Lead Halide Perovskite Thin Film Fabrication. *ACS Nano* **2015**, *9*, 9380−9393.
(28) Brenes, R.; Guo, D.; Osherov, A.; Noel, N. K.; Eames, C.; Hutter, E. M.; Pathak, S. K.; Niroui, F.; Friend, R. H.; Islam, M. S.; Snaith, H. J.; Bulović, V.; Savenije, T. J.; Stranks, S. D. Metal Halide Perovskite Polycrystalline Films Exhibiting Properties of Single Crystals. *Joule* **2007**, *1*, 155−167.
(29) Dong, X.; Fang, X.; Lv, M.; Lin, B.; Zhang, S.; Ding, J.; Yuan, N. Improvement of the Humidity Stability of Organic−Inorganic Perovskite Solar Cells Using Ultrathin Al_2O_3 Layers Prepared by Atomic Layer Deposition. *J. Mater. Chem. A* **2015**, *3*, 5360−5367.
(30) Niu, G.; Li, W.; Meng, F.; Wang, L.; Dong, H.; Qiu, Y. Study on the Stability of $CH_3NH_3PbI_3$ Films and the Effect of Post-Modification by Aluminum Oxide in All-Solid-State Hybrid Solar Cells. *J. Mater. Chem. A* **2014**, *2*, 705−710.
(31) Bass, K. K.; McAnally, R. E.; Zhou, S.; Djurovich, P. I.; Thompson, M. E.; Melot, B. C. Influence of Moisture on the Preparation, Crystal Structure, and Photophysical Properties of Organohalide Perovskites. *Chem. Commun.* **2014**, *50*, 15819−15822.
(32) Park, B.-w.; Jain, S. M.; Zhang, X.; Hagfeldt, A.; Boschloo, G.; Edvinsson, T. Resonance Raman and Excitation Energy Dependent Charge Transfer Mechanism in Halide-Substituted Hybrid Perovskite Solar Cells. *ACS Nano* **2015**, *9*, 2088−2101.
(33) Mamun, A. A.; Ava, T. T.; Jeong, H. J.; Jeong, M. S.; Namkoong, G. A Deconvoluted PL Approach to Probe the Charge Carrier Dynamics of the Grain Interior and Grain Boundary of a Perovskite Film for Perovskite Solar Cell Applications. *Phys. Chem. Chem. Phys.* **2017**, *19*, 9143−9148.
(34) Song, Z.; Watthage, S. C.; Phillips, A. B.; Tompkins, B. L.; Ellingson, R. J.; Heben, M. J. Impact of Processing Temperature and Composition on the Formation of Methylammonium Lead Iodide Perovskites. *Chem. Mater.* **2015**, *27*, 4612−4619.
(35) Li, C.; Guerrero, A.; Zhong, Y.; Gräser, A.; Luna, C. A. M.; Köhler, J.; Bisquert, J.; Hildner, R.; Huettner, S. Real-Time Observation of Iodide Ion Migration in Methylammonium Lead Halide Perovskites. *Small* **2017**, *13*, 1701711.
(36) Domanski, K.; Correa-Baena, J.-P.; Mine, N.; Nazeeruddin, M. K.; Abate, A.; Saliba, M.; Tress, W.; Hagfeldt, A.; Grätzel, M. Not All That Glitters Is Gold: Metal-Migration-Induced Degradation in Perovskite Solar Cells. *ACS Nano* **2016**, *10*, 6306−6314.
(37) Seo, H.-K.; Kim, H.; Lee, J.; Park, M.-H.; Jeong, S.-H.; Kim, Y.-H.; Kwon, S.-J.; Han, T.-H.; Yoo, S.; Lee, T.-W. Efficient Flexible Organic/Inorganic Hybrid Perovskite Light-Emitting Diodes Based on Graphene Anode. *Adv. Mater.* **2017**, *29*, 1605587.
(38) Chen, S.; Wen, X.; Sheng, R.; Huang, S.; Deng, X.; Green, M. A.; Ho-Baillie, A. Mobile Ion Induced Slow Carrier Dynamics in Organic−Inorganic Perovskite $CH_3NH_3PbBr_3$. *ACS Appl. Mater. Interfaces* **2016**, *8*, 5351−5357.
(39) Cho, H.; Kim, Y.-H.; Wolf, C.; Lee, H.-D.; Lee, T.-W. Improving the Stability of Metal Halide Perovskite Materials and Light-Emitting Diodes. *Adv. Mater.* **2018**, 1704587.
(40) Yamada, Y.; Yamada, T.; Shimazaki, A.; Wakamiya, A.; Kanemitsu, Y. Interfacial Charge-Carrier Trapping in $CH_3NH_3PbI_3$-Based Heterolayered Structures Revealed by Time-Resolved Photoluminescence Spectroscopy. *J. Phys. Chem. Lett.* **2016**, *7*, 1972−1977.
(41) Phuong, L. Q.; Braly, I. L.; Katahara, J. K.; Hillhouse, H. W.; Kanemitsu, Y. Nonlinear photocarrier recombination dynamics in mixed-halide $CH_3NH_3Pb(I_{1-x}Br_x)_3$ perovskite thin films. *Appl. Phys. Express* **2017**, *10*, 102401.
(42) Handa, T.; Tex, D. M.; Shimazaki, A.; Wakamiya, A.; Kanemitsu, Y. Charge Injection Mechanism at Heterointerfaces in $CH_3NH_3PbI_3$ Perovskite Solar Cells Revealed by Simultaneous Time-Resolved Photoluminescence and Photocurrent Measurements. *J. Phys. Chem. Lett.* **2017**, *8*, 954−960.
(43) Saba, M.; Cadelano, M.; Marongiu, D.; Chen, F.; Sarritzu, V.; Sestu, N.; Figus, C.; Aresti, M.; Piras, R.; Lehmann, A. G.; Cannas, C.; Musinu, A.; Quochi, F.; Mura, A.; Bongiovanni, G. Correlated Electron−Hole Plasma in Organometal Perovskites. *Nat. Commun.* **2014**, *5*, 5049.
(44) Manser, J. S.; Kamat, P. V. Band Filling with Free Charge Carriers in Organometal Halide Perovskites. *Nat. Photon.* **2014**, *8*, 737−743.
(45) Draguta, S.; Thakur, S.; Morozov, Y. V.; Wang, Y.; Manser, J. S.; Kamat, P. V.; Kuno, M. Spatially Non-uniform Trap State Densities in Solution-Processed Hybrid Perovskite Thin Films. *J. Phys. Chem. Lett.* **2016**, *7*, 715−721.
(46) de Quilettes, D. W.; Vorpahl, S. M.; Stranks, S. D.; Nagaoka, H.; Eperon, G. E.; Ziffer, M. E.; Snaith, H. J.; Ginger, D. S. Impact of Microstructure on Local Carrier Lifetime in Perovskite Solar Cells. *Science* **2015**, *348*, 683−686.
(47) Momblona, C.; Gil-Escrig, L.; Bandiello, E.; Hutter, E. M.; Sessolo, M.; Lederer, K.; Blochwitz-Nimoth, J.; Bolink, H. J. Efficient Vacuum Deposited p-i-n and n-i-p Perovskite Solar Cells Employing Doped Charge Transport Layers. *Energy Environ. Sci.* **2016**, *9*, 3456−3463.
(48) Pérez-del-Rey, D.; Boix, P. P.; Sessolo, M.; Hadipour, A.; Bolink, H. J. Interfacial Modification for High-Efficiency Vapor-Phase-Deposited Perovskite Solar Cells Based on a Metal Oxide Buffer Layer. *J. Phys. Chem. Lett.* **2018**, *9*, 1041−1046.
(49) Chirvony, V. S.; González-Carrero, S.; Suárez, I.; Galian, R. E.; Sessolo, M.; Bolink, H. J.; Martínez-Pastor, J. P.; Pérez-Prieto, J. Delayed Luminescence in Lead Halide Perovskite Nanocrystals. *J. Phys. Chem. C* **2017**, *121*, 13381−13390.
(50) Abdi-Jalebi, M.; Andaji-Garmaroudi, Z.; Cacovich, S.; Stavrakas, C.; Philippe, B.; Richter, J. M.; Alsari, M.; Booker, E. P.; Hutter, E. M.; Pearson, A. J.; Lilliu, S.; Savenije, T. J.; Rensmo, H.; Divitini, G.; Ducati, C.; Friend, R. H.; Stranks, S. D. Maximizing and stabilizing luminescence from halide perovskites with potassium passivation. *Nature* **2018**, *555*, 497−501.
(51) Azpiroz, J. M.; Mosconi, E.; Bisquert, J.; De Angelis, F. Defect migration in methylammonium lead iodide and its role in perovskite solar cell operation. *Energy Environ. Sci.* **2015**, *8*, 2118−2127.
(52) Brenes, R.; Guo, D.; Osherov, A.; Noel, N. K.; Eames, C.; Hutter, E. M.; Pathak, S. K.; Niroui, F.; Friend, R. H.; Islam, M. S.; Snaith, H. J.; Bulović, V.; Savenije, T. J.; Stranks, S. D. Metal Halide

DOI: 10.1021/acsami.8b13100
ACS Appl. Mater. Interfaces XXXX, XXX, XXX−XXX

Perovskite Polycrystalline Films Exhibiting Properties of Single Crystals. *Joule* **2017**, *1*, 155−167.
(53) Juarez-Perez, E. J.; Hawash, Z.; Raga, S. R.; Ono, L. K.; Qi, Y. Thermal degradation of $CH_3NH_3PbI_3$ perovskite into NH_3 and CH_3I gases observed by coupled thermogravimetry-mass spectrometry analysis. *Energy Environ. Sci.* **2016**, *9*, 3406−3410.
(54) Olthof, S.; Meerholz, K. Substrate-dependent electronic structure and film formation of $MAPbI_3$ perovskites. *Sci. Rep.* **2017**, *7*, 40267.
(55) Xu, W.; McLeod, J. A.; Yang, Y.; Wang, Y.; Wu, Z.; Bai, S.; Yuan, Z.; Song, T.; Wang, Y.; Si, J.; Wang, R.; Gao, X.; Zhang, X.; Liu, L.; Sun, B. Iodomethane-mediated organometal halide perovskite with record photoluminescence lifetime. *ACS Appl. Mater. Interfaces* **2016**, *8*, 23181−23189.
(56) Liu, L.; McLeod, J. A.; Wang, R.; Shen, P.; Duhm, S. Tracking the formation of methylammonium lead triiodide perovskite. *Appl. Phys. Lett.* **2015**, *107*, 061904.

DOI: 10.1021/acsami.8b13100
ACS Appl. Mater. Interfaces XXXX, XXX, XXX−XXX

6 Influence of hole transport material ionization energy on the performance of perovskite solar cells

Hybrid organic-inorganic metal perovskites are promising candidates for the next generation of thin film photovoltaics due to excellent photophysical properties such as weak exciton binding energies, sharp absorption onset, long carrier diffusion length and low trap densities.[81,83,84,110–113] While these properties are fairly well rationalized, some of the basic working mechanisms of the solar cells are still under debate. A lot of effort was spent developing different hole-transport materials with different ionization potentials (IP) and energy level alignments with the perovskite, as a high V_{oc} was attributed to a high potential difference between the IP of the HTM and the electron affinity of the electron transporting material. One way of systematically investigating the link between the energy alignment and ionization potential/electron affinity with the V_{oc} is to make use of the diversity of HTMs available. It was previously reported that the use of HTMs with increasing IP systematically increases the Voc[114–116]. Nevertheless this trend seems not to be reflected looking at record performing perovskite solar cells where high V_{oc}`s have been reported for HTMs with both high IP with aligned energy levels and low IP with non-aligned energy levels[106,117]. A minimal effect of the HTM IP on the V_{oc} was also reported by Belisle et al.[118]. Nevertheless, this work suffers from the fundamental limitation of solution processed solar cells. When the perovskite is spin-coated in a p-i-n architecture on different HTMs, the resulting morphology is heavily affected by the surface of the HTM, most likely leading to different grain sizes and trap densities. When the perovskite is deposited on the electron transport material (ETM) and later capped with the HTMs, the morphology and thus trap density is not dependent on the latter. Nevertheless, in such a device layout the great majority of the carries

is generated at the ETM/perovskite interface thus reducing the effect of the HTM and possibly underestimating its impact on the V_{oc}. A possible solution to this problem is to fully evaporate the solar cells structure in a p-i-n layout. The morphology of evaporated perovskite active layers is insensitive to the underlying layer which most likely leads to comparable trap densities at the perovskite/HTM interface.

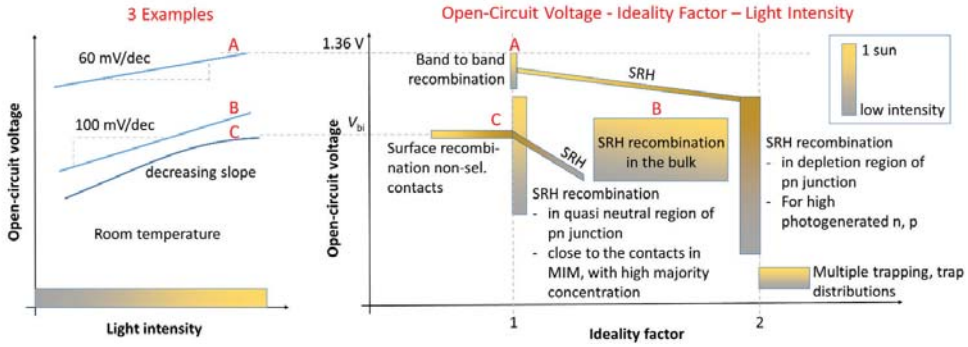

Figure 22. Ideality factor for different recombination mechanisms and corresponding trends in V_{oc} with illumination intensity (gradient). The shaded areas show possible combinations of n_{ID} and V_{oc}, where V_{oc} is not to scale. The ideality factor can change with illumination intensity and increase for lower V_{oc} (tilted areas), in particular if radiative or surface recombination appear paired with SRH recombination, with the latter dominating at lower light intensities. However, high V_{oc} is possible for high n_{ID} and n_{ID} is not a simple quality factor correlated with Voc. SRH recombination can lead to ideality factors between 1 and 2. The left diagram shows three examples, how a measurement of V_{oc} vs. illumination intensity would look like in cases A–C. Adapted from reference. [119]

The trap density is a crucial parameter as recombination losses reduce the V_{oc} in a solar cell. However, it is not trivial to identify possible recombination losses and disentangle bulk from surfaces processes. The type of recombination can be identified by means of ultrafast spectroscopy. The

absorber is excited with a defined laser pulse and the relaxation of the excited carrier is observed. Depending on the relaxation dynamics one is able to distinguish between trap mediated, direct, or Auger-recombination (details can be found in the introduction, "Basic processes of operating perovskite solar cells and light emitting devices"). Nevertheless, ultrafast spectroscopy is a complex technique and cannot distinguish between bulk and surface recombination. One way to shed light on both location and type of recombination is to measure of ideality factors. Ideality factors (n_{ID}) can be either extracted measuring the V_{oc} as a function of light intensity or from dark JV-curves. Measuring the current as a function of voltage we find[119]:

$$J_{dark}(V) = J_0 \left(exp \frac{eV}{n_{ID} k_B T} - 1 \right)$$

With k_B being the Boltzmann constant and T being the Temperature. Here n_{ID} can be extracted from the slope of the exponential region of the JV curve. Nevertheless, the diode equation does not take parasitic resistance into account and was thus not applied in this work. From semiconductor theory using the Boltzmann statistics and Born-Oppenheimer approximation the V_{oc} can be also expressed as: [120,121]

$$eV_{oc} = E_g - k_B T \; ln \frac{N_C N_V}{np}$$

With E_g being the bandgap and n and p concentration of electrons and holes occupying the effective density of states in the conducting and valence band (N_C,N_v). n and p are determined by the equilibrium between the carrier generation and their recombination. For the recombination we take into account band to band electron-hole recombination and Shockley-Read-Hall

(SRH) recombination. The V_{oc} depends logarithmically on the light intensity *I* and introducing the ideality factor n_{ID} as a pre-factor we find[119]:

$$eV_{oc} = E_g - n_{ID}k_BT\ ln\frac{I_0}{I}$$

I_0 is a constant with the same unit as I. In a pn-junction n_{ID} = 1 for band to band recombination in the quasi-neutral region whereas n_{ID} = 2 for SRH recombination in the depletion region (Figure 22). In the following we will explain how to transfer this concept to perovskite solar cells, where electron and hole carrier densities are balanced and quasi-neutral regions and depletion regions are not present.

Experimental Section

Perovskite films deposition and diodes fabrication.

ITO-coated glass substrates were subsequently cleaned with soap, water and isopropanol in an ultrasonic bath, followed by UV-ozone treatment. Substrate were transferred to a vacuum chamber integrated into a nitrogen-filled glovebox (H_2O and O_2 < 0.1 ppm) and evacuated to a pressure of 10^{-6} mbar. The vacuum chamber is equipped with six temperature controlled evaporation sources (Creaphys) fitted with ceramic crucibles. Three quartz crystal microbalance (QCM) sensors are used, two monitoring the deposition rate of each evaporation source and a third one close to the substrate holder monitoring the total deposition rate. For the HTMs we used 4,4',4''-Tris[(3-methylphenyl)phenylamino]triphenylamine (m-MTDATA), tris(4-carbazoyl-9-ylphenyl)amine (TcTa), TaTm whereas the fullerene (C_{60}) and BCP where used as ETM. For thickness calibration we individually sublimed the materials and a calibration factor was obtained by comparing the thickness inferred from the QCM sensors with that measured with a mechanical profilometer (Ambios XP1). After HTL deposition, the chamber was vented with dry N_2 to replace the crucibles with those containing the starting materials for the perovskite deposition, PbI_2 and CH_3NH_3I. The vacuum chamber was evacuated again to a pressure of 10^{-6} mbar, and the perovskite films were then obtained by co-deposition of the two precursors. MAI was evaporated with a temperature of approximately 70 °C and PbI_2 with a temperature between 255 °C and 300 °C to obtain a final perovskite thickness of around 600 nm. After deposition of the perovskite films, the chamber was vented and the crucibles replaced with those containing C_{60} and BCP, and evacuated again to a pressure of 10^{-6} mbar. Finally the substrates were transferred to a

second vacuum chamber where the silver top contact (100 nm thick) was deposited.

Device and film characterization.

The EQE was estimated using the cell response at different wavelength (measured with a white light halogen lamp in combination with band-pass filters), where the solar spectrum mismatch is corrected using a calibrated Silicon reference cell (MiniSun simulator by ECN, the Netherlands). The current density-voltage (JV) characteristics were obtained using a Keithley 2612A source measure under white light illumination using a solar simulator by Abet Technologies (model 10500 with an AM1.5G xenon lamp as the light source). Optical filters were used to reduce the light intensity when needed. The scan rate was 0.1 V/s. Before each measurement, the exact light intensity was determined using a calibrated Si reference diode equipped with an infrared cut-off filter (KG-3, Schott). Photoelectron spectroscopy in air measurements was carried out using a APS02 system (KP Technology)

Femtosecond Transient Absorption Spectroscopy:

TA measurements were performed with 600 nm pulsed excitation, generated in an optical parametric amplifier (OPerA, Coherent) from the fundamental pulses of an amplified Ti:sapphire laser system (35 fs, 800 nm, 1 kHz, 6 mJ, Astrella, Coherent). The broadband white light probe pulses were generated by focusing the fundamental beam on a sapphire plate, then split into a reference and a signal component. The pump pulses were chopped at half the laser frequency to allow shot-to-shot detection. The pump and probe beam diameters were measured with a beam profilometer (1 mm and 260 µm, respectively), ensuring a uniform distribution of detected photo-excited

species. The probe pulses were temporally delayed relative to the excitation pulses via a micrometer translation stage, and pump-probe delays up to 2 ns were measured. The probe pulses transmitted through the sample and the reference probe pulses were spectrally dispersed in a home-build prism spectrograph, assembled by Entwicklungsbüro Stresing (Berlin) and detected shot-to-shot by a pair of back-thinned silicon CCDs (Hamamatsu S07030-0906).

Results and discussion

Here we present a series of fully evaporated perovskites solar cells with different HTMs, namely m-MTDATA, TaTm and TcTa (Figure 23**Error! Reference source not found.**). Their ionization potential of 5.02 eV, 5.38 eV, 5.68 eV was measured using photoelectron spectroscopy in air (see Figure 24). The devices were fabricated in a p-i-n architecture with glass/ITO/HTM/MAPI/C_{60}/BCP/Silver. Using a p-i-n structure ensures that the majority of the carriers are generated at the HTM/perovskite interface. Devices produced with m-MTDATA and TcTa showed almost no difference in V_{oc} (1008 mV and 1000 mV, respectively) despite the IP difference of 0.66 eV. The highest V_{oc} obtained for TaTm (1060 mV) could be ascribed to a different dominating recombination process compared to devices base on m-MTDATA and TcTa.

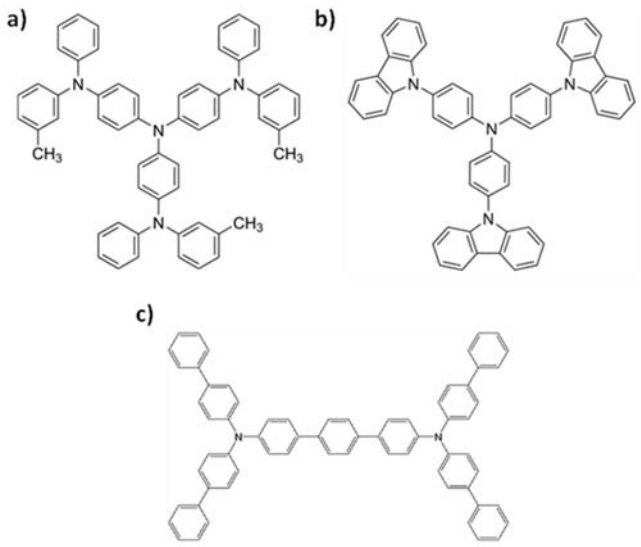

Figure 23. Organic hole-transport materials investigated in this study. a) m-MTDATA , b) TcTa, c) TaTm.

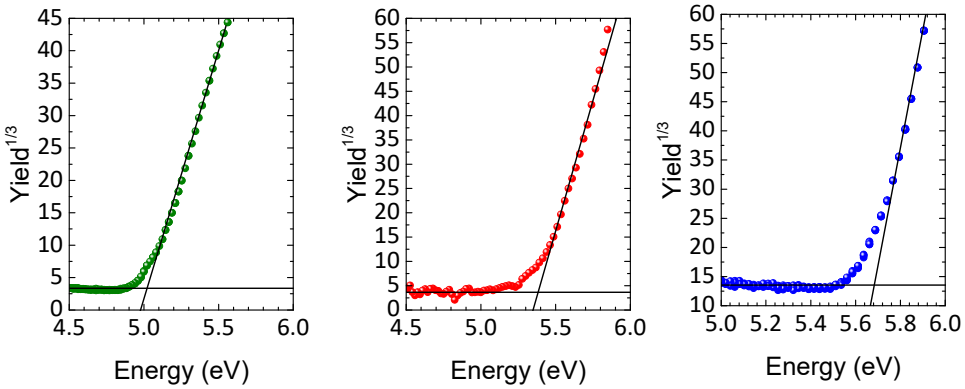

Figure 24. Photo-electron spectroscopy in air for m-MTDATA (green), TaTm (red) and TcTa (blue). Solid lines show fitted base and trend lines. The extrapolated ionization energies are 5.02 eV, 5.38 eV, 5.68 eV for m-MTDATA, TaTm and TcTa respectively.

The dominant type of recombination was investigated by measuring the V_{oc} as a function of light intensity.[119] Figure 25 shows the light intensity dependent V_{oc}`s and ideality factors for devices with different HTMs. As described in the introduction, the ideality factors were extracted using Boltzmann statistics and Born-Oppenheimer approximation measuring the $V_{oc}$`s as a function of light intensity. We found ideality factors of ~1.7 for TaTm and ~1.2 for TcTa and m-MTDATA. In perovskite solar cells, ideality factors close to two are usually interpreted as non-radiative SRH recombination and ideality factors close to one are attributed to direct recombination which is usually interpreted as non-radiative surface recombination (if the associated V_{oc} is low compared to the absorber's band gap) or to radiative bulk recombination (in case of high V_{oc}'s). [119] Therefore, against common believe, low ideality factors are not necessarily beneficial. In fact several perovskite solar cells with low ideality factors and low V_{oc} have been reported. [122–124] The higher ideality factor of TaTm compared to TcTa and m-MTDATA point towards an enhanced surface recombination which limits the V_{oc} in case of TcTa and m-MTDATA, while the V_{oc} of TaTm is mainly limited by SRH-recombination. The origin of the larger surface recombination at the MAPI/TcTa or MAPI/m-MTDATA interface is not clear yet. Nevertheless, the IP of the HTM itself is unlikely to influence the splitting of the quasi-Fermi levels, in particular the position of the quasi-Fermi level for holes (E_{Fh}), which is determined by the absorber. This is justified by the low exciton binding energy[20] and small dark charge carrier density[125] of MAPI, and it is in line with previous observations where modifications of the HTM and ETM energetics did not affect the photovoltage [118,126]. However, our results also suggest that it is possible to use HTMs with a HOMO lower than

the absorber's valence band without a significant voltage penalty associated to the energetics. It is thus important to analyze the other photovoltaic parameters.

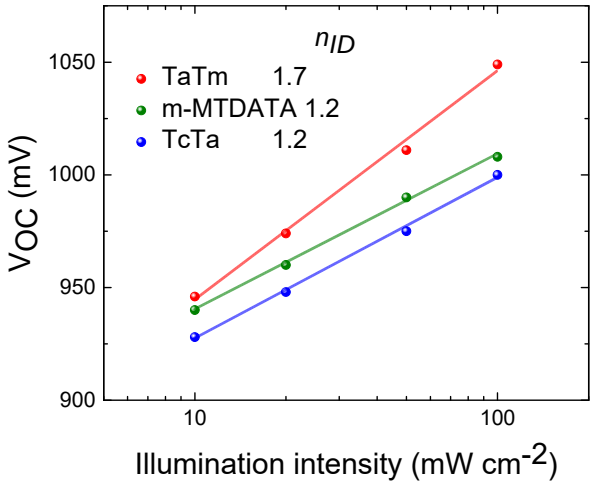

Figure 25. Light intensity dependent V_{oc} and extracted ideality factors for perovskite solar cells with different HTMs.

Table 1. IPs of different HTMs and representative photovoltaic parameters obtained when implemented in solar cells

HTM	IP (eV)	PCE (%)	V_{oc} (mV)	J_{sc} (mA/cm^2)	FF (%)
m-MTDATA	5.0	14.4 ± 1.20	1008 ± 4	18.9 ± 0.52	75 ± 3.0
TaTm	4.4	16.3 ± 0.76	1060 ± 6	20.1 ± 0.84	76 ± 1.2
TcTa	5.7	12.2 ± 1.60	1000 ± 8	18.9 ± 1.13	64 ± 9.0

Representative current-voltage characteristics measured under 100 mW cm^{-2} illumination in forward and reverse bias are displayed in Figure 26a, whereas the respective photovoltaic parameters can be found in Table 1. Slight current-voltage hysteresis is only visible in the TcTa based device, and it is negligible in all the other cases. Devices based on TaTm show the highest current, 20.12 mA cm^{-2}, in contrast to the ones based on TcTa and m-MTDATA, which are 1.22 mA/cm^{-2} lower. The three solar cells mainly differ in FF, with TaTm and m-MTDATA having high values of around 75 % and TcTa having a lower FF of 64 %. This can be attributed to a higher series resistance of the devices using TcTa as HTM, which is also reflected in the dark IV-curve above around 1V (Figure 26d).

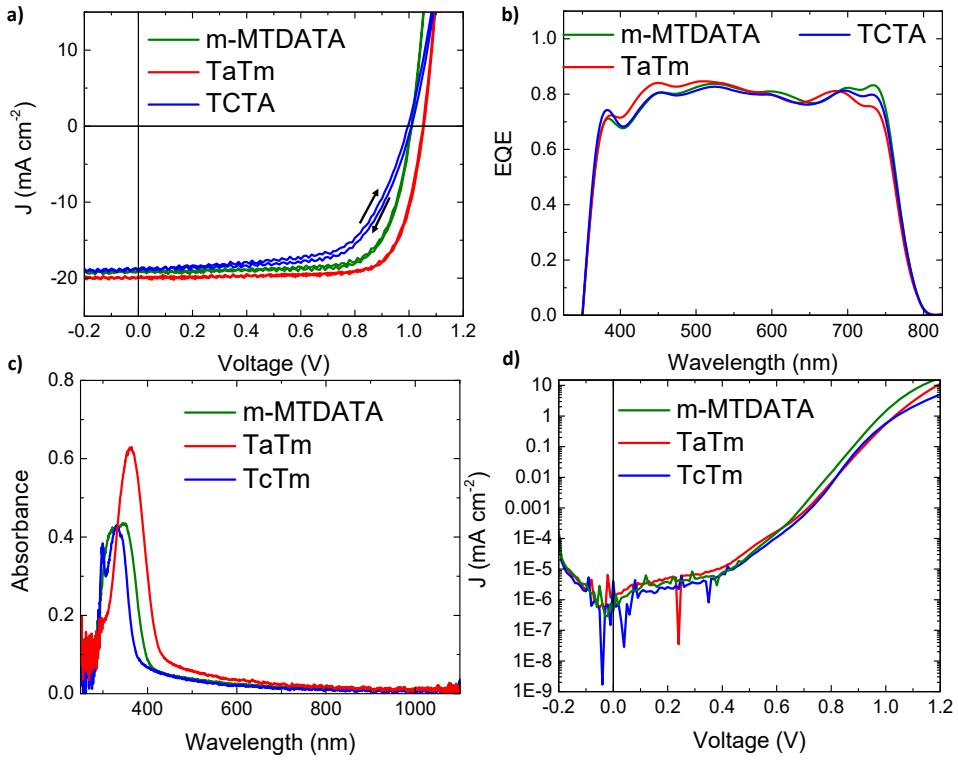

Figure 26. (a) JV curves of perovskite solar cells produced with different 5 nm thick HTMs under 100 mW cm^{-2} illumination in forward and reverse bias, (b) EQE spectra, (c) **a**bsorption of HTMs and (d) JV curves in the dark.

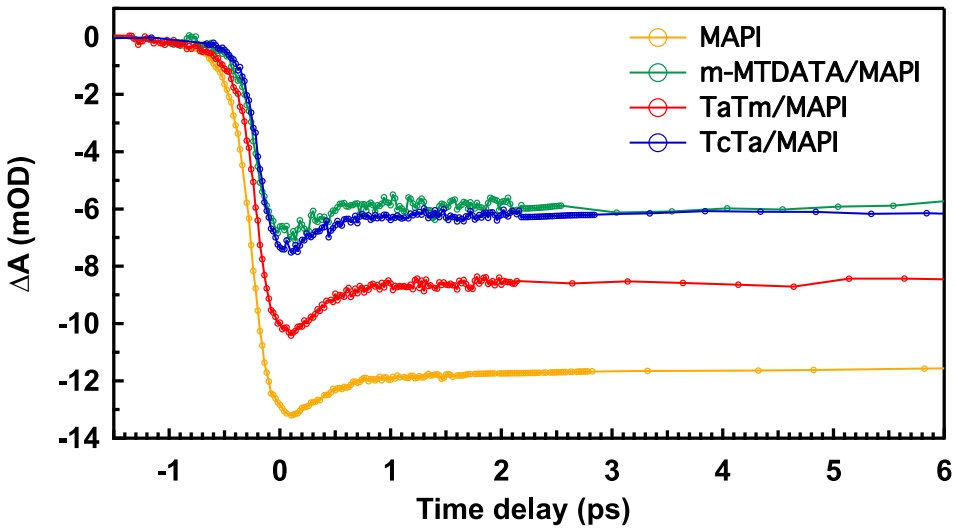

Figure 27. Time-resolved transient absorption dynamics for neat MAPI and the perovskite/HTM double layers, excited at 600 nm (at constant excitation density of $1.4 \cdot 10^{17}$ cm^{-3}) and probed at the perovskite maximum ground state bleaching band.

The EQE curves shown in Figure 26b are very similar which due to the very low absorption of the HTMs and their good extraction properties despite the HOMO level mismatch with the perovskite valence band in case of TcTa and m-MTDATA. To confirm this point, the charge injection from MAPI to the HTMs was studied using femtosecond transient absorption spectroscopy (TA). Figure 27 shows the time-resolved transient absorption dynamics for perovskite/HTM double layers. Samples were excited with laser pulses at 600 nm with a constant excitation density of $1.4 \cdot 10^{17}$ cm^{-3}, and probed at the maximum of the perovskite ground state bleaching (GSB) band. An instantaneously reduced signal in the perovskite GSB is observed upon the addition of the HTMs, indicating that the hole injection takes place for all HTMs, even faster than the time resolution of the setup of about 60 fs.

In Summary we produced a series of fully evaporated perovskite solar cells changing the HTMs which showed a difference in IP of around 0.66 eV. Devices produced with TaTm showed a V_{oc} of around 1060 mV whereas TcTa and m-MTDATA showed a V_{oc} of 1000 mV. Measuring the V_{oc} as a function of light intensity we were able to extract the ideality factors and thus concluded that the difference in V_{oc} solely depend on the recombination in the bulk and at the interface rather than on the energetic offset between the valence band of the perovskite and the highest occupied molecular orbital of the organic transport layers. These results will help to develop novel charge transport materials to further improve the performance of perovskite solar cells.

Journal of
Materials Chemistry C

PAPER

View Article Online
View Journal

Cite this: DOI: 10.1039/c8tc05372c

Influence of hole transport material ionization energy on the performance of perovskite solar cells†

Benedikt Dänekamp,[a] Nikolaos Droseros,[b] Demetra Tsokkou,[b] Verena Brehm,[a] Pablo P. Boix,*[a] Michele Sessolo,[a] Natalie Banerji[b] and Henk J. Bolink[a]

Received 24th October 2018,
Accepted 25th November 2018

DOI: 10.1039/c8tc05372c

rsc.li/materials-c

Halide perovskites have shown excellent photophysical properties for solar cell applications which led to a rapid increase in device efficiency. Understanding the charge carrier dynamics within an active perovskite absorber and at its interfaces will be the key to further progress in their development. Here we present a series of fully evaporated devices employing hole transport materials with different ionization energies. The open circuit voltage of the devices, along with their ideality factors, confirms that the former is mainly determined by the bulk and surface recombination in the perovskite, rather than by the energetic offset between the valence band of the perovskite and the highest occupied molecular orbital of the organic transport layers. These results help to further understand the origin of the open circuit potential in perovskite solar cells, which is an important parameter that needs to be improved to further boost power conversion efficiencies.

Introduction

Perovskite solar cells are one of the most interesting alternatives to current photovoltaic technologies. Since the first reports of solid state solar cells based on methylammonium lead iodide (MAPI),[1,2] the development of this technology has resulted in a rapid increase in device efficiencies, exceeding 22%.[3] Identifying the unique properties of halide perovskites is essential to understand the reasons for this remarkable progress. In this regard, unveiling long charge carrier diffusion lengths,[4–6] sharp optical absorption edges[7] and weak exciton binding energies[8–10] are some of the key discoveries that contributed to explain the excellent device performances, as well as to gauge the full material potential.

However, there is still some debate regarding the main factors affecting the open circuit potential (V_{oc}) of the devices.[11] In general, the splitting of the electron and hole quasi-Fermi levels defines the maximum achievable V_{oc}, and it is determined by charge generation/recombination rates along with the distribution of electronic states and charge carriers of the materials.[12] In multilayer perovskite solar cells, the problem shifts towards the role of the charge selective and transporting layers in contributing to the final V_{oc}. Several reports have associated the high achieved V_{oc} with a high energy difference between the highest occupied molecular orbitals (HOMOs) of the hole transport material (HTM) and the lowest unoccupied molecular orbitals (LUMOs) of the electron transport material (ETM), together with good alignment of these energy levels with the perovskite valence and conduction bands, respectively.[13–18] Although some reports show an increase in V_{oc} for HTMs with a higher ionization energy (IE),[17,19,20] this trend is not necessarily reflected in the record performance of perovskite solar cells, where the best V_{oc}'s have been reported for both high HOMO (closer to the vacuum level) HTMs with well-aligned energy levels; and low HOMO (further from the vacuum level) HTMs with non-perfectly aligned energy levels.[21,22] More specifically, recent publications discuss the negligible V_{oc} dependence on the ETM[23] and HTM energy levels.[24] This view is also in line with previous results, where V_{oc}'s higher than that expected from the HTM energy levels were obtained.[17] However, in all these cases, the HOMO of the employed HTM was close in energy to or just above the perovskite valence band maximum (reciprocally, the LUMO level of the ETM was aligned or slightly below the perovskite conduction band).

Analyzing the effect of a set of HTMs with different HOMO energies appears to be a straightforward approach to systematically investigate the relationship between the V_{oc} and the energy levels of the extraction layers. However, it is important to note that the replacement of the HTM can also affect the interfacial charge recombination,[25] which has a large impact on the V_{oc}. In addition, the vast majority of studies suffer from the limitations associated with solution-processed solar cells.

[a] Instituto de Ciencia Molecular, Universidad de Valencia, C/Catedrático J. Beltrán 2, 46980 Paterna (Valencia), Spain. E-mail: Pablo.P.Boix@uv.es
[b] Department of Chemistry and Biochemistry, University of Bern, Freiestrasse 3, CH-3012 Bern, Switzerland

† Electronic supplementary information (ESI) available. See DOI: 10.1039/c8tc05372c

This is in particular the case for p–i–n device architectures in which the holes are extracted through the front contact. In this configuration, the polar solutions containing the perovskite precursors are applied onto the apolar aromatic HTMs, leading to poor wetting and consequently poorly controlled film growth. Hence the resulting perovskite film is strongly affected by the surface of the HTM,[26] leading to different morphologies and, most likely, different trap densities. Moreover, most studies have been carried out on n–i–p solar cells, where a large majority of charge carriers are generated at the ETM/perovskite interface, which could reduce the effect of the HTM and underestimate its impact on the V_{oc}.[17,24]

Here, we present a series of fully vacuum deposited perovskite solar cells with different HTMs. Vacuum deposition allows for the direct modification or substitution of any layer in the device stack with a negligible effect on the rest, as no solvents are used and hence no wetting or de-wetting occurs. In addition, the high voltages previously obtained with vacuum-deposited MAPI solar cells, which indicates the absence of non-radiative recombination paths at the selective interfaces,[21] make it an ideal reference system to study interfacial modifications. Therefore, we are able to produce and study high efficiency perovskite solar cells based on a series of HTMs with more than 0.66 eV difference in their IE, including materials with IE more than 0.3 eV higher and lower than the perovskite valence band.

Results and discussion

The different vacuum-deposited materials used as HTMs are 4,4′,4″-tris[phenyl(*m*-tolyl)amino]triphenylamine (*m*-MTDATA), *N*4,*N*4,*N*4″,*N*4″-tetra([1,1′-biphenyl]-4-yl)-[1,1′:4′,1″-terphenyl]-4,4″-diamine (TaTm) and tris(4-carbazoyl-9-ylphenyl)amine (TcTa). Their respective ionization energies of 5.0 eV, 4.4 eV, and 5.7 eV (Fig. 1a) were measured using photo-electron spectroscopy in air (see the ESI,† Fig. S1). The solar cells were fabricated following a p–i–n architecture consisting of pre-patterned ITO on glass with ITO, MoO_3, HTM, MAPI, fullerene (C_{60}), 2,9-dimethyl-4,7-diphenyl-1,10-phenanthroline (BCP) and Ag as a top contact (Fig. 1b). Detailed experimental conditions can be found in the ESI.† Using a p–i–n device structure ensures that the majority of carriers are generated at the HTM/perovskite interface. Representative current–voltage characteristics measured under 100 mW cm^{-2} illumination in forward and reverse bias are displayed in Fig. 2a, whereas the corresponding photovoltaic parameters with the associated statistical error (>10 samples per parameter) can be found in Table 1. Slight current–voltage hysteresis is only visible in the TcTa based device, while it is negligible in the other cases. Devices based on TaTm show the highest current, 20.1 mA cm^{-2}, in contrast to the ones with TcTa and *m*-MTDATA, which are 1.2 mA cm^{-2} lower. The FFs of the TaTm and *m*-MTDATA based devices are comparable (76% and 75% respectively), with a lower

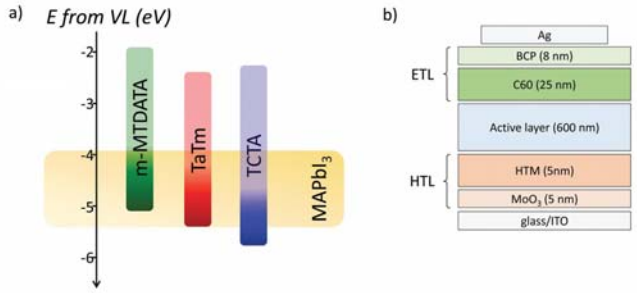

Fig. 1 (a) Energy diagram of different HTMs with respect to MAPI. The energy values of the HOMOs were determined by photoemission spectroscopy in air (PESA) (see the ESI,† Fig. S1). (b) Scheme of the completed stack with different HTMs.

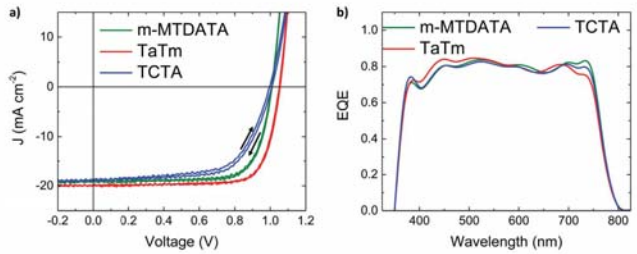

Fig. 2 (a) *J*–*V* curves under 100 mW cm^{-2} illumination in forward and reverse bias and (b) EQE spectra of representative perovskite solar cells produced with different 5 nm thick HTMs.

Table 1 IEs of different HTMs and representative photovoltaic parameters obtained when implemented in solar cells

HTM	IE (eV)	PCE (%)	V_{oc} (mV)	J_{sc} (mA cm^{-2})	FF
m-MTDATA	5.0	14.4 ± 1.2	1008 ± 4	18.9 ± 0.5	75 ± 3
TaTm	4.4	16.3 ± 0.8	1060 ± 6	20.1 ± 0.8	76 ± 1
TcTa	5.7	12.2 ± 1.6	1000 ± 8	18.9 ± 1.1	64 ± 9

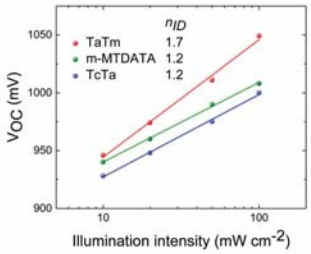

Fig. 3 Light intensity dependent V_{oc} and extracted ideality factors for perovskite solar cells with different HTMs.

value (64%) obtained for the solar cells employing TcTa. More interestingly, devices with *m*-MTDATA and TcTa show almost no difference in V_{oc} (1.008 V and 1.000 V) yet with an IE difference as large as 0.66 eV among them. Devices with TaTm present the highest V_{oc} of 1060 mV. Since these results do not show any evident trend between the HTM energetics and the resulting V_{oc}, further studies were carried out to elucidate the relationship among those parameters.

The dominant type of recombination was investigated by measuring the V_{oc} as a function of light intensity.[27] Fig. 3 shows the light intensity dependent V_{oc} and ideality factor for devices with different HTMs. The V_{oc} depends logarithmically on the light intensity and introducing the ideality factor n_{ID} as a pre-factor we find:[27]

$$eV_{oc} = E_g - n_{ID}k_BT\ln\frac{I_0}{I} \quad (1)$$

with E_g being the bandgap, T the temperature, k_B the Boltzmann constant and I_0 the reverse saturation current. Measuring the V_{oc} as a function of light intensity for devices with varying HTMs results in ideality factors of ~1.7 for TaTm and ~1.2 for TcTa and *m*-MTDATA. Ideality factors close to one can be attributed to direct recombination, which is usually interpreted as non-radiative surface recombination (if the associated V_{oc} is low compared to the absorber's band gap), or to radiative bulk recombination (in the case of high V_{oc}'s). Ideality factors close to 2 are usually associated with non-radiative Shockley-Read-Hall recombination. Therefore, against the common belief, low ideality factors are not necessarily beneficial. In fact, several perovskite solar cells with low ideality factors and low V_{oc} have been reported.[11,28,29]

Considering this, devices using TaTm show a higher V_{oc} and an ideality factor of 1.7, while the solar cells with TcTa and *m*-MTDATA have a lower V_{oc} and an ideality factor of 1.2. This points towards an enhanced surface recombination which limits the V_{oc} of the TcTa and *m*-MTDATA devices, while the V_{oc} of TaTm is mainly determined by SRH-recombination. The origin of the larger surface recombination at the interface between MAPI and TcTa or *m*-MTDATA is not clear yet. The IE of the HTM itself is unlikely to influence the splitting of the quasi-Fermi levels, in particular the position of the holes' quasi-Fermi level (E_{Fh}), which is determined by the absorber. This is justified by the low exciton binding energy[30] and the small dark charge carrier density[31] of MAPI, and it is in line with previous observations where modifications of the HTM and ETM energetics did not affect the photovoltage.[23,24] In addition, our results also suggest that it is possible using HTMs with a HOMO lower than the absorber's valence band without a significant voltage penalty associated with the energetics.

It is thus important to discuss the implications of these HTMs in the other relevant photovoltaic parameters of the devices.

The three solar cells mainly differ in FF, with TaTm and *m*-MTDATA having high values of around 75 and TcTa having a lower FF of 64. This can be attributed to a higher series resistance of the diode employing TcTa, as also reflected in the dark IV-curve above 1 V, and it is likely related with the relatively large barrier for hole injection/extraction at the TcTa/MAPI interface (Fig. S2, ESI†). All devices reach relatively high short circuit currents, 20.1 mA cm^{-2} for TaTm and 18.9 mA cm^{-2} for TcTa and *m*-MTDATA. The EQE curves shown in Fig. 2b are very similar which is consistent with the results discussed before. This point highlights the good extraction of the photogenerated charges obtained with both TcTa and *m*-MTDATA despite their HOMO level mismatch with the perovskite valence band. To confirm this point, the charge injection from MAPI to the HTMs was studied using femtosecond transient absorption spectroscopy (TAS). Fig. 4 shows the time-resolved transient absorption dynamics for perovskite/HTM double layers. The samples were excited with laser pulses at 600 nm with a constant excitation density of 1.4 × 10^{17} cm^{-3}, and probed at the maximum of the perovskite ground state bleaching (GSB) band. An instantaneously reduced signal in the perovskite GSB band is observed upon the addition of the HTMs,

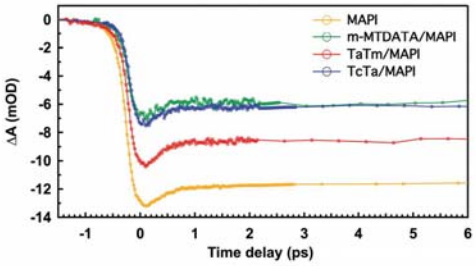

Fig. 4 Time-resolved transient absorption dynamics for neat MAPI and the perovskite/HTM double layers, excited at 600 nm (at a constant excitation density of 1.4 × 10^{17} cm^{-3}) and probed at the maximum of the perovskite ground state bleaching band.

indicating that the hole injection takes place for all HTMs, even faster than the time resolution of the setup of about 60 fs. The TA spectra at different time delays after excitation for the perovskite/TaTm bilayer are shown in Fig. S5 (ESI†). A detailed photophysical study of the systems will be published subsequently.

Conclusions

In summary, we produced a stack of fully evaporated devices based on different HTMs with an IP-difference as high as 0.66 eV among them. Devices produced with these HTMs showed V_{oc}'s ranging from 1000 mV (TcTa) to 1060 mV (TaTm). The measurement of the respective ideality factors allows us to explain the differences in V_{oc} by the nature of the recombination processes. These results support that the V_{oc} of perovskite solar cells is not necessarily limited by the energetics of the hole transporting material, but mainly by the different recombination paths. In addition, we show efficient charge extraction by HTMs with a misaligned HOMO with the perovskite (>300 meV above and below the perovskite's valence band). These results point towards HTM designing routes that can improve the performance of perovskite solar cells, focusing on the interfacial recombination reduction rather than on the energetic alignment.

Conflicts of interest

There are no conflicts to declare.

Acknowledgements

The authors would like to acknowledge financial support from the European Union H2020 project INFORM (grant 675867). N. D., D. T. and N. B. would like to acknowledge the University of Bern, Switzerland, for providing funding and infrastructure. Financial support is acknowledged from the Spanish Ministry of Economy and Competitiveness (MINECO) *via* the Unidad de Excelencia María de Maeztu MDM-2015-0538, MAT2017-88821-R, PCIN-2015-255, PCIN-2017-014 and the Generalitat Valenciana (Prometeo/2016/135). P. B and M. S. thank the MINECO for their RyC contracts. P. B. acknowledges the financial support from the Conselleria d'Educació, Investigació, Cultura i Esport Valenciana (SEJI2017/2017/012).

References

1 M. M. Lee, Efficient Hybrid Solar Cells Based on Meso-Superstructured Organometal Halide Perovskites, *Science*, 2012, **338**(6107), 643–647, DOI: 10.1126/science.1228604.
2 H.-S. Kim, C.-R. Lee and J.-H. Im, *et al.*, Lead Iodide Perovskite Sensitized All-Solid-State Submicron Thin Film Mesoscopic Solar Cell with Efficiency Exceeding 9%, *Sci. Rep.*, 2012, **2**, 591, DOI: 10.1038/srep00591.
3 W. S. Yang, B.-W. Park and E. H. Jung, *et al.*, Iodide management in formamidinium-lead-halide-based perovskite layers for efficient solar cells, *Science*, 2017, **356**(6345), 1376–1379, DOI: 10.1126/science.aan2301.
4 W. Nie, H. Tsai and R. Asadpour, *et al.*, High-efficiency solution-processed perovskite solar cells with millimeter-scale grains, *Science*, 2015, **347**(6221), 522–525, DOI: 10.1126/science.aaa0472.
5 D. Shi, V. Adinolfi and R. Comin, *et al.*, Low Trap-State Density and Long Carrier Diffusion in Organolead Trihalide Perovskite Single Crystals, *Science*, 2015, **347**(6221), 519–522, DOI: 10.1126/science.aaa2725.
6 G. Xing, N. Mathews and S. Sun, *et al.*, Long-Range Balanced Electron- and Hole-Transport Lengths in Organic-Inorganic $CH_3NH_3PbI_3$, *Science*, 2013, **342**(6156), 344–347, DOI: 10.1126/science.1243167.
7 S. De Wolf, J. Holovsky and S. J. Moon, *et al.*, Organometallic halide perovskites: Sharp optical absorption edge and its relation to photovoltaic performance, *J. Phys. Chem. Lett.*, 2014, **5**(6), 1035–1039, DOI: 10.1021/jz500279b.
8 Q. Lin, A. Armin, R. C. R. Nagiri, P. L. Burn and P. Meredith, Electro-optics of perovskite solar cells, *Nat. Photonics*, 2015, **9**(2), 106–112, DOI: 10.1038/nphoton.2014.284.
9 T. J. Savenije, C. S. Ponseca and L. Kunneman, *et al.*, Thermally activated exciton dissociation and recombination control the carrier dynamics in organometal halide perovskite, *J. Phys. Chem. Lett.*, 2014, **5**(13), 2189–2194, DOI: 10.1021/jz500858a.
10 Y. Yang, M. Yang, Z. Li, R. Crisp, K. Zhu and M. C. Beard, Comparison of Recombination Dynamics in $CH_3NH_3PbBr_3$ and $CH_3NH_3PbI_3$ Perovskite Films: Influence of Exciton Binding Energy, *J. Phys. Chem. Lett.*, 2015, **6**(23), 4688–4692, DOI: 10.1021/acs.jpclett.5b02290.
11 W. Tress, Perovskite Solar Cells on the Way to Their Radiative Efficiency Limit – Insights Into a Success Story of High Open-Circuit Voltage and Low Recombination, *Adv. Energy Mater.*, 2017, **7**, 1602358, DOI: 10.1002/aenm.201602358.
12 Y. Shao, Y. Yuan and J. Huang, Correlation of energy disorder and open-circuit voltage in hybrid perovskite solar cells, *Nat. Energy*, 2016, **1**(1), 1–9, DOI: 10.1038/nenergy.2015.1.
13 Y. Song, S. Lv and X. Liu, *et al.*, Energy level tuning of TPB-based hole-transporting materials for highly efficient perovskite solar cells, *Chem. Commun.*, 2014, **50**(96), 15239–15242, DOI: 10.1039/c4cc06493c.
14 M. Cheng, B. Xu and C. Chen, *et al.*, Phenoxazine-based small molecule material for efficient perovskite solar cells and bulk heterojunction organic solar cells, *Adv. Energy Mater.*, 2015, **5**(8), 1–9, DOI: 10.1002/aenm.201401720.
15 G.-W. Kim, G. Kang and J. Kim, *et al.*, Dopant-free polymeric hole transport materials for highly efficient and stable perovskite solar cells, *Energy Environ. Sci.*, 2016, **9**(7), 2326–2333, DOI: 10.1039/C6EE00709K.
16 K. Lim, H. Kim, J. Jeong, H. Kim, J. Y. Kim and T. Lee, Boosting the Power Conversion Efficiency of Perovskite Solar Cells Using Self-Organized Polymeric Hole Extraction Layers with High Work Function, *Adv. Mater.*, 2014, **26**(37), 1–6, DOI: 10.1002/adma.201401775.
17 S. Ryu, J. H. Noh and N. J. Jeon, *et al.*, Voltage output of efficient perovskite solar cells with high open-circuit voltage

and fill factor, *Energy Environ. Sci.*, 2014, **7**(8), 2614–2618, DOI: 10.1039/c4ee00762j.

18 J. Zhang, B. Xu and M. B. Johansson, *et al.*, Strategy to Boost the Efficiency of Mixed-Ion Perovskite Solar Cells: Changing Geometry of the Hole Transporting Material, *ACS Nano*, 2016, **10**(7), 6816–6825, DOI: 10.1021/acsnano.6b02442.

19 L. E. Polander, P. Pahner, M. Schwarze, M. Saalfrank, C. Koerner and K. Leo, Hole-transport material variation in fully vacuum deposited perovskite solar cells, *APL Mater.*, 2014, **2**(8), 081503, DOI: 10.1063/1.4889843.

20 M. Kulbak, D. Cahen and G. Hodes, How Important Is the Organic Part of Lead Halide Perovskite Photovoltaic Cells? Efficient $CsPbBr_3$ Cells, *J. Phys. Chem. Lett.*, 2015, **6**(13), 2452–2456, DOI: 10.1021/acs.jpclett.5b00968.

21 D. Pérez-del-Rey, P. P. Boix, M. Sessolo, A. Hadipour and H. J. Bolink, Interfacial Modification for High-Efficiency Vapor-Phase-Deposited Perovskite Solar Cells Based on a Metal Oxide Buffer Layer, *J. Phys. Chem. Lett.*, 2018, 1041–1046, DOI: 10.1021/acs.jpclett.7b03361.

22 W. Yu, S. Yu and J. Zhang, *et al.*, Two-in-one additive-engineering strategy for improved air stability of planar perovskite solar cells, *Nano Energy*, 2018, **45**, 229–235, DOI: 10.1016/j.nanoen.2017.12.041.

23 S. Ravishankar, S. Gharibzadeh and C. Roldán-Carmona, *et al.*, Influence of Charge Transport Layers on Open-Circuit Voltage and Hysteresis in Perovskite Solar Cells, *Joule*, 2018, **2**(4), 788–798, DOI: 10.1016/j.joule.2018.02.013.

24 R. A. Belisle, P. Jain, R. Prasanna, T. Leijtens and M. D. McGehee, Minimal Effect of the Hole-Transport Material Ionization Potential on the Open-Circuit Voltage of Perovskite Solar Cells, *ACS Energy Lett.*, 2016, **1**(3), 556–560, DOI: 10.1021/acsenergylett.6b00270.

25 Y. Yamada, T. Yamada, A. Shimazaki, A. Wakamiya and Y. Kanemitsu, Interfacial Charge-Carrier Trapping in $CH_3NH_3PbI_3$-Based Heterolayered Structures Revealed by Time-Resolved Photoluminescence Spectroscopy, *J. Phys. Chem. Lett.*, 2016, **7**, 1972–1977, DOI: 10.1021/acs.jpclett.6b00653.

26 D. P. McMeekin, Z. Wang, W. Rehman, F. Pulvirenti, J. B. Patel, N. K. Noel, M. B. Johnston, S. R. Marder, L. M. Herz and H. J. Snaith, Crystallization Kinetics and Morphology Control of Formamidinium–Cesium Mixed-Cation Lead Mixed-Halide Perovskite *via* Tunability of the Colloidal Precursor Solution, *Adv. Mater.*, 2017, **29**, 1607039, DOI: 10.1002/adma.201607039.

27 W. Tress, M. Yavari and K. Domanski, *et al.*, Interpretation and Evolution of Open-Circuit Voltage, Recombination, Ideality Factor and Subgap Defect States during Reversible Light-Soaking and Irreversible Degradation of Perovskite Solar Cells, *Energy Environ. Sci.*, 2017, **11**, 151–165, DOI: 10.1039/C7EE02415K.

28 K. Miyano, M. Yanagida, N. Tripathi and Y. Shirai, Simple characterization of electronic processes in perovskite photovoltaic cells, *Appl. Phys. Lett.*, 2015, **106**(9), 093903, http://scitation.aip.org/content/aip/journal/apl/106/9/10.1063/1.4914086, accessed March 5, 2015.

29 K. Miyano, N. Tripathi, M. Yanagida and Y. Shirai, Lead Halide Perovskite Photovoltaic as a Model p-i-n Diode, *Acc. Chem. Res.*, 2016, **49**(2), 303–310, DOI: 10.1021/acs.accounts.5b00436, accessed March 10, 2016.

30 A. Miyata, A. Mitioglu and P. Plochocka, *et al.*, Direct measurement of the exciton binding energy and effective masses for charge carriers in organic–inorganic tri-halide perovskites, *Nat. Phys.*, 2015, **11**, 582–587, DOI: 10.1038/nphys3357.

31 Y. Chen, H. T. Yi and X. Wu, *et al.*, Extended carrier lifetimes and diffusion in hybrid perovskites revealed by Hall effect and photoconductivity measurements, *Nat. Commun.*, 2016, **7**, 12253, DOI: 10.1038/ncomms12253.

7 Conclusions

The aim of this thesis was to get further inside into phenomena that are related to fundamental photophysical processes of perovskite solar cells and LEDs. The thesis was divided in three parts and the main conclusions for each of them are described below:

In the chapter “Perovskite-Perovskite Homojunctions via Compositional Doping” we described the production of a vertical MAPI homojunction obtained by vacuum deposition. The majority carrier density in the MAPI layers could be altered by changing the stoichiometry between the precursors MAI and PbI_2. A perovskite film produced with MAI-excess lead to p-type MAPI whereas an excess of PbI_2 lead to an n-type MAPI as shown by Kelvin Probe measurements on the film surface. By deposition the different majority carrier type MAPI on top of each other a compact bi-layer was obtained. This bi-layer was analyzed using a SKPM-setup which revealed a junction potential exceeding 250 mV. Devices with the MAPI homojunction as absorbing layer showed improved fill factors and photovoltages compared to a similar device with an intrinsic perovskite absorber layer. This work represents a proof-of-principle for the development of novel perovskite optoelectronic devices using perovskite-perovskite hetero and homo-junctions which can further improve the charge separation and reduce charge recombination.

A second goal was to reduce the trap density in perovskite LEDs as these are the main source of efficiency losses. By studying the excitation density dependence of the photoluminescence lifetime, a large concentration of trap

states was deduced for MAPI films prepared with stoichiometric amounts of the pre-cursors. The same films led to a low luminescence efficiency when employed in planar LEDs. By changing the MAI/PbI_2 precursors-ratios it was possible to increase the PL intensity of the perovskite layers substantially. The use of an excess MAI led to the passivating of traps in the MAPI films. Most importantly we were able to prepare perovskite LEDs with EQEs that were orders of magnitude higher than the reference LED. The data presented in this thesis are an important step towards the development of fully vacuum-deposited perovskite LEDs where the reduction of traps guarantees and efficient electro-luminescence.

The aim of the chapter "Influence of hole transport material (HTMs) ionization energy on performance of perovskite solar cells" was to untangle the factors influencing the V_{oc} in perovskite solar cells. A series of perovskite solar cells in which different HTMs with difference ionization potentials were employed as the hole transport layers.. This series of devices showed differences in V_{oc}`s of around 60 mV, which is a rather small difference in view of the larger differences in ionization potentials of the HTMs. By extracting the ideality factors from the dark JV-curves allowed to assign the differences in $V_{oc}$`s to different charge recombination paths. Furthermore, the results demonstrated that efficient charge extraction is possible even in a device that contains a HTMs that has a energy difference between its ionization potential and the perovskite valence band. These results point towards HTM designing routes which can improve the performance of perovskite solar cells, focusing on the interfacial recombination reduction rather than on the energetic alignment.

8 Resumen en castellano

Introducción

Perovskitas híbridas para células solares de tercera generación y dispositivos emisores de luz

La energía es crucial para las sociedades modernas y para el desarrollo socioeconómico de las futuras generaciones. En la actualidad, dependemos en gran medida de las fuentes de energía fósiles, que emiten gases de efecto invernadero y contribuyen al cambio climático, causando además conflictos geopolíticos y militares. Por todo ello, es necesario el desarrollo de nuevas fuentes de energía renovables, entre las cuales destaca la fotovoltaica. Las células solares basadas en silicio dominan el mercado fotovoltaico desde hace décadas, pero los altos costes de producción, transporte e instalación limitan su difusión a mayor escala y en aplicaciones donde se requiera flexibilidad y menor peso.

Se han realizado muchos estudios para desarrollar nuevas tecnologías fotovoltaicas que superen estas limitaciones. Así pues, la tercera generación de energía fotovoltaica utiliza materiales abundantes y fáciles de procesar, que permitirían una producción a gran escala reduciendo así el coste total de energía.

Por otro lado, el conocimiento obtenido en ese proceso de desarrollo de la energía fotovoltaica puede utilizarse también para desarrollar diodos emisores de luz (LED), utilizando los mismos materiales. La obtención de nuevas fuentes de luz más eficientes es un reto asimismo importante, ya que la iluminación consume aproximadamente el 20 % de la producción total de electricidad a escala global.

Uno de los materiales que pueden potencialmente dar respuesta a esta necesidad de proporcionar una fuente de energía renovable y al mismo tiempo una forma eficiente de iluminación son las perovskitas de haluros metálicos, compuestos semiconductores que pueden implementarse tanto en células solares como en LEDs.

Relación entre propiedades y estructura de capas delgadas de perovskita

La perovskita se define por una estructura general ABX_3, donde *X* es un anión y *A* y *B* son cationes de diferentes tamaños y carga. La estabilidad cristalográfica de una estructura de perovskita se puede estimar mediante el factor de tolerancia (*t*) y el factor octaédrico (μ), donde *t* se define como la relación entre las distancias *A-X* y la distancia *B-X*, que a su vez dependen de los radios iónicos. Simplificando las especies atómicas con un modelo de esfera sólida perfecta, *t* y μ se definen como:

$$\frac{r_{A+}r_X}{\sqrt{2(r_{B+}r_X)}}$$

$$\mu = \frac{R_B}{R_X}$$

R_A, R_B y R_X son los radios iónicos de los cationes y aniones. Para una perovskita de haluro con X = F, Cl, Br, I se obtendría una estructura estable cuando $0.81 < t < 1.11$ y $0.44 < u < 0.90$.

Las perovskitas híbridas (con cationes orgánicos) muestran características importantes para aplicaciones en diodos emisores de luz y capas absorbentes en células solares de capa delgada. Los LEDs basados en perovskita presentan un ancho de banda de emisión estrecho, que resulta en una alta pureza de color. Además, la banda de emisión puede sintonizarse en todo el espectro visible intercambiando los haluros. Por ejemplo, la perovskita de haluro de plomo y metilamonio $MAPbX_3$ con X = Cl−, X = Br−, o X = I− tiene bandas prohibidas de aproximadamente 3.1 eV, 2.3 eV y 1.6 eV, respectivamente. Se puede ajustar aún más la banda prohibida y por tanto la emisión simplemente mezclando los haluros en diferentes proporciones. Las perovskitas de banda ancha que contienen Br- y Cl- se han usado predominantemente en LEDs, ya que emiten en el espectro visible y son caracterizadas por altas energías de enlace excitónico. En contraste, el MAPI

tiene excelentes propiedades para aplicaciones fotovoltaicas, entre las cuales hay que destacar:

- Alto coeficiente de absorción
- Baja energía de enlace de los excitones
- Movilidad de electrones y huecos balanceada
- Gran longitud de difusión de las cargas

Sin embargo, no todas las propiedades de la perovskita son beneficiosas. Hace ya décadas que los científicos descubrieron que las cargas electrónicas no son la única especie móvil en la perovskita. La presencia de iones móviles complica la caracterización de estos dispositivos y puede comprometer su estabilidad. De hecho, los cálculos de las energías de activación y medidas de la migración iónica han revelado que los defectos de haluros vacantes e intersticiales son las especies más móviles en la estructura de la perovskita.

Otra característica de la perovskita es que su estructura y su morfología afectan enormemente el rendimiento global del dispositivo. Así pues, el mismo compuesto de perovskita puede tener diferentes propiedades dependiendo de las técnicas y condiciones de deposición. Esta deposición de perovskita es un proceso muy delicado e influye profundamente en la cristalinidad, tamaño y borde de grano. Los parámetros morfológicos más importantes son el tamaño y la forma de los granos, así como su orientación y empaquetamiento. La importancia de los bordes de grano se puede apreciar mediante medidas de mapas de fotoluminiscencia (PL), observando como la intensidad de emisión es mayor en el grano y disminuye hacia los bordes, que aparecen oscuros. Esto indica un aumento de la recombinación no-radiativa en los bordes de grano, debido a la presencia de trampas electrónicas. Por lo tanto, no es sorprendente que las perovskitas con granos grandes muestren típicamente una alta eficiencia de los dispositivos. Sin embargo, las capas de perovskita co-evaporadas se consideran una excepción ya que, a pesar de ser caracterizadas por un tamaño de grano mucho menor (< 100 nm), presentan también una elevada eficiencia y por tanto pueden utilizarse para la preparación de células solares de alta eficiencia.

Procesos básicos de operación de células solares y dispositivos emisores de luz de perovskitas.

Cuando una capa de perovskita absorbe un fotón, se genera un par electrón-hueco que, gracias a que la energía de enlace excitónica es baja, da lugar a la formación de cargas libres a temperatura ambiente. Estas cargas necesitan llegar a las capas de transporte selectivo (de huecos y electrones) y ser extraídas antes de que puedan recombinarse. La eficiencia de extracción de carga a las capas de transporte depende en buena medida de la movilidad de carga de la perovskita. Como se ha mencionado anteriormente, los electrones y huecos en las perovskitas tienen masas efectivas muy bajas que resultan en longitudes de difusión que pueden superar el micrómetro.

Otro factor a tener en cuenta es la recombinación de carga, que compite con la extracción, y que puede ser radiativa o no radiativa. En los dispositivos optoelectrónicos existen tres tipos diferentes de recombinación. La recombinación radiativa directa implica la recombinación de un electrón en la banda de conducción con un hueco en la banda de valencia, mediante generación de un fotón con energía igual a la separación entre bandas. Esta recombinación denominada de tipo bimolecular es relativamente baja en el régimen de funcionamiento normal de las células solares. Por otro lado, la recombinación no radiativa (sin emisión de fotones) puede tener un impacto significativo en el rendimiento del dispositivo incluso a iluminación baja. Este tipo de recombinación esta mediada por estados electrónicos asociados a defectos estructurales en el material, como los que caracterizan la superficie y los bordes del grano. El tercer tipo de recombinación se denomina Auger y es también de tipo no radiativo. En los procesos Auger, un electrón y un hueco se recombinan y transfieren su energía y momento a otro electrón. Este tipo de recombinación solo ocurre con iluminación muy intensa, por lo que no es muy relevante para el funcionamiento de las células solares de perovskita.

La eficiencia de conversión de potencia de una célula solar se evalúa mediante medidas eléctricas de corriente y voltaje, llamadas características JV. Simplemente se mide la corriente generada en función de la tensión aplicada bajo iluminación, utilizando un simulador solar calibrado. La

corriente de las células solares se describe mediante la ecuación clásica del diodo, formulada por Shockley. De las características JV pueden extraerse varios parámetros fundamentales:

• Densidad de corriente de cortocircuito (J_{SC}, mA cm^{-2})

• Voltaje en circuito abierto (V_{oc}, V)

• Factor de llenado (FF, %)

• Eficiencia de conversión de potencia (PCE, %)

Los dispositivos emisores de luz funcionan de manera muy similar a las células solares. De hecho, cuando se aplica un voltaje suficientemente alto a una célula solar, es posible inyectar portadores de carga que recombinan emitiendo fotones. Los parámetros más comúnmente utilizados para analizar los LEDs son:

• Luminancia (cd/m^2)

• Densidad de corriente (A/m^2)

• Eficiencia de corriente (cd/A)

• Eficiencia energética (lm/W)

• Eficiencia cuántica externa (EQE_{EL}, %)

Objetivo de la tesis

Los dispositivos fotovoltaicos y emisores de luz basados en perovskita se han desarrollado muy rápidamente en los últimos años. A pesar del rápido progreso, la gran mayoría de estudios se basa en un enfoque empírico con el fin de impulsar aún más la eficiencia del dispositivo. El objetivo de la tesis ha sido, por lo tanto, profundizar en los procesos fotofísicos fundamentales tanto en las células solares como en los LEDs de perovskita. El trabajo ha sido estructurado en tres partes:

• Homounión p-n de perovskita obtenida mediante modificación de la estequiometría

Una de las propiedades más importantes de los semiconductores es la posibilidad de controlar sus propiedades electrónicas a través de la introducción controlada de impurezas (dopado). Sin embargo, el dopado en la perovskita sigue estando casi inexplorado y nunca se han demostrado uniones p-n de perovskita. En este capítulo se presenta un proceso de dopado de perovskita y su aplicación en la preparación de una homounión p-n.

• Foto y electroluminiscencia eficientes mediante pasivación de defectos en perovskitas híbridas depositadas en vacío

Los estados electrónicos asociados a defectos estructurales (trampas electrónicas) son los mayores responsables de las pérdidas de eficiencia en los LED de perovskita. En este capítulo presentamos una estrategia para pasivar estos defectos mediante alteración de la estequiometría de la perovskita. Las capas así producidas aumentan la eficiencia general del dispositivo en órdenes de magnitud.

• Influencia de la energía de ionización del material transportador de huecos en el rendimiento de las células solares de perovskita

El voltaje de circuito abierto (V_{oc}) es un parámetro determinante para la eficiencia global de una célula solar. En este capítulo se han preparado células solares de perovskita variando de manera sistemática la energía de ionización de la capa de transporte de huecos. Pudimos demostrar que el V_{oc} se determina únicamente por la naturaleza de la recombinación de carga en el volumen y en la superficie de la perovskita y no por los niveles energéticos de las capas de transporte.

Métodos experimentales

Los dispositivos presentados en esta tesis fueron preparados exclusivamente por métodos de deposición en vacío. Las técnicas de deposición en vacío son ampliamente utilizadas en la industria de semiconductores, lo cual facilitaría la transferencia de conocimientos desde la investigación académica a la

industria. Además, las técnicas de deposición en vacío tienen una serie de ventajas importantes sobre los métodos basados en disolución.

• Fabricación independiente del substrato

• Alta pureza de los precursores

• Control exacto del espesor de la capa

• Proceso intrínsecamente aditivo

Las perovskitas pueden ser materiales complejos, formados a partir de múltiples precursores. El inconveniente de los métodos basados en disolución es que todos los precursores deben ser solubles en el mismo disolvente. En contraste, en la deposición en vacío no existen problemas de solubilidad y se pueden preparar capas de perovskitas a partir de una multitud de precursores. La deposición en vacío de doble fuente es el método elegido para el desarrollo de esta tesis. En el proceso de co-deposición, los dos precursores de perovskita PbI_2 y MAI se calientan simultáneamente en unos crisoles instalados en la base una cámara de alto vacío. En la parte superior de la cámara se monta un soporte para los sustratos, lo que permite que los precursores se condensen en dicho sustrato y reaccionen directamente dando lugar a la perovskita sin necesidad de ningún tratamiento térmico adicional. La estequiometría de la perovskita puede ajustarse cambiando las velocidades de evaporación relativa de los compuestos. La velocidad de evaporación se lee en tiempo real utilizando microbalanzas basadas en cristales de cuarzo.

Homounión de perovskita obtenida mediante dopado compositivo

La electrónica moderna comprende un amplio espectro de componentes y dispositivos la mayoría de los cuales se basan en materiales semiconductores. Uno de los aspectos más importantes de los semiconductores es la posibilidad de modular sus propiedades electrónicas a través del dopado. La introducción selectiva de impurezas que alteran la estequiometría del material permite controlar el tipo (electrón, hueco) y la concentración de los portadores de carga, obteniendo semiconductores de

tipo n o tipo p. De particular importancia para varias aplicaciones es la interfaz entre semiconductores con dopado contrario, la unión p−n. Los principios físicos de las uniones p-n han sido estudiados durante décadas, llevando al desarrollo de las primeras células solares eficientes basadas en semiconductores inorgánicos convencionales. Las perovskitas híbridas, como el yoduro de plomo y metilamonio ($CH_3NH_3PbI_3$, MAPI) tienen el potencial de transformar radicalmente la forma en que se concibe la optoelectrónica, combinando las propiedades favorables de los compuestos orgánicos e inorgánicos dentro de un solo material. Así pues, este tipo de perovskitas está entre los materiales fotovoltaicos más prometedores, gracias a sus eficiencias de conversión de potencia (PCE) en continua evolución y que ya superan el 22%. A pesar de este rápido desarrollo, el dopado extrínseco de las perovskitas permanece hasta ahora casi inexplorado, y las homouniones de perovskita solo se han obtenido en estructuras planas mediante el uso de sustratos de diferentes características electrónicas. De hecho, cuando se incorporan metales de otra naturaleza y carga en la estructura de perovskita, se producen distorsiones de la red cristalina que enmascaran el efecto de los dopantes, haciendo que las perovskitas sean poco sensibles a la inserción de otras especies metálicas. Además, el tipo de sustrato utilizado para el crecimiento de capas delgadas de perovskita tiene un efecto directo sobre sus bandas de energía y en particular sobre la posición del nivel de Fermi, complicando aún más el desarrollo de compuestos dopados. Teniendo en cuenta estas dificultades, se han explorado otras estrategias para obtener capas dopadas de perovskita. Por ejemplo, se ha observado como la perovskita MAPI puede ser dopada de tipo p mediante exposición a vapores de yodo. Una alternativa atractiva y peculiar es el dopado obtenido mediante defectos estequiométricos, por el cual capas de MAPI ricas en MAI son de tipo p, mientras que los compuestos deficientes en MAI son de tipo n. El desequilibrio en la relación molar entre los precursores causa defectos en el retículo cristalino que induce estados electrónicos próximos a los bordes de la bandas de energía, mientras que no se producen estados profundos dentro de la banda prohibida como se esperaría para semiconductores convencionales. Este efecto es una consecuencia de las pequeñas masas efectivas de electrones y huecos y de la alta constante dieléctrica de la

perovskita. En general, la mayoría de los estudios sobre las propiedades electrónicas y ópticas de las perovskitas se llevan a cabo en materiales depositados desde disolución. A pesar del alto nivel de control sobre la morfología de la perovskita obtenido mediante puesta a punto de las condiciones de deposición, no es posible preparar completamente por disolución una doble capa de perovskita, debido a la inevitable redisolución de la capa subyacente. Para este propósito, la deposición en vacío es una técnica más adecuada porque es intrínsecamente aditiva y además puede conducir a materiales de igual rendimiento y calidad.

Sección experimental

Se obtuvieron capas de perovskita dopadas mediante coevaporación en alto vacío cambiando sistemáticamente la relación molar entre MAI y PbI_2. La homounión de perovskita se obtuvo depositando una capa de MAPI tipo n (n-MAPI) sobre otra de tipo p (p-MAPI). En el proceso de coevaporación, se ha modificado la estequiometria de los precursores cambiando la velocidad de evaporación de PbI_2 y manteniendo constante la velocidad de evaporación de MAI. Las velocidades de deposición se controlan mediante sensores calibrados de cuarzo durante el proceso de evaporación. Las capas de perovskita se depositaron entre semiconductores orgánicos utilizados como materiales selectivos de transporte de carga. Los contactos selectivos utilizados consisten en capas dobles, formadas por una capa dopada (40 nm) y una capa intrínseca más delgada (10 nm) en contacto con la perovskita. Las capas de transporte de electrones y huecos (ETL, HTL) consistían en fullereno (C60) y N4,N4,N4'',N4''-tetra([1,1'-bifenil]-4-il)-[1,1':4',1'-terfenil]-4,4'-diamina (TaTm), mientras que los dopantes empleados son el N1,N4-bis(trip-tolylphosphoranylidene) benzene-1,4-diamine (PhIm) y el 2,2'-(perfluoronaftaleno-2,6-diylideno)-dimalononitrilo (F_6-TCNNQ), respectivamente. Los espesores y las concentraciones de dopado fueron optimizados previamente. Todas las capas del dispositivo se han depositado por sublimación en alto vacío encima de un electrodo transparente de ITO y usando Ag como contacto reflectante.

Resultados y discusión

La estequiometria de las capas de perovskita se ha determinado mediante espectroscopia infrarroja, que permite cuantificar el contenido de metilamonio. Analizamos la unión de perovskita usando una sonda Kelvin basada en un microscopio de fuerza atómica (del inglés, *scanning Kelvin probe microscope*, SKPM). Primero medimos la diferencia del potencial de los contactos en una célula solar de referencia de MAPI intrínseco (i-MAPI). Para un dispositivo de este tipo, encontramos una caída de potencial relativamente constante a lo largo del grosor del dispositivo, como es de esperar para un diodo de tipo p-i-n. En contraste, para la célula solar formada por la homounión de perovskita, observamos una variación abrupta del potencial en la interfaz entre las capas de p-MAPI y n-MAPI. Esta variación, de aproximadamente 250 mV, se mantuvo estable durante varias horas. Los mismos dispositivos se caracterizaron como células solares midiendo su respuesta espectral y las características eléctricas bajo iluminación. Las células preparadas con i-MAPI y p-MAPI mostraron espectros de EQE comparables. Las características de densidad de corriente en función del voltaje (J − V) bajo iluminación y en la oscuridad para las células intrínsecas y p-MAPI también resultaron ser similares. Se observó solamente una pequeña reducción en el voltaje de circuito abierto (V_{oc}) de 1059 a 1027 mV, que podría estar relacionada con una diferencia en el nivel de Fermi de los dos materiales. Sin embargo, el rendimiento del dispositivo fue muy inferior cuando se implementó la perovskita n-MAPI en un dispositivo. Debido a una reducida densidad óptica, el espectro de EQE resultó ser muy bajo, resultando en una J_{sc} de solo 6.4 mA cm^{-2}. El menor contenido de MAI da como resultado un exceso de PbI_2 en la capa, lo que dificulta tanto la generación de los portadores de cargas como su separación y transporte. Las características J-V mostraron un FF de tan solo 54.4%, lo cual confirma la presencia de problemas en la inyección y transporte de carga. Por otro lado, se observó un V_{oc} relativamente alto (1072 mV), lo que implica que la recombinación de carga no radiativa no es el proceso principal que limita la extracción de cargas en este dispositivo. El diodo basado en la homounión de perovskita tenía un rendimiento notable, con una buena rectificación. En particular, el V_{oc} (1095 mV) y el FF (∼80%) mejoraron sustancialmente en

comparación con los otros dispositivos, a pesar de que la eficiencia resultante fuese aún inferior en comparación con las células de referencia con MAPI estequiométrico.

En resumen, reportamos por primera vez la fabricación de una homounión de perovskita obtenida por codeposición en vacío de MAPI. Este trabajo representa una prueba de concepto para el desarrollo de dispositivos optoelectrónicos de perovskita, que podrían beneficiarse del uso de homo o heterouniones para mejorar aún más la separación de la carga y minimizar la recombinación.

Foto- y electroluminiscencia eficiente mediante pasivación de defectos en capas delgadas de perovskita híbrida depositadas en vacío.

Las perovskitas de haluro de plomo híbridas son semiconductores con potenciales aplicaciones en diodos emisores de luz (LED), ya que podrían cumplir los requisitos para desarrollar fuentes de luz económicas y a la vez eficientes. El bajo coste de los precursores y la posibilidad de un procesado simple y a baja temperatura las convierten en prometedoras competidoras de los semiconductores cristalinos inorgánicos, que requieren métodos de fabricación complejos y de alta temperatura. Los LEDs híbridos de perovskita de haluro de plomo muestran un ancho de banda de emisión muy estrecho, lo que conlleva una alta pureza del color, y pueden emitir en todo el espectro visible mediante modificaciones de la composición de la perovskita. El tipo de haluro empleado en la perovskita tiene el efecto más importante en la determinación de la banda prohibida. En particular, las perovskitas de haluro de plomo y metilamonio del tipo $MAPbX_3$ con $X = Cl^-$, Br^- o $X = I^-$ tienen bandas prohibidas de aproximadamente 3.1 eV, 2.3 eV y 1.6 eV, respectivamente. La banda puede ajustarse a energías intermedias mezclando los haluros en proporciones adecuadas. El desarrollo de LEDs de perovskita se ha centrado principalmente en las perovskitas con banda prohibida ancha (las que contienen Cl^- y Br^-), ya que emiten en el rango visible del espectro y muestran altas energías de enlace excitónico. Por otro lado, la perovskita de yodo MAPI tiene propiedades excelentes para aplicaciones fotovoltaicas, como la gran longitud de difusión de los portadores de cargas, una movilidad de electrones y huecos equilibrada, una baja densidad de defectos y la fotogeneración de portadoras de carga libres a temperatura ambiente. Esta última propiedad deriva de la baja energía de enlace de los excitones, de entre 2 y 60 meV, lo cual es beneficioso para células solares pero no necesariamente para aplicaciones en LEDs. Además, la mayoría de las perovskitas de tipo MAPI muestran un PLQY bajo, debido a que la recombinación monomolecular por defectos domina los procesos de recombinación, sobre todo a concentraciones bajas de portadores. Esto significa que, a baja densidad de corriente, los LEDs de perovskita basados

en MAPI policristalino son poco eficientes. Las estrategias para obviar esta limitación implican el uso de estructuras de perovskita cuasi-2D, o el uso de capas delgadas de perovskita nanoestructuradas. Una forma alternativa de mejorar la fotoluminiscencia de las perovskitas es el uso de un exceso de metilamonio. En el $MAPbBr_3$ procesado por disolución, una relación molar de $MABr/PbBr_2 > 3$ lleva a la formación de nanocristales incorporados en una matriz rica en MABr, lo que aumenta la PLQY. En las capas de MAPI, un exceso de MAI conduce a un aumento de la intensidad y del tiempo de vida medio de la fotoluminiscencia, debido a la pasivación de los defectos vacantes de haluros. En los primeros estudios sobre capas delgadas de MAPI depositadas en vacío se utilizaba también un exceso de MAI, sin embargo, para fomentar la formación de la perovskita, las capas se sometían a un tratamiento térmico eliminando el exceso de catión. Por lo tanto, el efecto del exceso de MAI en capas de perovskita depositadas en vacío sobre las propiedades luminiscentes de los materiales nunca se ha investigado anteriormente.

Sección experimental

Las capas de MAPI se prepararon optimizando la relación molar de los precursores de MAI y PbI_2. La estequiometria de estos componentes se ajustó cambiando la velocidad de deposición de PbI_2 mientras se mantenía la ratio de MAI fijo durante el proceso de deposición. Se depositaron tres tipos de perovskita diferentes con relación molar MAI:PbI_2 de 1:1, 3:1 y 6:1. La serie de compuestos se empleó como capa emisora en diodos emisores de luz, utilizando semiconductores orgánicos como materiales de transporte de carga. La capa emisora consistía en una perovskita de 320 nm de grosor, depositada entre capas selectivas de transporte de huecos y electrones de 10 nm de espesor, denominadas HTL y ETL, respectivamente. La HTL consistía en un derivado de arilamina, N4, N4, N4 ", N4" -tetra ([1,1´-bifenil] -4-il) -[1,1´: 4´, 1 '' --fenilo] -4,4 ”-diamina (TaTm) y la ETL en el fullereno C60. Entre los electrodos y las capas intrínsecas de transporte, depositamos capas de 40 nm de espesor con los mismos materiales pero dopados para mejorar la conductividad y, por lo tanto, la inyección de carga. Para el TaTm utilizamos 2,20- (perfluoronaftaleno-2,6-diilideno) dimalononitrilo (F_6-TCNNQ) como dopante orgánico, mientras que para el C60 se usó N1,N4-bis(tri-p-

tolilfosforanilideno)-benceno-1,4-diamina (PhIm). Los dispositivos se fabricaron enteramente por deposición en vacío en una configuración de tipo n-i-p usando ITO y oro como electrodos transparente y reflectante, respectivamente.

Resultados y discusión

El patrón de difracción de rayos-X en ángulo rasante (GIXRD) confirma la formación de capas delgadas de MAPI con alta cristalinidad para la perovskita estequiométrica, y menor cristalinidad para capas de MAPI producidas con exceso de MAI. Las capas de MAPI estequiométricas mostraban la absorción óptica característica a 780 nm y una absorbancia intensa en todo el espectro visible. Por otro lado, los espectros de absorción óptica de las capas de perovskita producidas con exceso de MAI mostraban una absorbancia mucho menos intensa. Es interesante evidenciar que, al exponerlas al aire, el espectro de absorción de las perovskitas de composición MAI:PbI_2 3:1 evolucionaba progresivamente hasta mostrar la transición característica a 780 nm y estabilizándose después de aproximadamente 30 minutos. El efecto de la atmósfera en el crecimiento y la estabilidad de la perovskita ha sido investigado previamente. Si bien una exposición prolongada de las capas de perovskita al aire generalmente conduce a su degradación y, por lo tanto, a dispositivos de bajo rendimiento, una exposición controlada durante el procesamiento del material puede ser beneficiosa. Los haluros de metilamonio son muy higroscópicos, lo cual favorece la penetración de agua en la capa de perovskita. El agua vuelve a disolver parcialmente los cationes orgánicos, permitiendo una reorganización del material y promoviendo su recristalización. Este es probablemente el mecanismo responsable de la evolución del espectro de absorción observado en nuestros sistemas, en vista del alto contenido de MAI utilizado en las capas de perovskita.

El tiempo de vida de fotoluminiscencia de las capas de perovskita con diferentes estequiométricas se ha analizado con una función monoexponencial, en el caso de la perovskita estequiométrica, o mediante una doble exponencial para las muestras con exceso de MAI. La perovskita estequiométrica muestra un tiempo medio de vida corto de $\tau_1 = 5.7$ ns, que aumenta al alterar la estequiometría. En particular, el tiempo de vida medio

para las capas con MAI:PbI_2 6:1 es ligeramente más largo, $\langle\tau\rangle = 13.5$ ns (τ_1 = 3.3 ns, τ_2 = 26 ns), mientras que aumenta sustancialmente para las capas que se produjeron con relación molar MAI:PbI_2 3:1, hasta $\langle\tau\rangle = 34.4$ ns (τ_1 = 13.7 ns, τ_2 = 47 ns), contribuyendo así al aumento de la PLQY.

Los dispositivos se caracterizaron midiendo la densidad de corriente y la intensidad de electroluminiscencia en función del voltaje. En general, observamos una corriente de fuga baja, lo que indica una buena calidad a nivel morfológico de los diodos de perovskita. La densidad de corriente comienza a aumentar por encima de 0.5 V y su tendencia es inversamente proporcional a la cantidad de MAI incorporada en la capa activa. Esto podría esperarse considerando la mayor cantidad de material amorfo y la reducida cristalinidad de capas con exceso de MAI, como también se observó por XRD y SEM. La electroluminiscencia se detecta a voltajes bajos, alrededor de 1.1 V, para los diodos con perovskita estequiométrica y con MAI:PbI_2 3:1, mientras que el voltaje aumenta ligeramente (> 1.3 V) para la perovskita con MAI:PbI_2 6:1. Es importante destacar que la electroluminiscencia más intensa (4.1 $W{\cdot}Sr^{-1}{\cdot}m^{-2}$) se observó para los LEDs basados en la perovskita no estequiométrica con MAI:PbI_2 3:1, dos órdenes de magnitud más elevada que para el dispositivo con MAPI estequiométrico ($2.3 \cdot 10^{-2}$ W · $W{\cdot}Sr^{-1}{\cdot}m^{-2}$). El EQE asociado es de 1.92% para MAI:PbI_2 3:1, mientras el valor máximo para los LEDs con MAPI estequiométrica es de 0.05%. El LED con el mayor exceso de MAI mostró una electroluminiscencia (máximo a 1.2 $W{\cdot}Sr^{-1}{\cdot}m^{-2}$) y EQE (0.67%) mejorados, a pesar de la menor densidad de corriente. Los valores de EQE registrados para la serie de LED siguen la tendencia del tiempo de vida y de la intensidad de fotoluminiscencia de las capas de perovskita, como se describió anteriormente.

Con el fin de entender el origen de las propiedades ópticas y optoelectrónicas de las muestras de MAPI no estequiométricas, estudiamos su dinámica de fotoluminiscencia en función de la densidad de excitación. Para la perovskita estequiométrica, el tiempo de vida medio se vuelve inicialmente más lento cuando se aumenta la densidad de excitación. Este comportamiento se ha observado en estudios anteriores y se ha atribuido al llenado de niveles electrónicos asociados a defectos. Al aumentar aún más la densidad de

excitación, la dinámica de fotoluminiscencia se hace más rápida, debido a los procesos de recombinación de orden superior. Por otro lado, la dinámica de fotoluminiscencia de las muestras que contienen un exceso de MAI muestra una tendencia diferente en comparación con la perovskita estequiométrica. Sus tiempos de vida se vuelven sistemáticamente más cortos al aumentar la densidad de excitación, lo que indica que los defectos electrónicos no interfieren en la recombinación en este régimen de excitación. Por lo tanto, el exceso de MAI pasiva eficientemente los defectos, reduciendo su concentración en comparación con el MAPI estequiométrico. Es importante destacar que el tiempo de vida medio más largo y la menor concentración de defectos son acordes con la tendencia observada en el EQE de los dispositivos.

En resumen, estudiamos el efecto del exceso de yoduro de metilamonio (MAI) en la preparación de capas delgadas de yoduro de plomo y metilamonio (MAPI) depositadas en vacío. El exceso de MAI en capas evaporadas es capaz de pasivar eficientemente sus defectos, en analogía a lo que se observó para capas MAPI procesadas por disolución. Es importante destacar que pudimos preparar diodos emisores de luz con una eficiencia cuántica externa cercana al 2%. Este valor es casi dos órdenes de magnitud más alto en comparación con los LEDs de referencia que emplean el MAPI estequiométrico. Los datos presentados aquí son prometedores para el desarrollo de LEDs de perovskita eficientes depositados en vacío, donde el control sobre los defectos es esencial para garantizar una electroluminiscencia eficiente.

Influencia de la energía de ionización del material transportador de huecos en el rendimiento de las células solares de perovskita.

Las células solares de perovskita son una de las alternativas más interesantes entre las tecnologías fotovoltaicas actuales. Sin embargo, y a pesar de los numerosos estudios sobre los procesos de recombinación de los portadores de carga, todavía existe debate sobre los factores que afectan al potencial de circuito abierto (V_{oc}) de los dispositivos. En general, la separación de los quasi-niveles de Fermi para electrones y huecos define el máximo V_{oc} obtenible para un determinado semiconductor, y están determinados por el balance entre la generación y recombinación de portadores de cargas en el material.

En las células solares de perovskita, el problema se amplía hacia el rol de las capas selectivas de transporte y su contribución al V_{oc} final. Algunas publicaciones han relacionado la magnitud del voltaje con la diferencia de energía entre los orbitales moleculares ocupados más altos (HOMO) del material de transporte de huecos (HTM) y los orbitales moleculares no ocupados más bajos (LUMO) del material de transporte de electrones (ETM), siempre que haya proximidad entre estos niveles de energía y las bandas de valencia y de conducción de la perovskita. Aunque algunos trabajos muestran un aumento del V_{oc} para HTMs con mayor energía de ionización (IE), esta tendencia no se ve reflejada en el rendimiento de las células solares más eficientes, donde se han reportado mejores Voc tanto para HTMs con HOMO alto (baja IE) como con bajo (alta IE), independientemente de la alineación entre niveles energéticos.

Sin embargo, en todos los trabajos presentados, el HOMO del HTM empleado tenía una energía cercana o menor respecto al máximo de la banda de valencia de la perovskita. Un análisis sistemático del efecto de una serie de HTMs con diferentes energías de HOMO sería adecuado para investigar su relación con el V_{oc}. Sin embargo, es importante tener en cuenta que la sustitución del HTM puede afectar a la recombinación de carga interfacial, que tiene un gran impacto sobre el V_{oc}. Cabe destacar como la gran mayoría de los estudios sufren las limitaciones asociadas a las células solares procesadas por disolución. La más importante es el efecto del HTM en la

morfología de la perovskita en configuración p-i-n (la perovskita se deposita por disolución sobre el HTM), ya que diferentes morfologías conllevarían diferentes densidades de defectos. Además, la mayoría de los estudios se han llevado a cabo en células solares de tipo n-i-p, donde la densidad de portadores de carga es más alta en la interfaz ETM/perovskita, lo que podría reducir el efecto del HTM y subestimar así su impacto en el V_{oc}. En este sentido, las perovskitas depositadas en vacío tienen importantes ventajas, como la morfología débilmente dependiente del sustrato y la posibilidad de depositar cualquier HTM o ETM en el orden y grosor deseado.

Sección experimental

Los materiales transportadores de huecos utilizados son el 4,4',4''-Tris[fenil(m-tolil)amino]trifenilamina (m-MTDATA), el N4,N4,N4'',N4''-tetra([1,1'-bifenil]-4-il)-[1,1´:4´,1''-fenil]-4,4''-diamina (TaTm) y el Tris (4-carbamoil-9-ilfenil)amina (TcTa)). Sus energías de ionización de 5.02 eV, 5.38 eV y 5.68 eV, respectivamente, se midieron utilizando espectroscopia fotoelectrónica en aire. Las células solares se fabricaron siguiendo una arquitectura de tipo p-i-n que consiste en vidrio con ITO, MoO_3, HTM, MAPI, fullereno (C60), 2,9-Dimetil-4,7-difenil-1,10-fenantrolina (BCP) y Ag como contacto superior.

Resultados y discusión

Las características de voltaje y corriente se midieron bajo iluminación de 100 mW cm^{-2} en polarización directa e inversa. Curiosamente, los dispositivos con m-MTDATA y TcTa casi no muestran variación en el V_{oc} (1.008 V y 1.000 V), a pesar de tener una diferencia de IE de 0.66 eV entre los HTMs. Los dispositivos con TaTm muestran el V_{oc} más alto, 1060 mV. Dado que estos resultados no muestran una tendencia evidente entre la IE de los HTMs y el V_{oc} resultante, se llevaron a cabo estudios adicionales para elucidar la relación entre estos parámetros.

El tipo dominante de recombinación se investigó midiendo el V_{oc} en función de la intensidad de iluminación. El V_{oc} depende logarítmicamente de la intensidad de la luz y al introducir el factor de idealidad n_{ID} como factor previo, obtenemos:

$$eV_{oc} = E_g - n_{ID}k_BT\ ln\frac{I_0}{I}$$

E_g es la banda prohibida, T la temperatura, k_B la constante de Boltzmann y I_0 la corriente de saturación inversa. Midiendo el V_{oc} en función de la intensidad de la luz para dispositivos con HTM variables obtuvimos factores de idealidad de ∼1.7 para TaTm y ∼1.2 para TcTa y m-MTDATA. Cuando los factores de idealidad se aproximan a 1, la recombinación es directa y generalmente se

interpreta como una recombinación superficial no radiativa (si el V_{oc} asociado es bajo en comparación con la banda prohibida del semiconductor) o recombinación radiativa en el volumen del semiconductor (en el caso de V_{oc} elevados). Los factores de idealidad cercanos a 2 se asocian generalmente a la recombinación no radiativa mediada por defectos.

Estas consideraciones sugieren una recombinación superficial mayor que limita el V_{oc} en el caso de los dispositivos con TcTa y m-MTDATA, mientras que el V_{oc} en células con TaTm está limitado principalmente por la recombinación no radiativa mediada por defectos. El origen de la aumentada recombinación superficial en la interfaz entre MAPI y TcTa o m-MTDATA no está aún claro. Es poco probable que la IE del HTM influya en la separación de los quasi-niveles de Fermi, y en particular en la posición del quasi-nivel de Fermi de los huecos (E_{Fh}), que está determinado por la perovskita. Esto resulta de la baja energía de enlace del excitón y de la pequeña densidad de portadores de cargas en oscuridad del MAPI. Además, está en línea con observaciones anteriores donde las modificaciones de la energía de los HTMs y ETMs no afectan al fotovoltaje.

Por lo tanto, es importante discutir las implicaciones de los diferentes HTMs mediante los otros parámetros fotovoltaicos relevantes para los dispositivos. Las tres células solares difieren principalmente en FF, con TaTm y m-MTDATA con valores altos de alrededor de 75% y TcTa con un FF más bajo de 64%. Esto se puede atribuir a la mayor energía de ionización del TcTa, que también se refleja en la curva IV en oscuridad a voltajes de alrededor de 1 V. Todos los dispositivos alcanzan corrientes de cortocircuito relativamente altas, aproximadamente 20 mA/cm^2 para TaTm y 19 mA/cm^2 para TcTa y m-MTDATA. Las curvas de EQE son muy similares, lo que concuerda con los resultados analizados anteriormente. Este punto resalta la buena extracción de carga obtenida con TcTa y m-MTDATA a pesar de su desajuste de nivel de HOMO con la banda de valencia de la perovskita. Pudimos medir la cinética de extracción de carga mediante espectroscopia de absorción transitoria (TAS). Observamos una señal de reducción instantánea del GSB de la perovskita independientemente del HTM utilizado, lo que indica que la

inyección de huecos tiene lugar para todos los HTM a tiempos incluso menores que la resolución temporal del equipo (aproximadamente 60 fs).

En resumen, hemos fabricado una serie de dispositivos completamente evaporados basados en diferentes HTM con una diferencia de IE entre ellos de hasta 0.66 eV. Los dispositivos producidos con estos HTM mostraron voltajes de entre 1000 mV (TcTa, m-MTDATA) y 1060 mV (TaTm). La medición de los factores de idealidad nos permite explicar las diferencias en V_{OC} por los procesos de recombinación. Nuestros resultados indican que el Voc de las células solares de perovskita no está necesariamente limitado por la energía del material de transportador de huecos, sino principalmente por los diferentes caminos de recombinación de los portadores de carga. Además, mostramos una extracción de carga eficiente por HTM con HOMO desalineado con la perovskita (> 300 meV por encima y por debajo de la banda de valencia de la perovskita). Estos resultados ayudarán al diseño de nuevos HTMs que pueden mejorar el rendimiento de las células solares de perovskita.

9 Bibliography

1. Jäger-waldau A. *PV Status Report 2016*.; 2016. doi:10.2790/749737.

2. Chapin DM, Fuller CS, Pearson GL. A new silicon p-n junction photocell for converting solar radiation into electrical power [3]. *J Appl Phys*. 1954;25(5):676-677. doi:10.1063/1.1721711.

3. Tiwari GN, Kumar Mishra R. *Advanced Renewable Energy Sources*. The Royal Society of Chemistry; 2012.

4. Green MA, Hishikawa Y, Warta W, et al. Solar cell efficiency tables (version 50). *Prog Photovoltaics Res Appl*. 2017;25(7):668-676. doi:10.1002/pip.2909.

5. O'Regan B, Gratzel M. A Low-Cost, High-Efficiency Solar-Cell Based on Dye-Sensitized Colloidal TiO_2 Films. *Nature*. 1991;353(6346):737-740. doi:10.1038/353737a0.

6. Manser JS, Christians JA, Kamat P V. Intriguing Optoelectronic Properties of Metal Halide Perovskites. *Chem Rev*. 2016. http://pubs.acs.org/doi/abs/10.1021/acs.chemrev.6b00136. Accessed June 26, 2016.

7. Van Noorden R. Cheap solar cells tempt businesses. *Nature*. 2014;513(7519):470. doi:10.1038/513470a.

8. Waide P, Tanishima S. Light ' S Labour ' S Lost. 2006.

9. Li C, Lu X, Ding W, Feng L, Gao Y, Guo Z. Formability of ABX 3 (X = F, Cl,

Br, I) halide perovskites. *Acta Crystallogr Sect B Struct Sci*. 2008;64(6):702-707. doi:10.1107/S0108768108032734.

10. McKinnon NK, Reeves DC, Akabas MH. 5-HT3 receptor ion size selectivity is a property of the transmembrane channel, not the cytoplasmic vestibule portals. *J Gen Physiol*. 2011;138(4):453-466. doi:10.1085/jgp.201110686.

11. Cohen BN, Labarca C, Davidson N, Lester HA. Mutations in M2 alter the selectivity of the mouse nicotinic acetylcholine receptor for organic and alkali metal cations. *J Gen Physiol*. 1992;100(September):373-400. doi:10.1085/jgp.100.3.373.

12. Im J-H, Chung J, Kim S-J, Park N-G. Synthesis, structure, and photovoltaic property of a nanocrystalline 2H perovskite-type novel sensitizer (CH3CH2NH3)PbI3. *Nanoscale Res Lett*. 2012;7(1):353. doi:10.1186/1556-276X-7-353.

13. Koh TM, Fu K, Fang Y, Chen S, Sum TC, Mathews N. Formamidinium-Containing Metal-Halide: An Alternative Material for Near-IR Absorption Perovskite Solar Cells. 2013. doi:10.1021/jp411112k.

14. Pang S, Hu H, Zhang J, et al. NH2CH=NH2PbI3: An alternative organolead iodide perovskite sensitizer for mesoscopic solar cells. *Chem Mater*. 2014;26(3):1485-1491. doi:10.1021/cm404006p.

15. Green MA, Ho-Baillie A, Snaith HJ. The emergence of perovskite solar cells. *Nat Photonics*. 2014;8(7):506-514. doi:Doi 10.1038/Nphoton.2014.134.

16. Baikie T, Barrow NS, Fang Y, et al. A combined single crystal neutron/X-

ray diffraction and solid-state nuclear magnetic resonance study of the hybrid perovskites CH 3 NH 3 PbX 3 (X = I, Br and Cl). *J Mater Chem A*. 2015;3(17):9298-9307. http://pubs.rsc.org/en/content/articlehtml/2015/ta/c5ta01125f. Accessed June 26, 2015.

17. Kitazawa N, Watanabe Y, Nakamura Y. Optical properties of CH3NH3PbX3 (X = halogen) and their mixed-halide crystals. *J Mater Sci*. 2002;37(17):3585-3587. doi:10.1023/A:1016584519829.

18. Comin R, Walters G, Thibau ES, Voznyy O, Lu ZH, Sargent EH. Structural, optical, and electronic studies of wide-bandgap lead halide perovskites. *J Mater Chem C*. 2015;3(34):8839-8843. doi:10.1039/c5tc01718a.

19. Sessolo M, Gil-Escrig L, Longo G, Bolink HJ. Perovskite Luminescent Materials. *Top Curr Chem*. 2016;374(4). doi:10.1007/s41061-016-0051-1.

20. Miyata A, Mitioglu A, Plochocka P, et al. Direct measurement of the exciton binding energy and effective masses for charge carriers in organic–inorganic tri-halide perovskites. *Nat Phys*. 2015;11:582–587. doi:10.1038/nphys3357.

21. D'Innocenzo V, Grancini G, Alcocer MJP, et al. Excitons versus free charges in organo-lead tri-halide perovskites. *Nat Commun*. 2014;5:3586. doi:10.1038/ncomms4586.

22. Brivio F, Butler KT, Walsh A, Van Schilfgaarde M. Relativistic quasiparticle self-consistent electronic structure of hybrid halide

perovskite photovoltaic absorbers. *Phys Rev B*. 2014;89(15):155204. doi:10.1103/PhysRevB.89.155204.

23. Umari P, Mosconi E, De Angelis F. Relativistic GW calculations on CH3NH3PbI3 and CH3NH3SnI3 perovskites for solar cell applications. *Sci Rep*. 2014;4:4467. doi:10.1038/srep04467.

24. Hoke ET, Slotcavage DJ, Dohner ER, Bowring AR, Karunadasa HI, McGehee MD. Reversible photo-induced trap formation in mixed-halide hybrid perovskites for photovoltaics. *Chem Sci*. 2015;6(1):613-617. doi:10.1039/c4sc03141e.

25. Mizusaki J, Arai K, Fueki K. Ionic conduction of the perovskite-type halides. *Solid State Ionics*. 1983;11(3):203-211. doi:10.1016/0167-2738(83)90025-5.

26. Snaith HJ, Abate A, Ball JM, et al. Anomalous hysteresis in perovskite solar cells. *J Phys Chem Lett*. 2014;5(9):1511-1515. doi:10.1021/jz500113x.

27. de Quilettes DW, Vorpahl SM, Stranks SD, et al. Impact of microstructure on local carrier lifetime in perovskite solar cells. *Science (80-)*. 2015;348(6235):683-686. doi:10.1126/science.aaa5333.

28. Momblona C, Gil-Escrig L, Bandiello E, et al. Efficient vacuum deposited p-i-n and n-i-p perovskite solar cells employing doped charge transport layers. *Energy Environ Sci*. 2016;9(11):3456-3463. doi:10.1039/C6EE02100J.

29. Chung I, Lee B, He J, Chang RPH, Kanatzidis MG. All-solid-state dye-sensitized solar cells with high efficiency. *Nature*. 2012;485(7399):486-

489. doi:10.1038/nature11067.

30. Jiang CS, Yang M, Zhou Y, et al. Real-space distributions of electrical potential in planar and porous perovskite solar cells: Carrier separation and transport. *2015 IEEE 42nd Photovolt Spec Conf PVSC 2015*. 2015;6:1-10. doi:10.1109/PVSC.2015.7355618.

31. Edri E, Kirmayer S, Mukhopadhyay S, Gartsman K, Hodes G, Cahen D. Elucidating the charge carrier separation and working mechanism of CH3NH3PbI(3-x)Cl(x) perovskite solar cells. *Nat Commun*. 2014;5:3461. doi:10.1038/ncomms4461.

32. You J, Meng L, Hong Z, Li G, Yang Y. Inverted planar structure of perovskite solar cells. *Org Halide Perovskite Photovoltaics From Fundam to Device Archit*. 2016:307-324. doi:10.1007/978-3-319-35114-8_12.

33. DeQuilettes DW, Koch S, Burke S, et al. Photoluminescence Lifetimes Exceeding 8 μs and Quantum Yields Exceeding 30% in Hybrid Perovskite Thin Films by Ligand Passivation. *ACS Energy Lett*. 2016;1(2):438-444. doi:10.1021/acsenergylett.6b00236.

34. Brenner TM, Egger DA, Rappe AM, Kronik L, Hodes G, Cahen D. Are Mobilities in Hybrid Organic-Inorganic Halide Perovskites Actually “high”? *J Phys Chem Lett*. 2015;6(23):4754-4757. doi:10.1021/acs.jpclett.5b02390.

35. Brandt RE, Stevanovi?? V, Ginley DS, Buonassisi T. Identifying defect-tolerant semiconductors with high minority-carrier lifetimes: Beyond hybrid lead halide perovskites. *MRS Commun*. 2015;5(2):265-275.

doi:10.1557/mrc.2015.26.

36. Brenner TM, Egger DA, Kronik L, Hodes G, Cahen D. Hybrid organic—inorganic perovskites: low-cost semiconductors with intriguing charge-transport properties. *Nat Rev Mater*. 2016;1(1):15007. doi:10.1038/natrevmats.2015.7.

37. Wehrenfennig C, Eperon GE, Johnston MB, Snaith HJ, Herz LM. High charge carrier mobilities and lifetimes in organolead trihalide perovskites. *Adv Mater*. 2014;26(10):1584-1589. doi:10.1002/adma.201305172.

38. MK H, MD H. Performance Analysis of Intermediate Band Solar Cell (IBSC). *J Mater Sci Eng*. 2015;04(06). doi:10.4172/2169-0022.1000200.

39. Shi J, Xu X, Li D, Meng Q. Interfaces in perovskite solar cells. *Small*. 2015;11(21):2472-2486. doi:10.1002/smll.201403534.

40. Yoshikawa K, Kawasaki H, Yoshida W, et al. Silicon heterojunction solar cell with interdigitated back contacts for a photoconversion efficiency over 26%. *Nat Energy*. 2017;2(5). doi:10.1038/nenergy.2017.32.

41. No Title. https://www.nrel.gov/pv/assets/images/efficiency-c.

42. Yang WS, Park B-W, Jung EH, et al. Iodide management in formamidinium-lead-halide–based perovskite layers for efficient solar cells. *Science (80-)*. 2017;356(6345):1376-1379. doi:10.1126/science.aan2301.

43. Chen H, Ye F, Tang W, et al. A solvent-and vacuum-free route to large-area perovskite films for efficient solar modules. *Nature*. 2017;550(7674):92-95. doi:10.1038/nature23877.

44. Bi C, Chen B, Wei H, DeLuca S, Huang J. Efficient Flexible Solar Cell based on Composition-Tailored Hybrid Perovskite. *Adv Mater*. 2017;29(30):1-6. doi:10.1002/adma.201605900.

45. Uoyama H, Goushi K, Shizu K, Nomura H, Adachi C. Highly efficient organic light-emitting diodes from delayed fluorescence. *Nature*. 2012;492(7428):234-238. doi:10.1038/nature11687.

46. Reineke S, Lindner F, Schwartz G, et al. White organic light-emitting diodes with fluorescent tube efficiency. *Nature*. 2009;459(7244):234-238. doi:10.1038/nature08003.

47. Di D, Romanov AS, Yang L, et al. High-performance light-emitting diodes based on carbene-metal-amides. *Science (80-)*. 2017;356(6334):159-163. doi:10.1126/science.aah4345.

48. Tan Z-K. Bright light-emitting diodes based on organometal halide perovskite. *Geoing Ambient e Mineraria*. 2014;127(2):45-51. doi:10.1038/nnano.2014.149.

49. Yang X, Zhang X, Deng J, et al. Efficient green light-emitting diodes based on quasi-two-dimensional composition and phase engineered perovskite with surface passivation. *Nat Commun*. 2018;9(1):100124. doi:10.1038/s41467-018-02978-7.

50. Lin K, Xing J, Quan LN, et al. Perovskite light-emitting diodes with external quantum efficiency exceeding 20 per cent. *Nature*. 2018;562(7726):245-248. doi:10.1038/s41586-018-0575-3.

51. Era M, Hattori T, Taira T, Tsutsui T. Self-organized growth of PbI-based layered perovskite quantum well by dual-source vapor deposition.

Chem Mater. 1997;9(16):8-10. doi:10.1021/cm960434m.

52. Malinkiewicz O, Yella A, Lee YH, et al. Perovskite solar cells employing organic charge-transport layers. *Nat Photonics*. 2013;8(2):128-132. doi:10.1038/nphoton.2013.341.

53. Momblona C, Gil-Escrig L, Bandiello E, et al. Efficient vacuum deposited p-i-n and n-i-p perovskite solar cells employing doped charge transport layers. *Energy Environ Sci*. 2016;9(11):3456-3463. doi:10.1039/C6EE02100J.

54. Stranks SD, Stranks SD, Eperon GE, et al. Electron-Hole Diffusion Lengths Exceeding. *Science*. 2014;342(2013):341-344. doi:10.1126/science.1243982.

55. Bergmann VW, Weber S a. L, Javier Ramos F, et al. Real-space observation of unbalanced charge distribution inside a perovskite-sensitized solar cell. *Nat Commun*. 2014;5:5001. doi:10.1038/ncomms6001.

56. Guerrero A, Juarez-Perez EJ, Bisquert J, Mora-Sero I, Garcia-Belmonte G. Electrical field profile and doping in planar lead halide perovskite solar cells. *Appl Phys Lett*. 2014;105(13):0-5. doi:10.1063/1.4896779.

57. Chen YF, Tsai YT, Bassani DM, et al. Evidence of band bending induced by hole trapping at MAPbI3perovskite/metal interface. *J Mater Chem A*. 2016;4(44):17529-17536. doi:10.1039/c6ta08979h.

58. Dong Q, Fang Y, Shao Y, et al. Electron-hole diffusion lengths > 175 um in solution-grown CH 3 NH 3 PbI 3 single crystals. *Science (80-)*. 2015;347(6225):967-970. doi:10.1126/science.aaa5760.

59. Zhou Y, Chen J, Bakr OM, Sun HT. Metal-Doped Lead Halide Perovskites: Synthesis, Properties, and Optoelectronic Applications. *Chem Mater*. 2018;30:6589-6613. doi:10.1021/acs.chemmater.8b02989.

60. Abdelhady AL, Saidaminov MI, Murali B, et al. Heterovalent Dopant Incorporation for Bandgap and Type Engineering of Perovskite Crystals. *J Phys Chem Lett*. 2016;7(2):295-301. doi:10.1021/acs.jpclett.5b02681.

61. Wang JTW, Wang Z, Pathak S, et al. Efficient perovskite solar cells by metal ion doping. *Energy Environ Sci*. 2016;9(9):2892-2901. doi:10.1039/c6ee01969b.

62. Zhang J, Shang MH, Wang P, et al. N-Type Doping and Energy States Tuning in CH3NH3Pb1-xSb2x/3I3Perovskite Solar Cells. *ACS Energy Lett*. 2016;1(3):535-541. doi:10.1021/acsenergylett.6b00241.

63. Grancini G, Marras S, Prato M, et al. The impact of the crystallization processes on the structural and optical properties of hybrid perovskite films for photovoltaics. *J Phys Chem Lett*. 2014;5(21):3836-3842. doi:10.1021/jz501877h.

64. Grancini G, Srimath Kandada AR, Frost JM, et al. Role of microstructure in the electron–hole interaction of hybrid lead halide perovskites. *Nat Photonics*. 2015;7:695-702. doi:10.1038/nphoton.2015.151.

65. Wang Q, Shao Y, Xie H, et al. Qualifying composition dependent p and n self-doping in {CH}3NH3PbI3. *Appl Phys Lett*. 2014;105(16):163508. doi:10.1063/1.4899051.

66. Kim J, Lee SH, Lee JH, Hong KH. The role of intrinsic defects in methylammonium lead iodide perovskite. *J Phys Chem Lett*. 2014;5(8):1312-1317. doi:10.1021/jz500370k.

67. Abdelhady AL, Saidaminov MI, Murali B, et al. Heterovalent {Dopant} {Incorporation} for {Bandgap} and {Type} {Engineering} of {Perovskite} {Crystals}. *J Phys Chem Lett*. 2016;7(2):295-301. doi:10.1021/acs.jpclett.5b02681.

68. Sendner M, Nayak PK, Egger DA, et al. Optical Phonons in Methylammonium Lead Halide Perovskites and Implications for Charge Transport. 2016. doi:10.1039/C6MH00275G.

69. Glaser T, Müller C, Sendner M, et al. Infrared Spectroscopic Study of Vibrational Modes in Methylammonium Lead Halide Perovskites. *J Phys Chem Lett*. 2015;6:2913-2918. http://dx.doi.org/10.1021/acs.jpclett.5b01309. Accessed July 13, 2015.

70. Zohar A, Levine I, Gupta S, et al. What is the Mechanism of MAPbI3 p-doping by I2 ? Insights from optoelectronic properties. *ACS Energy Lett*. 2017:acsenergylett.7b00698. doi:10.1021/acsenergylett.7b00698.

71. Olthof S, Meerholz K. Substrate-dependent electronic structure and film formation of MAPbI 3 perovskites. *Sci Rep*. 2017;7(September 2016):1-10. doi:10.1038/srep40267.

72. Saive R, Scherer M, Mueller C, et al. Imaging the electric potential within organic solar cells. *Adv Funct Mater*. 2013;23(47):5854-5860.

doi:10.1002/adfm.201301315.

73. Saive R, Mueller C, Schinke J, Lovrincic R, Kowalsky W. Understanding S-shaped current-voltage characteristics of organic solar cells: Direct measurement of potential distributions by scanning Kelvin probe. *Appl Phys Lett*. 2013;103(24):2012-2015. doi:10.1063/1.4846615.

74. Zerweck U, Loppacher C, Otto T, Grafström S, Eng LM. Accuracy and resolution limits of Kelvin probe force microscopy. *Phys Rev B - Condens Matter Mater Phys*. 2005;71(12):1-9. doi:10.1103/PhysRevB.71.125424.

75. Wurfel U, Cuevas A, Wurfel P. Charge carrier separation in solar cells. *IEEE J Photovoltaics*. 2015;5(1):461-469. doi:10.1109/JPHOTOV.2014.2363550.

76. Sutherland BR, Sargent EH. Perovskite photonic sources. *Nat Photonics*. 2016;10(5):295-302. doi:10.1038/nphoton.2016.62.

77. Kim Y-H, Cho H, Lee T-W. Metal halide perovskite light emitters. *Proc Natl Acad Sci*. 2016;113(42):11694-11702. doi:10.1073/pnas.1607471113.

78. Veldhuis SA, Boix PP, Yantara N, et al. Perovskite Materials for Light-Emitting Diodes and Lasers. *Adv Mater*. 2016:6804-6834. doi:10.1002/adma.201600669.

79. Noh JH, Im SH, Heo JH, Mandal TN, Seok S Il. Chemical management for colorful, efficient, and stable inorganic-organic hybrid nanostructured solar cells. *Nano Lett*. 2013;13(4):1764-1769. doi:10.1021/nl400349b.

80. Chondroudis K, Mitzi DB. Electroluminescence from an Organic−Inorganic Perovskite Incorporating a Quaterthiophene Dye within Lead Halide Perovskite Layers. *Chem Mater*. 1999;11(11):3028-3030. doi:10.1021/cm990561t.

81. Xing G, Mathews N, Sun S, et al. Long-Range Balanced Electron- and Hole-Transport Lengths in Organic-Inorganic CH3NH3PbI3. *Science (80-)*. 2013;342(6156):344-347. doi:10.1126/science.1243167.

82. Xing G, Mathews N, Lim SS, et al. Low-temperature solution-processed wavelength-tunable perovskites for lasing. *Nat Mater*. 2014;13(5):476-480. doi:10.1038/nmat3911.

83. Savenije TJ, Ponseca CS, Kunneman L, et al. Thermally activated exciton dissociation and recombination control the carrier dynamics in organometal halide perovskite. *J Phys Chem Lett*. 2014;5(13):2189-2194. doi:10.1021/jz500858a.

84. Yang Y, Yang M, Li Z, Crisp R, Zhu K, Beard MC. Comparison of Recombination Dynamics in CH3NH3PbBr3 and CH3NH3PbI3 Perovskite Films: Influence of Exciton Binding Energy. *J Phys Chem Lett*. 2015;6(23):4688-4692. doi:10.1021/acs.jpclett.5b02290.

85. Stranks SD, Burlakov VM, Leijtens T, Ball JM, Goriely A, Snaith HJ. Recombination Kinetics in Organic-Inorganic Perovskites: Excitons, Free Charge, and Subgap States. *Phys Rev Appl*. 2014;2(3):034007. http://link.aps.org/doi/10.1103/PhysRevApplied.2.034007. Accessed September 16, 2014.

86. Yuan M, Quan LN, Comin R, et al. Perovskite energy funnels for

efficient light-emitting diodes. *Nat Nanotechnol*. 2016;11(10):872-877. doi:10.1038/nnano.2016.110.

87. Zhao P, Kim BJ, Jung HS. Passivation in perovskite solar cells: A review. *Mater Today Energy*. 2018;7(February):267-286. doi:10.1016/j.mtener.2018.01.004.

88. Supasai T, Rujisamphan N, Ullrich K, Chemseddine A, Dittrich T. Formation of a passivating CH3NH3PbI 3/PbI2 interface during moderate heating of CH 3NH3PbI3 layers. *Appl Phys Lett*. 2013;103(18):1-4. doi:10.1063/1.4826116.

89. Son DY, Lee JW, Choi YJ, et al. Self-formed grain boundary healing layer for highly efficient CH3NH3PbI3perovskite solar cells. *Nat Energy*. 2016;1(7):1-8. doi:10.1038/nenergy.2016.81.

90. Tosun BS, Hillhouse HW. Enhanced Carrier Lifetimes of Pure Iodide Hybrid Perovskite via Vapor-Equilibrated Re-Growth (VERG). *J Phys Chem Lett*. 2015;6(13):2503-2508. doi:10.1021/acs.jpclett.5b00842.

91. Zhou Z, Wang Z, Zhou Y, et al. Methylamine-Gas Induced Defect-Healing Behavior of CH3NH3PbI3 Thin Films for Perovskite Solar Cells. *Angew Chemie Int Ed*. 2015;54(33):9705–9709. doi:10.1002/anie.201504379.

92. Kong W, Rahimi-Iman A, Bi G, Dai X, Wu H. Oxygen Intercalation Induced by Photocatalysis on the Surface of Hybrid Lead Halide Perovskites. *J Phys Chem C*. 2016;120(14):7606-7611. doi:10.1021/acs.jpcc.6b00496.

93. Eperon GE, Habisreutinger SN, Leijtens T, et al. The Importance of

Moisture in Hybrid Lead Halide Perovskite Thin Film Fabrication. *ACS Nano*. 2015;9(9):9380-9393. doi:10.1021/acsnano.5b03626.

94. Dong X, Fang X, Lv M, et al. Improvement of the humidity stability of organic–inorganic perovskite solar cells using ultrathin Al_2O_3 layers prepared by atomic layer deposition. *J Mater Chem A*. 2015;3(10):5360-5367. doi:10.1039/C4TA06128D.

95. Niu G, Li W, Meng F, Wang L, Dong H, Qiu Y. Study on the stability of $CH_3NH_3PbI_3$ films and the effect of post-modification by aluminum oxide in all-solid-state hybrid solar cells. *J Mater Chem A*. 2014;2(3):705-710. doi:10.1039/C3TA13606J.

96. Bass KK, McAnally RE, Zhou S, Djurovich PI, Thompson ME, Melot BC. Influence of moisture on the preparation, crystal structure, and photophysical properties of organohalide perovskites. *Chem Commun*. 2014;50(99):15819-15822. doi:10.1039/C4CC05231E.

97. Park BW, Jain SM, Zhang X, Hagfeldt A, Boschloo G, Edvinsson T. Resonance Raman and excitation energy dependent charge transfer mechanism in halide-substituted hybrid perovskite solar cells. *ACS Nano*. 2015;9(2):2088-2101. doi:10.1021/nn507345e.

98. Mamun A Al, Ava TT, Jeong HJ, Jeong MS, Namkoong G. A deconvoluted PL approach to probe the charge carrier dynamics of the grain interior and grain boundary of a perovskite film for perovskite solar cell applications. *Phys Chem Chem Phys*. 2017;19(13):9143-9148. doi:10.1039/c7cp01140g.

99. Song Z, Watthage SC, Phillips AB, Tompkins BL, Ellingson RJ, Heben MJ.

Impact of Processing Temperature and Composition on the Formation of Methylammonium Lead Iodide Perovskites. *Chem Mater*. 2015;27(13):4612-4619. doi:10.1021/acs.chemmater.5b01017.

100. Yamada Y, Yamada T, Shimazaki A, Wakamiya A, Kanemitsu Y. Interfacial Charge-Carrier Trapping in CH3NH3PbI3 -Based Heterolayered Structures Revealed by Time-Resolved Photoluminescence Spectroscopy. *J Phys Chem Lett*. May 2016:acs.jpclett.6b00653. http://dx.doi.org/10.1021/acs.jpclett.6b00653. Accessed May 9, 2016.

101. Phuong LQ, Braly IL, Katahara JK, Hillhouse HW, Kanemitsu Y. Nonlinear photocarrier recombination dynamics in mixed-halide CH3NH3Pb(I1−xBrx)3 perovskite thin films. :1-5.

102. Handa T, Tex DM, Shimazaki A, Wakamiya A, Kanemitsu Y. Charge Injection Mechanism at Heterointerfaces in $CH_3NH_3PbI_3$ Perovskite Solar Cells Revealed by Simultaneous Time-Resolved Photoluminescence and Photocurrent Measurements. *J Phys Chem Lett*. February 2017. doi:10.1021/acs.jpclett.6b02847.

103. Saba M, Cadelano M, Marongiu D, et al. Correlated electron–hole plasma in organometal perovskites. *Nat Commun*. 2014;5(May):5049. doi:10.1038/ncomms6049.

104. Manser JS, Kamat P V. Band filling with free charge carriers in organometal halide perovskites. *Nat Photonics*. 2014;8(9):737-743. doi:10.1038/nphoton.2014.171.

105. Draguta S, Thakur S, Morozov Y V, et al. Spatially Non-uniform Trap State Densities in Solution-Processed Hybrid Perovskite Thin Films. *J Phys Chem Lett*. February 2016:715-721.

106. Pérez-del-Rey D, Boix PP, Sessolo M, Hadipour A, Bolink HJ. Interfacial Modification for High-Efficiency Vapor-Phase-Deposited Perovskite Solar Cells Based on a Metal Oxide Buffer Layer. *J Phys Chem Lett*. 2018:1041-1046. doi:10.1021/acs.jpclett.7b03361.

107. Azpiroz JM, Mosconi E, Bisquert J, De Angelis F. Defect migration in methylammonium lead iodide and its role in perovskite solar cell operation. *Energy Environ Sci*. 2015;8(7):2118-2127. doi:10.1039/c5ee01265a.

108. Abdi-Jalebi M, Andaji-Garmaroudi Z, Cacovich S, et al. Maximizing and stabilizing luminescence from halide perovskites with potassium passivation. *Nature*. 2018;555(7697):497-501. doi:10.1038/nature25989.

109. Brenes R, Guo D, Osherov A, et al. Metal Halide Perovskite Polycrystalline Films Exhibiting Properties of Single Crystals. *Joule*. 2017;1(1):155-167. doi:10.1016/j.joule.2017.08.006.

110. Yan K, Long M, Zhang T, et al. Hybrid Halide Perovskite Solar Cell Precursors: The Colloidal Chemistry and Coordination Engineering behind Device Processing for High Efficiency. *J Am Chem Soc*. March 2015. http://dx.doi.org/10.1021/jacs.5b00321. Accessed March 18, 2015.

111. Shi D, Adinolfi V, Comin R, et al. Low Trap-State Density and Long

Carrier Diffusion in Organolead Trihalide Perovskite Single Crystals. *Sci (80-)*. 2015;347(6221):519-522. doi:10.1126/science.aaa2725.

112. De Wolf S, Holovsky J, Moon SJ, et al. Organometallic halide perovskites: Sharp optical absorption edge and its relation to photovoltaic performance. *J Phys Chem Lett*. 2014;5(6):1035-1039. doi:10.1021/jz500279b.

113. Lin Q, Armin A, Nagiri RCR, Burn PL, Meredith P. Electro-optics of perovskite solar cells. *Nat Photonics*. 2015;9(2):106-112. doi:10.1038/nphoton.2014.284.

114. Ryu S, Noh JH, Jeon NJ, et al. Voltage output of efficient perovskite solar cells with high open-circuit voltage and fill factor. *Energy Environ Sci*. 2014;7(8):2614-2618. doi:10.1039/c4ee00762j.

115. Zhang J, Xu B, Johansson MB, et al. Strategy to Boost the Efficiency of Mixed-Ion Perovskite Solar Cells: Changing Geometry of the Hole Transporting Material. *ACS Nano*. 2016;10(7):6816-6825. doi:10.1021/acsnano.6b02442.

116. Calió L, Kazim S, Grätzel M, Ahmad S. Hole-Transport Materials for Perovskite Solar Cells. *Angew Chemie - Int Ed*. 2016;55(47):14522-14545. doi:10.1002/anie.201601757.

117. Yu W, Yu S, Zhang J, et al. Two-in-one additive-engineering strategy for improved air stability of planar perovskite solar cells. *Nano Energy*. 2018;45(October 2017):229-235. doi:10.1016/j.nanoen.2017.12.041.

118. Belisle RA, Jain P, Prasanna R, Leijtens T, McGehee MD. Minimal Effect of the Hole-Transport Material Ionization Potential on the Open-

Circuit Voltage of Perovskite Solar Cells. *ACS Energy Lett*. 2016;1(3):556-560. doi:10.1021/acsenergylett.6b00270.

119. Tress W, Yavari M, Domanski K, et al. Interpretation and Evolution of Open-Circuit Voltage, Recombination, Ideality Factor and Subgap Defect States during Reversible Light-Soaking and Irreversible Degradation of Perovskite Solar Cells. *Energy Environ Sci*. 2017;11:151-165. doi:10.1039/C7EE02415K.

120. Tress W. Maximum Efficiency and Open-Circuit Voltage of Perovskite Solar Cells. In: *Organic-Inorganic Halide Perovskite Photovoltaics*. Cham: Springer International Publishing; 2016:53-77. doi:10.1007/978-3-319-35114-8_3.

121. Tress W. *Organic Solar Cells*. Vol 208. Cham: Springer International Publishing; 2014. doi:10.1007/978-3-319-10097-5.

122. Tress W. Perovskite Solar Cells on the Way to Their Radiative Efficiency Limit - Insights Into a Success Story of High Open-Circuit Voltage and Low Recombination. *Adv Energy Mater*. 2017. doi:10.1002/aenm.201602358.

123. Miyano K, Yanagida M, Tripathi N, Shirai Y. Simple characterization of electronic processes in perovskite photovoltaic cells. *Appl Phys Lett*. 2015;106(9):093903. http://scitation.aip.org/content/aip/journal/apl/106/9/10.1063/1.4914086. Accessed March 5, 2015.

124. Miyano K, Tripathi N, Yanagida M, Shirai Y. Lead Halide Perovskite Photovoltaic as a Model p-i-n Diode. *Acc Chem Res*. 2016;49(2):303-

310. http://dx.doi.org/10.1021/acs.accounts.5b00436. Accessed March 10, 2016.

125. Chen Y, Yi HT, Wu X, et al. Extended carrier lifetimes and diffusion in hybrid perovskites revealed by Hall effect and photoconductivity measurements. *Nat Commun*. 2016;7:12253. doi:10.1038/ncomms12253.

126. Ravishankar S, Gharibzadeh S, Roldán-Carmona C, et al. Influence of Charge Transport Layers on Open-Circuit Voltage and Hysteresis in Perovskite Solar Cells. *Joule*. 2018;2(4):788-798. doi:10.1016/j.joule.2018.02.013.

10 List of abbreviations

AFM	Atomic force microscopy
APS	Air Photoemission measurement system
DSSC	Dye sensitized solar cell
E_g	Band gap energy
EQE	External quantum efficiency
ETM	Electron transport material
$FAPbI_3$	Formamidinium lead triiodide
FF	Fill factor
FIB	Focused Ion Beam
GB	Grain boundary
GIXRD	Grazing incidence x-Ray diffraction
HOMO	Highest occupied molecular orbital
HTM	Hole transport material
I	Current
IP	Ionization potential
IR	Infrared
ITO	Indium tin oxide

J	Current density
J_{SC}	Short circuit current density
LED	Light emitting diode
LUMO	Lowest unoccupied molecular orbital
MA	Methylammonium
MAI	Methylammonium iodide
$MAPbBr_3$	Methylammonium lead tribromide
$MAPbCl_3$	Methylammonium lead cloride
$MAPbI_3$	Methylammonium lead triiodide
OLED	Organic light emitting diode
PCE	Power conversion efficiency
PESA	Photo-electron spectroscopy
PL	Photoluminescence
PLQY	Photoluminescence quantum yield
PSC	Perovskite solar cell
SEM	Scanning electron microscopy
V	Voltage
V_{OC}	Open circuit voltage
XRD	X-Ray diffraction